Aerodynamic Shape Optimization of Natural Laminar Flow Airfoils via Discrete Adjoint Approach

Peyman Khayatzadeh

Doctor of Philosophy

Department of Mechanical Engineering

McGill University

Montreal,Quebec

2012-12-12

A dissertation submitted to McGill University in partial fulfilment of the requirements for the degree of doctor of philosophy

ACKNOWLEDGEMENTS

I would like to express my sincere thanks to my supervisor, Professor Siva Nadarajah, for sharing his knowledge and professional experience with me during my studies. It has been a great honor to work under his supervision. I am grateful to the past and present members of McGill computational fluid dynamics laboratory (CFDLab) for their support and friendship. I would like to extremely thank my parents who sacrifice so much for me to have a better education. Above all, my eternal gratitude goes to my wife for all her love, patience, and encouragement. I would like to dedicate this dissertation to her.

ABSTRACT

In this research the $\gamma - \tilde{Re_{\theta t}}$ transition model is combined with the $k - \omega$ SST turbulence model to predict the transition region for a laminar-turbulent boundary layer and redesign the geometry to achieve lower skin friction drag coefficients. The present work addresses several modifications necessary for a robust transition model and investigates the accuracy of the model for a wide range of angles of attack and Reynolds numbers. The transition model is employed to predict the transition locations and an assessment of the various transition mechanisms, Reynolds number effects, sectional characteristics, and aerodynamic performance for two subsonic airfoils are presented with comparisons to experimental data and numerical solutions. Discrete adjoint equations for the transition and turbulence models are derived and implemented into the design framework. The adjoint-based optimization procedure is employed to optimize the S809 wind turbine profile and NLF(1)-0416 airfoil to postpone the onset of transition and extend the natural laminar region of the transitional flow for minimizing the total drag, while maintaining the lift, or maximizing the lift-to-drag ratio. The obtained results demonstrate the ability of the developed optimization framework to design new natural laminar flow airfoils.

ABRÉGÉ

Dans cette recherche, le modèle de transition $\gamma - \tilde{Re_{\theta t}}$ est combiné avec le modèle de turbulence $k-\omega$ SST afin de prédire la transition vers le régime turbulent et d'obtenir des formes aérodynamiques au frottement visqueux minimal. Nous présentons les modifications nécessaires à l'amélioration de la robustesse du modèle de transition et étudions la précision du modèle pour une large gamme d'angles d'attaque et de nombres de Reynolds. Le modèle de transition est utilisé pour prédire le point de transition, pour évaluer les mécanismes de transition ainsi que les différents effets reliés au nombre de Reynolds, et pour étudier les caractéristiques et les performances aérodynamique de deux profils aérodynamiques. Des comparaisons avec des données expérimentales et des solutions numériques sont présentées. Les équations adjointes discrètes des modèles de transition et de turbulence sont dérivées et employées dans un processus d'optimization. Cette procédure d'optimisation est utilisée pour modifier le profil d'éolienne S809 et le profil NLF(1)-0416 afin de retarder la transition et d'étendre la zone laminaire de l'écoulement, de minimiser le coefficient de traînée totale tout en maintenant la portance, ou de maximiser la finesse aerodynamique. Les résultats obtenus démontrent la capacité du procéssus d'optimisation développé à concevoir de nouveaux profils écoulement laminaire naturel.

TABLE OF CONTENTS

LIST OF TABLES

LIST OF FIGURES

CHAPTER 1
Introduction

1.1 Introduction

The rise in fuel prices together with the impending threat of an increase in greenhouse gases due to the projected increases in global air travel has renewed a call for the development of the next generation commercial air transport. The European Union's Clean Sky initiative [20] and NASA's Environmentally Responsible Aviation (ERA) Project [19] have placed benchmarks on the type of performance improvements that are expected on future aircraft designs. The goal is to develop the enabling technologies to design environmentally responsible aircraft. The NASA N+3 program, which stands for three generations after the current commercial transport aircraft, helps to develop technological bases for advanced airframes and propulsion systems for aircraft scheduled to enter service in 2030. The following are brief summaries of the various conceptual designs proposed by leading airframe manufactures and institutions.

- Aircraft and Technology Concepts for an N+3 Subsonic Transport.

  Here the design and manufacture of a subsonic fixed wing transport airplane for 2030's as well as more environmentally and economically friendly technologies are studied. This aircraft is anticipated to reduce the noise up to 71 db, the NOx emission up to 80%, and the fuel consumption up to 60% in comparison with current fixed wing transport aircraft [13]. Three innovative concepts: liquid natural gas as fuel, multiple-engine propulsion, and lower cruise speed, are considered as the main design aspects of the airplane (figure 1–1). The reduced Mach number combined with nearly-unswept wing reduces the wing weight and induced drag, eliminates the leading edge slats, and maintains natural laminar flow on the wing bottom. The double-bubble composite fuselage with lifting nose increases the optimum carryover lift and effective span and reduces floor-beam weight. A roomier passenger cabin with fewer windows decreases the airplane weight as well. The benefit of the lifting nose is to have built-in nose-up trimming moment [13]. Three geared turbofans with a high bypass ratio of 20 and high efficiency small cores increase the engine performance and reduce the emissions. Having advanced combustors, materials, and a cooling system in addition to having variable area nozzles further increases the efficiency of this engine. The engine/pi-tail integration improves the propulsive efficiency via fuselage boundary layer ingestion and shield the fan noise. The other benefits are immunity from bird strike, small vertical tails due to small engine-out yaw, and lightweight horizontal tail [13]. A 10% lower cruise speed helps the designers to use technologies that are not applicable to current transonic commercial airplanes. Participants in this study include Aurora Flight Sciences, Aerodyne Research Inc., Pratt & Whitney, and Boeing Phantom Works led by Massachusetts Institute of Technology [19].

- Small Commercial Efficient and Quiet Air Transportation for 2030-2035.

Figure 1–1: N+3 Subsonic Fixed Wing Transport Airplane [19]

The main goal is to develop the technology road-maps for a suburban airplane with minimum impact on the environment. A hybrid technique that combines a natural laminar flow (NLF) wing with active laminar flow to further extend the transition point assist in reducing the total drag and fuel burn. Advances in material and manufacturing processes will allow for more complex NLF wing shapes, guaranteeing higher aerodynamic performance [7]. Advanced low NOx combustors combined with low noise and high performance propellers reduce the engine emission and noise. Using advanced propulsion materials reduces the need for cooling, lowers the engine weight, and increases the performance and durability of the engine. To reduce the airframe weight, low weight composite structures are employed [7]. This 10- to 30-passenger aircraft (figure 1–2)

Figure 1–2: Small Commercial Efficient and Quiet Airplane [19]

will reduce air traffic congestion and help better utilization of the current community airport infrastructures. GE Aviation along with GE Global Research, the Cessna Aircraft Company, and the Georgia Institute of Technology are participating in this program [19].

- Subsonic Ultra Green Aircraft Research (SUGAR).

  This project, as part of NASA's subsonic fixed wing technical plan, will investigate advanced concepts and technologies for future subsonic fixed wing aircraft (figure 1–3). Currently laminar flow technologies are not mentioned in the released publications; however due to the aircraft low Mach number and low swept wing, laminar flow control techniques will mostly likely be employed. The aircraft performance will be evaluated in regards to the noise, emission,

Figure 1–3: Subsonic Ultra Green Aircraft Research [19]

take-off and landing length, and fuel consumption indicators. Technologies and aircraft configuration risk will be identified along with the development of technical road-maps for future aircraft programs [19]. The aircraft is based on the Boeing 737-800 and is designed to lift 150 passengers with a higher aspect ratio strut braced wing [2]. An advanced turbofan engine (gFan+) with a high bypass ratio in addition to advanced combustor, compressor, and turbine is developed to reduce noise and emission, and in the process decrease the fuel consumption. Another version of SUGAR employs an electric-gas turbine engine (hFan) which uses batteries to assist the aircraft during take-off and cruise [2]. Boeing Phantom Works along with Boeing Commercial Airplanes, General Electric, and the Georgia Institute of Technology are the research team members [19].

- Advanced Concepts for Subsonic Commercial Transport Aircraft.

  This project focuses on the development of advanced configurations and new systems designed with a special interest on environmental issues such as noise footprint, runway requirements, and traffic mix projections for in flight and

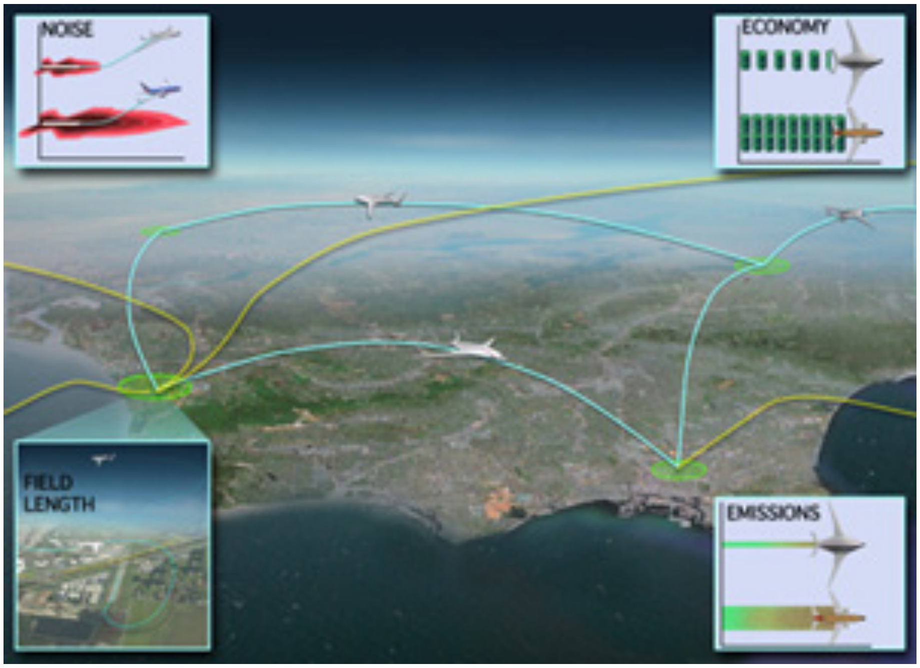

Figure 1–4: Subsonic Commercial Transport Aircraft [19]

near airports (figure 1–4). In this project advanced propulsion concepts, multi-mode propulsion, short take-off and landing, variable geometry, and flow control are studied and the application of advanced material and manufacturing technologies are evaluated. These advanced processes reduce the airplane weight and increase the performance and durability. The project has been awarded to a team that includes Tufts University, Sensis Corp., Spirit Aerosystems Corp. and Rolls-Royce North America Technologies Inc. (LibertyWorks) led by Northrop Grumman Systems Corporation [19].

Across the Atlantic, the EU initiative is currently supporting six Clean Sky platforms, where the Green Regional Aircraft (GRA) program that combines the expertise of 32 European companies, is one of the most ambitious platforms [20]. To reduce pollutant emissions and noise generation, the GRA is designed with a light weight structure, with advances in both aerodynamic and engine efficiencies, and a complete life-cycle and environmental impact analysis including sustainable manufacturing to ensure that the aircraft satisfies future standards and regulations. The following themes form the major concentration of innovation required to establish a realizable aircraft: Low Weight Configuration (LWC), Low Noise Configuration (LNC), All Electric Aircraft (AEA), Mission and Trajectory Management (MTM), and New Configuration (NC). In the low noise configuration (LNC) phase, methods for reducing the airplane drag and fuel consumption will be evaluated with a view on decreasing external noise. NLF technology is employed to reduce the skin friction drag. The NLF technology has some disadvantages that will be explained in section 1.2 and will be improved by using innovative high lift and anti-icing devices. The gears will be aerodynamically optimized to reduce the generated turbulence and consequently the airplane drag and noise. In addition, improvements of the high lift systems will further reduce the airframe noise [20]. In the final phase of the project, a new configuration of an advanced regional aircraft will be defined. This new aircraft will employ state-of-the-art avionics, innovative engines such as open rotors, and optimized aerodynamics and structure within a multidisciplinary design environment. Low noise and emission to reduce the environmental impact on near airport communities will be incorporated [20].

A second Clean Sky platform, the Smart Fixed Wing Aircraft (SFWA) project, led by Airbus and Saab AB are illustrated in figure 1–5. The goals of this project are [20]:

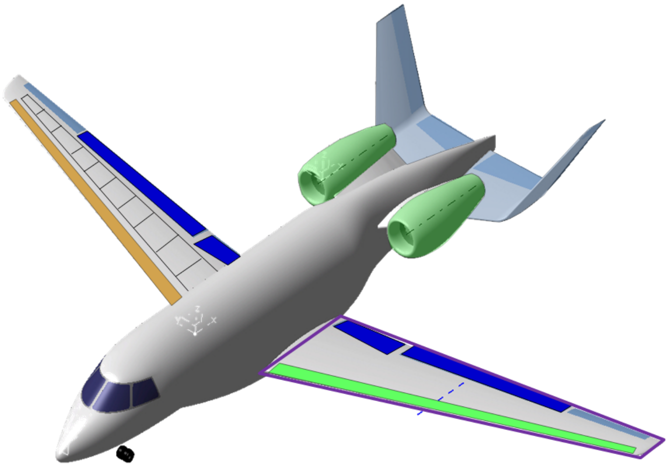

Figure 1–5: Smart Fixed Wing Aircraft [20]

1. To reduce 25% of the wing drag by using active and passive natural laminar flow technologies. Since the total wing drag produces 40% of the aircraft drag, this reduction translates to 10% of the aircraft total drag reduction.
2. To reduce 20% of the fuel consumption by employing a counter rotating open rotor engine. For this purpose a new rotor blade and pylon will be designed to decrease the noise and vibration levels.

In the majority of new advanced subsonic aircraft proposed either through EU's Clean Sky [20] or NASA's ERA program [19], laminar flow control techniques, either passive or active, play a prominent role in the anticipated reduction in total drag. Drag reduction is a significant issue in aircraft design, where one drag count reduction in the design of a subsonic transport airplane corresponds to approximately 200lb increase of its payload [3]. The efficiency of the aircraft increases by reducing the drag and consequently a reduction in fuel burn is accompanied if the aircraft range is kept constant. The lower fuel burn translates into lower emissions and thus the technology contributes towards the total expected greenhouse gas reduction that is expected for the next generation of commercial aircraft.

For an aircraft, the total drag is broken down into four components based on their origins [33] as follows:

- Skin-friction Drag

  A boundary layer develops over the airplane wing and the produced shear stress forms the skin friction component of the drag. The skin friction drag is the largest component and contributes approximately half of the total drag at a cruise condition.

- Pressure Drag

  The developed viscous shear layer produces dissimilar pressure distributions over the forward and rear portions of the wing. This pressure imbalance due to the viscous effects, creates the pressure component of the total drag.

- Wave Drag

  At transonic flights, the presence of shock waves produces the wave drag component. The entropy generation across the shock wave reduces the stagnation pressure and increases local static pressure in order to recover the freestream pressure at the trailing edge; this pressure increase across the shock wave forms the wave drag. In addition the interaction of the shock wave and the boundary layer over the wing leads to boundary layer separation, further increasing the drag.

- Vortex Drag

> The tip vorticies generated over the lifting surfaces of the airplane develop the vortex component of the drag. The vortex drag is also known as the lift-induced drag since its magnitude is proportional to the square of the airplane lift. This component produces the second largest portion of the total drag.

A total drag breakdown of a medium size transport in cruise, demonstrates that the skin friction drag is the dominant component with approximately 45% of the total drag, while the lift-induced and pressure drag components are 40% and 15% respectively [15, 48]. The aircraft wing produces approximately 35% of the skin friction drag which is the second largest contribution after the fuselage with 40% [15]. Hence, designing an aircraft that maintains laminar flow over the wing helps to reduce the skin friction and total drag significantly. This drag reduction decreases the required engine thrust and fuel consumption consequently.

In the 1930's it was discovered that increasing the favourable pressure gradient over the wing can postpone the onset of transition and reduce the skin friction component of the total drag by extending the laminar boundary layer around the wing. Generally, three different laminar flow control methods, passive, active, and hybrid, are available to extend the laminar flow [4]. In the passive method, the aerodynamic shape is designed to maintain a favourable pressure gradient over a large area of the wing to postpone the transition and increase the extension of the laminar boundary layer. This method is known as natural laminar flow (NLF) since it maintains the laminar flow as much as possible over the wing. The NLF method has two advantages; first, the wing shape is optimized to ensure a large laminar region and hence additional weight contributing equipment is not required; second, the NLF method is a passive technology and therefore it does not increase the fuel consumption of the airplane [4]. However, the NLF passive approach is not applicable at high Reynolds numbers where the growth of streamwise instability waves is fast, and at high sweep angles where the crossflow instabilities are the dominant transition mechanism [15].

In contrast to the NLF approach, there are various active flow control methods such as laminar flow control (LFC), hybrid laminar flow control (HLFC), and plasma actuators. These methods extend the laminar flow in the presence of an adverse pressure gradient by maintaining convex and stable velocity profiles along the boundary layer while the NLF approach extends the favourable pressure gradient region to postpone the transition point [12]. The active flow control methods increase the operational weight and fuel consumption of the aircraft due to an additional suction unit for the wing surface. Ice and insects can fill out the suction holes and reduce the efficiency of the active flow control techniques in addition to contaminate the laminar boundary layer and trip the boundary layer to fully turbulent. In the case of an asymmetric failure of the active flow control system, dissimilarity in the drag and lift on the aircraft wings can lead to unsymmetrical rolling and yawing moments which alter the aircraft balance and stability [4].

The laminar flow control (LFC) technique thins the boundary layer thickness and alters the boundary layer profile by the employment of suction. In addition, the LFC method reduces the effect of crossflow instabilities over the swept wings. These effects stabilize the laminar boundary layer, postpone the transition point, and increase the extension of laminar flow over the wing [4].

The hybrid laminar flow control (HLFC) technique combines the benefits of the passive and active approaches [4]. It employs the natural laminar flow aerodynamic shapes to increase the favourable pressure gradient and incorporates LFC techniques to control the laminar flow in adverse pressure gradient regions and crossflow instabilities [4].

The plasma actuator which is the third active flow control method, modifies the velocity profile by introducing additional momentum into the unenergized regions of the boundary layer. The higher momentum velocity profile is more resistant to the disturbances and damps out Tollmien-Schlichting (T-S) waves; therefore the stability characteristics of the modified boundary layer is augmented [14, 21]. In addition, the pulsed plasma actuators have been successfully applied in active wave cancellation. The actuator working in a closed loop mode produces waves along the boundary layer. These waves have the same amplitude as the T-S disturbances but with inverted phase (antiphase) in order to cancel the T-S waves and postpone the onset of transition. These three different active flow control approaches extend the laminar flow over the aircraft wing and reduce the airplane total drag [14, 21].

1.2 Natural Laminar Flow (NLF) Airfoils

In the 1930's an inverse design method was applied to design new airfoils by considering a pressure distribution and finding its corresponding airfoil shape [53]. During the 1940's and 1950's, NASA designed the 2-7 series airfoils systematically by employing the inverse method and tested them in the Langley Low-Turbulence Pressure Tunnel (LTPT) [53]. The favourable pressure gradient over the forward portion of the airfoil accelerates the flow and reduces the local pressure in order to stabilize and maintain the laminar boundary layer. Since the transition points are located near the minimum pressure points, designers modified pressure distributions by postponing the minimum pressure points as much as possible to increase the extension of laminar boundary layers. Airfoils which were able to maintain laminar flow over more than 30% of the chord length on both upper and lower surfaces, were named NLF airfoils [53].

By increasing the laminar flow region, the tangential force over the airfoil decreases and NLF airfoils can have significantly lower drag coefficients over a small range of Reynolds numbers. However, this very important benefit comes with several disadvantageous. First, the lower momentum in the laminar boundary layer results in bursting of the laminar separation bubble which is a transition mechanism at low and moderate angles of attack and will be explained further in section 1.3; hence NLF airfoils have poorer stall characteristics, and thus are not suitable at landing and takeoff conditions. However, changes to the geometric twist angle can alter the pressure distribution over the aircraft wing and improve the early laminar separation of NLF wings. Second, NLF airfoils are very sensitive to roughness since roughness may trip the laminar to a turbulent boundary layer. Apart from specific airfoil characteristics, there are geometric wing planform parameters that could promote laminar flow. Forward swept wings and larger taper ratios can reduce crossflow and attachment line instabilities to achieve significant regions of laminar flow over the wing. In addition, the use of composite materials has introduced an unintended potential benefit for future aircraft wings. Absence of rivets on composite wings, will allow aircraft manufactures to capitalize on the smooth surfaces and employ NLF profiles.

There are three classical approaches to design NLF wing sections. The first method known as the direct approach, modifies an airfoil's geometrical parameters such as leading edge radius, thickness distribution, and camber to achieve a desired set of airfoil characteristics. This traditional approach is only possible at the hands of a skillful aerodynamicist [53]. The second approach employs an inverse design method, where an airfoil shape is recovered to produce a target pressure or velocity distribution [53]. The last approach is to apply a gradient-based optimization technique. In this method a proper objective function is defined to postpone the transition point and to extend the laminar flow over the entire airfoil with respect to the geometrical and aerodynamic constraints. The airfoil shape is iteratively modified until the cost function is satisfied. This approach is general and applicable to a wide range of flows but requires a large number of flow evaluations to calculate the sensitivity of the cost function associated with the airfoil shape parameters.

1.3 Transition Models

The numerical simulation of flow without considering the transition process may result in the overprediction of total drag leading to an incorrect estimation of aerodynamic load and performance. Modelling of transition from laminar to fully turbulent boundary layer increases the accuracy and capability of computational fluid dynamics (CFD) analyses to simulate the flow field more realistically, with better agreement with experimental data. When the experimental data about the location of the transition points are available, then the transition point can be set manually and laminar-turbulent RANS solvers can be used to simulate the transition process. In cases where the experimental data about the transition point is unavailable, then there are two possible options: first, an educated guess of the transition point based on interpolation among available data; second, a fully turbulent solution. Neither method is applicable to CFD-based aerodynamic shape optimization and design frameworks where in every design cycle a new geometry is generated and there is no experimental transition point available for these new cases. In addition, development of a design (optimization) framework to potentially reduce the viscous drag is dependent on the reliable prediction of transition points.

Using the transition prediction models incorporated within a laminar-turbulent RANS solver can increase the accuracy and capability of the flow solver by predicting the transition point and solving the laminar-turbulent flow instead of only the fully turbulent flow. These models extend from simple empirical relationships via linear stability equations (LSE) to parabolic stability equations (PSE) [57]. Empirical correlations for predicting the onset of transition are limited to two-dimensional incompressible flows such as Michel's method [6], Granville's method [6], and the $H - R_x$ method [6]. The LSE and PSE methods using the e^n criterion are computationally costly in comparison with the empirical correlations and are practically impossible for complex geometries since they require a separate boundary layer solver to compute integrated and non-local boundary layer parameters such as the displacement and momentum thicknesses. There are several methods to model three-dimensional transitional flows. A computationally efficient approach, employs several two-dimensional solutions to generate the three-dimensional transition line. The two-dimensional transition points could be obtained from the popular XFOIL and MSES codes [30] that employ a simple viscous/inviscid coupling; however, the technique does not consider the effect of crossflow instabilities. An alternate approach is to solve the quasi-3D boundary layer by using sweep/taper boundary layer analysis based on the conical flow assumption [58] or by using a database method [45] to provide the integral parameters of the boundary layer to simulate the growth of the streamwise Tollmien-Schlichting (T-S) waves and crossflow (CF) instabilities. The e^n method is applied in both the streamwise and crossflow directions with typical n-factors of 9 and 5 respectively to predict the onset of transition. To consider the interference between the T-S and crossflow instabilities a composite amplification ratio [58] can be defined based on the streamwise and crossflow n-factors.

Apart from e^n-based approaches, correlation-based methods employ experimental data together with transport equations to limit the production of the turbulent kinetic energy present in most turbulence models. These models such as the $\gamma - \tilde{Re}_{\theta t}$ transition model are designed to predict various transition processes within modern CFD codes and are able to address practical engineering problems. To employ a transition model which is fully compatible with turbulent RANS solvers and that it can be integrated into a design framework, the transition model should possess the following properties [30, 32]: allow the calibrated prediction of the onset and the length of all transition mechanisms, require only local parameters, does not affect the fully turbulent region, is not dependent on the coordinate system, and is extendable to three dimensions. In comparison with other transition models such as the e^n method, the $\gamma - \tilde{Re}_{\theta t}$ transition model encompasses these properties. Moreover it has the ability of using local parameters provided by a RANS solver instead of using an additional boundary layer solver coupled with a RANS solver. This transition model provides a unique solution based on the prescribed conditions, is able to be coupled with the $k-\omega$ SST turbulence model and does not affect the solution of the fully turbulent region.

Unlike the e^n method which predicts only the onset of transition by using different n factors based on the ambient turbulence intensity and the roughness of the surface, the $\gamma - \tilde{Re}_{\theta t}$ transition model predicts the onset and length of the transition process and even the reattachment point in case of a laminar separation bubble. In comparison with the linear stability theory such as the e^n method which predicts the linear growth of instability waves, the $\gamma - \tilde{Re}_{\theta t}$ transition model simulates all four transition mechanisms and even analyzes the bypass transition caused by the non-linear growth of the instabilities. The $\gamma - \tilde{Re}_{\theta t}$ transition model is able to simulate the laminar-turbulent flow over complex geometries [30] while the e^n method has some limitations such as the need for an accurate separate boundary layer solver. As the transported variables are evaluated based on the local freestream velocity, the $\gamma - \tilde{Re}_{\theta t}$ transition model is dependent on the coordinate system and this is the only deficiency in the model [32]. The $\gamma - \tilde{Re}_{\theta t}$ transition model coupled with a three-dimensional turbulent RANS solver without employing an additional boundary layer solver, has shown the ability to model transition from laminar to fully turbulent three-dimensional flows and the results have been validated by available experimental data [30]. In three dimensions, the $\gamma - \tilde{Re}_{\theta t}$ transition model with the current correlations is able to simulate the transition process through the attachment line contamination. This model has the potential capability of simulating the crossflow instabilities and their effects can be included in the correlations. Up to date, no practical correlation that includes the crossflow contributions has been proposed and the present work can be a basis to develop a three-dimensional laminar-turbulent RANS solver based on the $\gamma - \tilde{Re}_{\theta t}$ transition model that simulates all different types of transition mechanisms such as crossflow instabilities for three-dimensional applications and ultimately employ the new framework to design and optimize the next generation predominantly laminar flow aircraft wings. .

1.4 Transitional and Turbulent Airfoil Optimization

Upon the introduction of the finite-difference method to compute the sensitivity derivatives for the purpose of shape optimization by Hicks and Henne [16], gradient-based methods have been used widely in aerodynamic optimization and design problems [43]. The use of finite-difference to compute sensitivity derivatives is both computationally costly and subject to subtractive cancellation errors which prevented the approach from providing sensitivity derivatives that were accurate for viscous flows. Through the work of Lions et al. [35] on the establishment of optimal control of systems governed by partial differential equations, Pironneau [46] introduced the control theory approach for elliptic design problems by computing the gradient in a less costly approach than the finite-difference technique. In this approach the gradient of the cost function is obtained by solving the adjoint equations independent of the number of the design variables. Jameson et al. [23, 25, 26] applied this theory initially to potential flow and subsequently for the Euler and Navier-Stokes (N-S) equations (hyperbolic PDEs) and successfully demonstrated automatic aerodynamic shape optimization of complete aircraft configurations in transonic flow. There are two approaches, the continuous and discrete, in deriving the adjoint equations. In the continuous approach, the adjoint equations and their boundary conditions are derived by perturbing the cost function and flow field equations with respect to flow variables through the use of Lagrange multipliers [43]. The equations are then discretized and solved numerically. In the alternate approach, the discrete adjoint equations are derived by applying control theory directly to the discretized flow field equations. The primary difference between the two approaches is the accuracy of the resulting gradients of the objective function with respect to any geometrical parameter or flow property. The solution of the discrete adjoint equations, provides the exact discrete gradient that is independent of the grid size, while the continuous approach provides an inexact gradient of the computed objective function. As the grid size increases, the discretized continuous gradient approaches the true discrete gradient. The reader is encouraged to refer to Nadarajah et al. [43, 44] for a complete comparison between the continuous and discrete adjoint equations for inviscid and viscous flows. In this preliminary work, the Baldwin-Lomax turbulence model was employed and the eddy viscosity was assumed to be constant during the linearization of both the continuous governing equations and its discrete counterpart.

In Le Moigne et al.'s work [42], the linearization of the Baldwin-Lomax model was included in their derivation of the discrete adjoint equations. The eddy viscosity, μ_t, in the Baldwin-Lomax turbulence model was defined based on local flow variables and the straight differentiation of the eddy viscosity was used for linearization. The obtained gradient was compared against the finite difference method and its ability in the drag minimization of the ONERA M6 wing was shown by employing a sequential quadratic programming (SQP) optimization algorithm. Zymaris et al. [60] developed a continuous adjoint approach for the incompressible flow solver and the SA turbulence model to investigate the sensitivities and gradient accuracy. The eddy viscosity is not considered constant and the corresponding continuous adjoint equations and boundary conditions for the SA turbulence model are derived. In internal flow problems, where the total pressure loss is heavily dependent on the turbulence model, they showed that the gradient is more accurate than the gradient obtained without considering an extra adjoint equation for the SA turbulence model. Kim et al. [28] developed a discrete adjoint approach and a direct differential method in order to study the sensitivity of RANS equations using three different two-equation turbulence models (Menter's $k-\omega$ SST , Wilcox's $k-\omega$ and standard $k-\epsilon$ models). They showed that when the two-equation turbulence models are applied the assumption of constant eddy viscosity in adjoint methods does not provide accurate sensitivity derivatives in turbulent flows involving strong shocks. The two additional adjoint variables related to the discrete adjoint equations of the turbulence models improves the accuracy of the gradient and increases the ability of the adjoint approach to obtain better results.

After reviewing several fully turbulent optimization and design frameworks, the developed laminar-turbulent flow solvers and their corresponding design and optimization approaches are briefly explained. Lee et al. [33] developed a design and optimization framework for NLF airfoils and wings by using a continuous adjoint approach and an automatic transition prediction module. This module predicts the location of transition points in each design cycle. The Baldwin-Lomax turbulence model is used for calculating the eddy viscosity in each cell. Here transition points are not considered as design parameters and computed automatically in each design cycle; therefore the adjoint equations for the transition prediction method are not derived and employed in the optimization process. Amoignon et al. [1] developed a transitional flow solver, where an Euler solver provides pressure distributions for a separate boundary layer solver in order to compute the integral parameters for solving the parabolized stability equations (PSE). The adjoint equations for the combined flow solver are derived and employed in a gradient-based optimization procedure. The cost function is the minimization of the energy of the disturbances combined with the minimization of the wave drag in order to design NLF airfoils. The RAE2822 airfoil is optimized in order to delay the transition point and remove the shock wave. By reducing the total amplification of the disturbances, the transition point is delayed and the skin friction drag component is reduced. In addition, the pressure drag decreases by removing the shock wave; therefore the total drag is minimized while the lift and pitching moment are maintained. Driver et al. [10] incorporated the MSES code [9] to their two-dimensional Newton-Krylov flow solver employing the SA turbulence model [56]. The MSES code couples the Euler equation together with a boundary layer solver and uses the e^n criterion to predict the onset of transition points over the airfoil surface. The developed laminar-turbulent flow solver has been employed in an aerodynamic shape optimization framework where adjoint-based gradients are employed to compute the contribution from the RANS equations together with finite-difference based gradients of the MSES code and demonstrated the ability of the optimizer to move the locations of the transition points in order to maximize the lift, performance, and endurance factor of the airfoils [10].

1.5 Objectives

In this dissertation an improved $\gamma - \tilde{R}e_{\theta t}$ transition model is introduced and validated for the simulation of transitional flows around NLF airfoils. The discrete adjoint equations for the $\gamma - \tilde{R}e_{\theta t}$ transition and $k - \omega$ SST turbulence models are derived in order to develop an adjoint-based design and optimization of NLF airfoils. Finally new algorithms for the design of high lift-to-drag ratio NLF airfoils are demonstrated by introducing novel objective functions such as the production of turbulent kinetic energy.

1.6 Author's Contributions

In the present work, the $k - \omega$ SST turbulence and $\gamma - \tilde{R}e_{\theta t}$ transition models are implemented into the employed Reynolds-averaged Navier-Stokes (RANS) solver. The $k - \omega$ SST turbulence model is modified to be used in the developed transitional flow solver. Modifications to the $\gamma - \tilde{R}e_{\theta t}$ transition model are proposed to increase the robustness and provide accurate solutions to a wider range of angles of attack and Reynolds numbers. The discrete adjoint equations for the $k - \omega$ SST turbulence and $\gamma - \tilde{R}e_{\theta t}$ transition models are derived and added to the discrete adjoint equations of the RANS solver. The developed flow solver has been tested for various airfoils and its accuracy and robustness have been validated. Furthermore, the developed transitional discrete adjoint solver has been successfully employed to design and optimize NLF airfoils.

1.7 Thesis Outline

In chapter 2, the turbulent RANS solver, $\gamma - \tilde{Re}_{\theta t}$ transition model, and their numerical implementation are described. The necessary modifications to the $k - \omega$ SST turbulence model to allow it to be coupled with the $\gamma - \tilde{Re}_{\theta t}$ transition model are thoroughly discussed. Finally, the proposed changes to the $\gamma - \tilde{Re}_{\theta t}$ transition model to increase its robustness and accuracy at various Reynolds numbers and angles of attack are described.

In chapter 3, the gradient based optimization methods are explained. The unconstrained optimization approaches such as steepest descent and smoothed steepest descent methods are described and compared. The constrained optimization procedure and the first-order optimality conditions are then presented. Finally, the various approaches for choosing the design variables are discussed.

In chapter 4, the discrete adjoint theory is explained. The discrete adjoint equations for the $\gamma - \tilde{Re}_{\theta t}$ transition and $k - \omega$ SST turbulence models are derived as well as their boundary condition source terms. The various cost functions employed in the present work and their implementation are explained. Finally the gradient of the cost function and the mesh perturbation method used in this research are discussed.

Chapter 5 presents the validation of the results obtained by the developed flow solver. The residual convergences of the laminar-turbulent flow solver, the $\gamma - \tilde{Re}_{\theta t}$ transition model, and the $k - \omega$ SST turbulence model are studied. A thorough grid study for the streamwise and normal directions are provided. The accuracy of the laminar-turbulent flow solver are demonstrated for two different cases: the S809 wind turbine blade, and the NLF(1)-0416 airfoil, and the results are validated by comparing against available experimental data. The distributions of the pressure coefficients and the skin friction coefficients are shown as well. Then the location of the transition points at various angles of attack and the drag polar at different Reynolds numbers are sketched against the experiments. Finally, the change of the size of the laminar separation bubble at various angles of attack and Reynolds numbers are qualitatively compared with the experimental reports.

In chapter 6, taking advantage of having an accurate laminar-turbulent flow solver, the aerodynamic shape optimization framework is used to design new NLF airfoils for minimizing the drag and maintaining or maximizing the lift. The NLF(1)-0416 airfoil is optimized with and without using the transitional and turbulent adjoint variables to show the influence of solving the adjoint equations for the transition and turbulence models. The observed difference between the results illustrates that having these adjoint variables increases the accuracy of the obtained gradient and improves the design process of the NLF airfoils. Furthermore, introducing the production of turbulent kinetic energy to the cost function increases the effectiveness of the transitional and turbulent adjoint variables and improves the optimization of NLF airfoils. The airfoil shape is modified to maintain a favourable pressure gradient and postpone the onset of transition over the upper and lower surfaces. This reduces the total drag especially the skin friction component while the lift is maintained or maximized. The results demonstrate the capability and accuracy of the developed adjoint-based optimization framework to design new NLF airfoils.

Finally, chapter 7 concludes the present research and provides a list of possible future works.

CHAPTER 2

The Navier-Stokes, $k-\omega$ SST Turbulence Model, and $\gamma-\tilde{R}e_{\theta t}$ Transition Model Equations

2.1 Introduction

This chapter presents the integral and conservative forms of the governing equations. Furthermore the temporal and spatial discretization of the convective, viscous, and artificial dissipative fluxes of the Navier-Stokes equations are explained as well as the convergence acceleration techniques. Finally the $\gamma-\tilde{R}e_{\theta t}$ transition and $k-\omega$ SST turbulence models and their corresponding discretization are described.

2.2 Navier-Stokes Equations

By applying the conservation of mass, momentum, and energy principles to a control system, the Navier-Stokes equations are obtained [36]. The Navier-Stokes equations which govern the motion of fluid elements in a continuum space, are a set of non-linear partial differential equations (PDEs) and together with thermodynamic relations describe the fluid properties such as density, velocity, pressure, and temperature in any point of the flow field [11]. To evaluate these dynamic and thermodynamic properties at a fixed position in the flow field, the Reynolds transport theorem (RTT) is employed to convert the temporal derivative from a Lagrangian approach into an Eulerian form [44]. The following equation demonstrates the transformation as,

$$\begin{aligned}\frac{DB_{\text{system}}}{Dt} &= \frac{D}{Dt}\int_{V(t)} \beta \; dV \\ &= \frac{\partial}{\partial t}\int_{V(t)} \beta dV + \int_{A(t)} \beta \vec{U}.\vec{n} \; dA,\end{aligned}$$

where $B_{\text{system}} = \int_{V(t)} \beta \; dV$ and β is the transported property of the system per unit volume, t is time, V is volume, A is area, and $\vec{U}$ is the velocity vector. By using Gauss's theorem [44], the surface integral is converted to a volume integral as follows,

$$\frac{D}{Dt}\int_{V(t)} \beta \; dV = \int_{V(t)} \left[\frac{\partial \beta}{\partial t} + \left(\vec{\nabla} \cdot \beta \vec{U}\right)\right] \; dV.$$

2.2.1 Conservation of mass

The continuity or conservation of mass states that the mass inside a control system is neither produced nor destroyed and is mathematically presented as follows

$$\frac{D}{Dt}\int_{v(t)} \rho \; dV = 0,$$

which implies that the time rate of change of mass inside the system and volume, V, are zero. By employing the Reynolds transport theorem the above equation is transformed to

$$\frac{D}{Dt}\int_{v(t)} \rho \; dV = \int_{v(t)} \left[\frac{\partial \rho}{\partial t} + \vec{\nabla}.\left(\rho \vec{U}\right)\right] \; dV = 0.$$

Expanding the divergence of $\rho\vec{U}$ and using the definition of the material derivative $\left(\frac{D\rho}{Dt} = \frac{\partial \rho}{\partial t} + \vec{U}.\vec{\nabla}\rho\right)$, the continuity equation is defined as follows,

$$\frac{D}{Dt}\int_{v(t)} \rho \, dV = \int_{v(t)} \left[\frac{D\rho}{Dt} + \rho\vec{\nabla}\cdot\vec{U}\right] \, dV = 0.$$

2.2.2 Conservation of momentum

Newton's second law states that the summation of the body and surface forces acting on a control system equals the time rate change of momentum [36] and is formulated as

$$\frac{D}{Dt}\int_{V(t)} \rho u_i \, dV = \int_{S(t)} T_i \, dS + \int_{V(t)} \rho G_i \, dV, \tag{2.1}$$

where u_i is the element of the velocity vector, $\vec{U}$, in the x_i direction. G_i is the body force per unit volume component and T_i is the surface force vector per unit surface area component in the x_i direction. Using the Reynolds transport theorem, the time rate of change of momentum is transformed to the material derivative form and equation (2.1) is defined for a control volume as

$$\int_{V(t)} \left[\frac{D\rho u_i}{Dt} + \rho u_i\vec{\nabla}\cdot\vec{U}\right] dV = \int_{S(t)} T_i \, dS + \int_{V(t)} \rho G_i \, dV.$$

The surface force vector component which is the sum of the hydrostatic pressure and viscous stress, is written as follows over the control surface, $S(t)$,

$$\int_{S(t)} T_i \, dS = \int_{S(t)} \left(-p\delta_{ki}n_k + \tau_{ki}n_k\right) \, dS,$$

where p is pressure and τ is the viscous stress tensor. For the Newtonian isotropic gas, there is a linear relationship between the stress tensor and the rate of deformation. Using the Stokes assumption, the viscous stress tensor is defined as

$$\tau_{ki} = \mu \left[\frac{\partial u_k}{\partial x_i} + \frac{\partial u_i}{\partial x_k} \right] - \frac{2}{3} \mu \left[\frac{\partial u_j}{\partial x_j} \right] \delta_{ki}.$$

By applying Gauss's theorem [44], the surface integral of the surface forces component, T_i, is converted to a volume integral

$$\int_{S(t)} T_i \; dS = \int_{V(t)} \left(- \frac{\partial p}{\partial x_i} + \frac{\partial \tau_{ki}}{\partial x_k} \right) \; dV,$$

and finally the integral form of the conservation of momentum is obtained

$$\int_{V(t)} \left[\frac{D \rho u_i}{Dt} + \rho u_i \vec{\nabla} \cdot \vec{U} + \frac{\partial p}{\partial x_i} - \frac{\partial \tau_{ki}}{\partial x_k} - \rho G_i \right] \; dV = 0.$$

2.2.3 Conservation of energy

According to the first law of thermodynamics [44], the following four items affect the rate of change of energy in volume

- rate of work done by surface forces per unit area $\left(\int_{S(t)} T_k u_k \; dS \right)$,
- rate of work done by body forces per unit volume $\left(\int_{V(t)} \rho G_k u_k \; dV \right)$,
- rate of heat source addition into the volume $\left(\int_{V(t)} Q \; dV \right)$,
- and rate of heat loss through the control surface $\left(- \int_{S(t)} q_k n_k \; dS \right)$. The heat flux, q_k, is calculated by Fourier's law of heat conduction

  $$q_k = -\kappa \frac{\partial T}{\partial x_k},$$

  where κ is the coefficient of thermal conductivity.

Therefore the conservation of energy equation is written as follows for a control system

$$\frac{D}{Dt}\int_{V(t)} \rho \left(e + \frac{U^2}{2}\right) = \int_{S(t)} T_k u_k \; dS + \int_{V(t)} \rho G_k u_k \; dV - \int_{S(t)} q_k n_k \; dS + \int_{V(t)} Q \; dV,$$

where e is the internal energy and U is the magnitude of the velocity vector. The Reynolds transport theorem is applied to convert the rate of change of energy of the system into the material derivative form and then all surface integrals are converted into volume integrals using the Gauss theorem. The conservation of energy equation finally is presented as follows,

$$\int_{V(t)} \left[\frac{D\rho\left(e + \frac{U^2}{2}\right)}{Dt} + \rho\left(e + \frac{U^2}{2}\right)\vec{\nabla}\cdot\vec{U} + \frac{\partial}{\partial x_k}\left(-\sigma_{ki}u_i + q_k\right) - \rho G_k u_k - Q \right] dV = 0.$$

2.3 Conservative form of the Navier-Stokes equations

Collecting the integral form of the conservation equations yields the complete system for the Navier-Stokes equations [36, 44]. The Cartesian coordinates and velocity components are denoted by (x_1, x_2) and (u_1, u_2) respectively. By using Einstein's notation the two-dimensional equations take the form

$$\frac{\partial \vec{w}}{\partial t} + \frac{\partial \vec{f}_i}{\partial x_i} - \frac{\partial \vec{f}_{vi}}{\partial x_i} = 0 \;\text{ in }\; D, \tag{2.2}$$

where the state vector, $\vec{w}$, inviscid flux vector, $\vec{f}$, and viscous flux vector, $\vec{f}_v$, are described respectively by

$$\vec{w} = \begin{pmatrix} \rho \\ \rho u_1 \\ \rho u_2 \\ \rho E \end{pmatrix}, \quad \vec{f_i} = \begin{pmatrix} \rho u_i \\ \rho u_1 u_i + p\delta_{i1} \\ \rho u_2 u_i + p\delta_{i2} \\ \rho E u_i + p u_i \end{pmatrix}, \quad \vec{f_{vi}} = \begin{pmatrix} 0 \\ \tau_{ij}\delta_{j1} \\ \tau_{ij}\delta_{j2} \\ u_j\tau_{ij} + k\frac{\partial T}{\partial x_i} \end{pmatrix},$$

where ρ and E are density and specific total energy, and δ_{ij} is the Kronecker delta function [44]. The pressure, p, is computed through the state equation.

$$p = (\gamma - 1)\,\rho\left\{E - \frac{1}{2}(u_i u_i)\right\},$$

where γ is the specific heat ratio. The ideal gas state equation specifies the relation between temperature, T, and pressure, p,

$$p = \rho R T,$$

where R is the gas constant. The viscous stresses, τ_{ij}, are written as

$$\tau_{ij} = (\mu + \mu_t)\left[\left(\frac{\partial u_i}{\partial x_j} + \frac{\partial u_j}{\partial x_i}\right) - \frac{2}{3}\left(\frac{\partial u_k}{\partial x_k}\right)\delta_{ij}\right],$$

where μ is the molecular viscosity and μ_t is the turbulent eddy viscosity which is provided by using a turbulence model as will be discussed in section 2.9. For moderate temperatures, the molecular viscosity for air, can be obtained from the Sutherland equation

$$\mu = C_1 \frac{T^{\frac{3}{2}}}{T + C_2},$$

where $C_1 = 1.458 \times 10^{-6}\mathrm{kg}/(\mathrm{ms}\sqrt{\mathrm{K}})$ and $C_2 = 110.4\mathrm{K}$.The thermal conductivity coefficient, κ, relates the temperature gradient and heat flux. It is computed as follows

$$\kappa = \frac{c_p \mu}{Pr},$$

where c_p is the specific heat at constant pressure and Pr is the Prandtl number.

2.4 Boundary conditions

The wall boundary conditions for viscous flows must satisfy the no-slip and no-injection conditions; the normal and tangential components of the velocity vector over the wall surface are zero

$$\vec{U}.\vec{n} = 0, \qquad \text{and} \qquad \vec{U}.\vec{t} = 0,$$

where $\vec{n}$ and $\vec{t}$ are the normal and tangential unit vectors respectively. These equations imply that the velocity on the wall must be zero. To satisfy the energy equation on the wall boundary, the adiabatic or isothermal boundary condition is employed. Since in the present work the heat flux through the wall is zero, the adiabatic wall condition is used and defined as follows

$$\vec{q}.\vec{n} = 0.$$

Since in computational fluid dynamics the domain is finite, the boundary conditions at the far-field boundary must be defined in order to solve the Navier-Stokes equations. By determining the inflow and outflow boundaries, the corresponding properties to the inward waves must be specified [44]. More explanation about this procedure can be found in subsection 2.5.5.

2.5 Numerical Discretization

The Navier-Stokes equations are one of the most difficult partial differential systems of equations where analytical solutions are available only for selected simple problems. To solve more complicated problems, researchers convert this set of nonlinear partial differential equations into a set of algebraic equations using numerical discretization schemes in order to solve them computationally. Two issues need to be addressed to numerically solve a partial differential equation; first, the generation of a mesh of discrete points where the numerical equations are evaluated; second, the manner in which the equations are numerically discretized and solved until a converged solution is obtained. In this work, a structured grid and a second-order finite-volume method is employed together with both explicit and implicit solvers to march the equations to a steady state solution. This method has the ability to be applied on any complex grid and preserves all conservation laws locally and globally. Details about the numerical scheme and methods of convergence acceleration will be discussed in the following subsections.

2.5.1 Finite-Volume Method

In the present work the integral form of the conservation equations are discretized by using a finite-volume method. To solve the Reynolds-averaged Navier-Stokes (RANS) equations (2.2) on a body conforming structured grid, the following metrics are used to transfer the physical domain to the computational coordinates (ξ_1, ξ_2) [17, 44],

$$K_{ij} = \left[\frac{\partial x_i}{\partial \xi_i}\right], \qquad J = \det\left(K\right), \qquad K_{ij}^{-1} = \left[\frac{\partial \xi_i}{\partial x_i}\right].$$

In the computational domain the governing equations are defined as

$$\frac{\partial\left(J\vec{w}\right)}{\partial t} + \frac{\partial\left(\vec{F}_i - \vec{F}_{v_i}\right)}{\partial \xi_i} = 0 \quad \text{in} \quad D.$$

Considering $S_{ij} = JK_{ij}^{-1}$ as the projection of the ξ_i cell face along the x_j axis, the convective and viscous flux contributions in the computational space are defined by $\vec{F}_i = S_{ij}\vec{f}_j$ and $\vec{F}_{vi} = S_{ij}\vec{f}_{v_j}$ respectively. In the following subsections the (x, y) and (ξ, η) are used as the two-dimensional physical and computational coordinates respectively.

2.5.2 Discretization of Convective Fluxes

In order to discretize the convective fluxes for cell (i, j), the derivatives of the flux, $\vec{f}_i$, are evaluated in both computational directions (ξ, η) [44]. In each direction the derivative at the cell center, in the computational domain, is calculated by subtracting the inviscid fluxes of the adjacent cell faces

$$\frac{\partial \vec{F}_1}{\partial \xi_1} = \vec{F}_{1_{i+\frac{1}{2},j}} - \vec{F}_{1_{i-\frac{1}{2},j}},$$

where $(i \pm \frac{1}{2}, j)$ indices denote the cell face centers as shown in figure 2–1 . In each computational direction the average inviscid fluxes of the neighbouring cell centers are used as follows,

$$\vec{f}_{i+\frac{1}{2},j} = \frac{1}{2}\left(\vec{f}^{+}_{i+1,j} + \vec{f}^{-}_{i,j}\right).$$

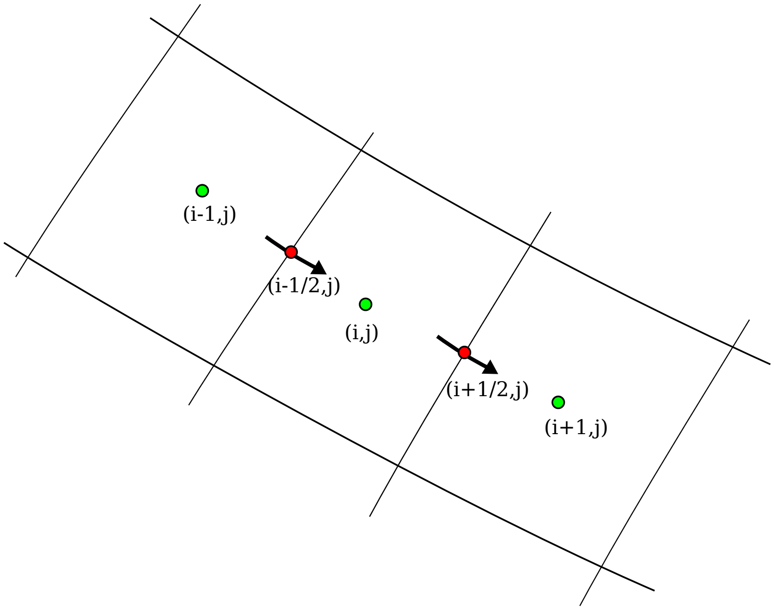

Figure 2–1: Inviscid Computational Stencil

Considering the cell based finite-volume method employed in this work, the information is stored at the cell centres and the flux vectors are stated as

$$\vec{f}^{+}_{i+1,j} = \begin{pmatrix} \rho_{i+1,j} q^{+} \\ (\rho u)_{i+1,j} q^{+} + y_{\eta_{i+\frac{1}{2},j}} p_{i+1,j} \\ (\rho v)_{i+1,j} q^{+} - x_{\eta_{i+\frac{1}{2},j}} p_{i+1,j} \\ (\rho E + p)_{i+1,j} q^{+} \end{pmatrix}, \quad \text{and} \quad \vec{f}^{-}_{i,j} = \begin{pmatrix} \rho_{i,j} q^{-} \\ (\rho u)_{i,j} q^{-} + y_{\eta_{i+\frac{1}{2},j}} p_{i,j} \\ (\rho v)_{i,j} q^{-} - x_{\eta_{i+\frac{1}{2},j}} p_{i,j} \\ (\rho E + p)_{i,j} q^{-} \end{pmatrix},$$

where $q^{\pm}$ are the flux velocities. They are calculated by using the metrics of transformation and the velocity components in the physical domain,

$$q^{+}=\frac{y_{\eta_{i+\frac{1}{2},j}}(\rho u)_{i+1,j}-x_{\eta_{i+\frac{1}{2},j}}(\rho v)_{i+1,j}}{\rho_{i+1,j}},\quad\text{and}\quad q^{-}=\frac{y_{\eta_{i+\frac{1}{2},j}}(\rho u)_{i,j}-x_{\eta_{i+\frac{1}{2},j}}(\rho v)_{i,j}}{\rho_{i,j}}.$$

2.5.3 Discretization of Viscous Flux

In order to discretize the viscous flux for the cell (i,j) a second-order central difference approach is employed for the second derivatives of the velocity and temperature [44]. To compute the viscous fluxes, $\vec{f}_{v_{i+\frac{1}{2},j}}$ and $\vec{g}_{v_{i+\frac{1}{2},j}}$, on the face centers the following mathematical procedure is applied

$$\vec{f}_{v_{i+\frac{1}{2},j}}=\frac{1}{2}\left(\vec{f}_{v_{i+\frac{1}{2},j+\frac{1}{2}}}+\vec{f}_{v_{i+\frac{1}{2},j-\frac{1}{2}}}\right),\quad\text{and}\quad \vec{g}_{v_{i+\frac{1}{2},j}}=\frac{1}{2}\left(\vec{g}_{v_{i+\frac{1}{2},j+\frac{1}{2}}}+\vec{g}_{v_{i+\frac{1}{2},j-\frac{1}{2}}}\right),$$

where $\vec{f}_{v_{i+\frac{1}{2},j\pm\frac{1}{2}}}$ and $\vec{g}_{v_{i+\frac{1}{2},j\pm\frac{1}{2}}}$ represent the viscous fluxes calculated on the vertices of the cell. The viscous fluxes are then evaluated in the computational domain as,

$$\vec{F}_{v_{i+\frac{1}{2},j}}=y_{\eta_{i+\frac{1}{2}},j}\vec{f}_{v_{i+\frac{1}{2}}}+x_{\eta_{i+\frac{1}{2},j}}\vec{g}_{v_{i+\frac{1}{2}}}.$$

To discretize and evaluate the viscous fluxes at the cell vertices, four cells that share a vertex construct an auxiliary control volume, where its vertices are the cell centers of the four mentioned cells. The auxiliary control volumes with cell centers $\left(i+\frac{1}{2},j+\frac{1}{2}\right)$ and $\left(i+\frac{1}{2},j-\frac{1}{2}\right)$ are shown in figure 2–2. The viscous fluxes in the physical domain for the node $\left(i+\frac{1}{2},j+\frac{1}{2}\right)$ are written as

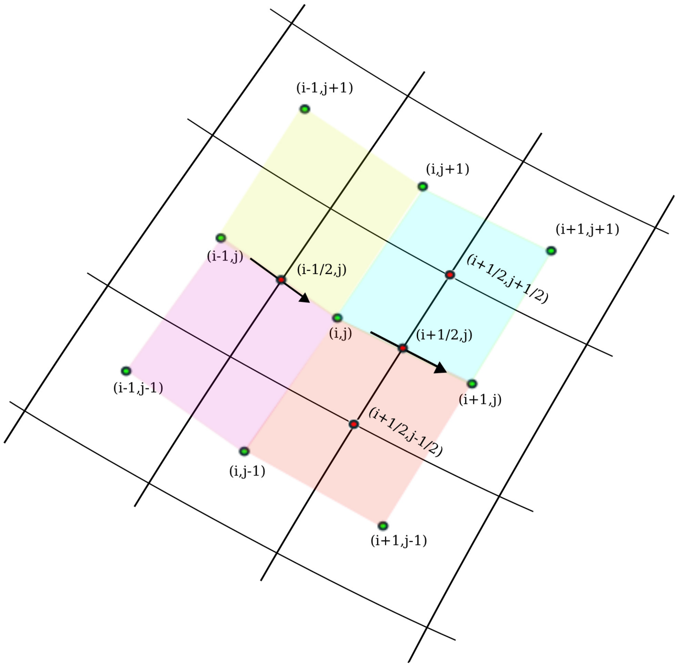

Figure 2–2: Viscous Computational Stencil

$$\vec{f}_{v_{i+\frac{1}{2},j+\frac{1}{2}}} = \begin{pmatrix} 0 \\ \tau_{xx} \\ \tau_{xy} \\ u\tau_{xx} + v\tau_{xy} + k\frac{\partial T}{\partial x} \end{pmatrix}_{i+\frac{1}{2},j+\frac{1}{2}} , \quad \text{and} \quad \vec{g}_{v_{i+\frac{1}{2},j+\frac{1}{2}}} = \begin{pmatrix} 0 \\ \tau_{yx} \\ \tau_{yy} \\ u\tau_{yx} + v\tau_{yy} + k\frac{\partial T}{\partial y} \end{pmatrix}_{i+\frac{1}{2},j+\frac{1}{2}} ,$$

where τ_{xx}, τ_{yy}, and $\tau_{xy}\,(=\tau_{yx})$ are the normal and shear stress tensors respectively. For example the normal stress tensor for the node $\left(i+\frac{1}{2}, j+\frac{1}{2}\right)$ is presented as

$$\tau_{xx_{i+\frac{1}{2},j+\frac{1}{2}}} = 2\mu_{i+\frac{1}{2},j+\frac{1}{2}} \left[\frac{\partial u}{\partial x}\right]_{i+\frac{1}{2},j+\frac{1}{2}} - \frac{2}{3}\mu_{i+\frac{1}{2},j+\frac{1}{2}} \left\{\left[\frac{\partial u}{\partial x}\right] + \left[\frac{\partial v}{\partial y}\right]\right\}_{i+\frac{1}{2},j+\frac{1}{2}} .$$

The flow field properties such as velocity components, u, v, and the thermodynamics properties such as thermal conductivity coefficient, k, and temperature, T, are being averaged from the neighbouring cell centres [44]. For example

$$T_{i+\frac{1}{2},j+\frac{1}{2}} = \frac{1}{4}\left(T_{i+1,j+1} + T_{i+1,j} + T_{i,j+1} + T_{i,j}\right).$$

In order to evaluate the velocity gradients, the auxiliary control volume illustrated in figure 2–2 is used. By employing the metrics of transformation, the velocity derivative in the physical domain is written based on the velocity gradients of the computational domain as follows

$$\left(\frac{\partial u}{\partial x}\right)_{i+\frac{1}{2},j+\frac{1}{2}} = \frac{1}{J_{i+\frac{1}{2},j+\frac{1}{2}}}\left[\left(\frac{\partial u}{\partial \xi}\right)_{i+\frac{1}{2},j+\frac{1}{2}} y_{\eta_{i+\frac{1}{2},j+\frac{1}{2}}} + \left(\frac{\partial u}{\partial \eta}\right)_{i+\frac{1}{2},j+\frac{1}{2}} y_{\xi_{i+\frac{1}{2},j+\frac{1}{2}}}\right],$$

where the velocity gradients in the computational coordinates, $\left(\frac{\partial u}{\partial \xi}\right)_{i+\frac{1}{2},j+\frac{1}{2}}$ and $\left(\frac{\partial u}{\partial \eta}\right)_{i+\frac{1}{2},j+\frac{1}{2}}$, are described as

$$\begin{aligned}\left(\frac{\partial u}{\partial \xi}\right)_{i+\frac{1}{2},j+\frac{1}{2}} &= \frac{(u_{i+1,j+1} - u_{i,j+1}) + (u_{i+1,j} - u_{i,j})}{2}, \quad \text{and}\\ \left(\frac{\partial u}{\partial \eta}\right)_{i+\frac{1}{2},j+\frac{1}{2}} &= \frac{(u_{i+1,j+1} - u_{i+1,j}) + (u_{i,j+1} - u_{i,j})}{2}.\end{aligned}$$

The average velocity differences of the auxiliary control volume (figure 2–2) are employed to calculate the derivatives.

2.5.4 Numerical Dissipation

Introducing numerical dissipation into the convective and viscous fluxes stabilizes the numerical scheme of the discretized Navier-Stokes equations [17, 44]. In the present work the Jameson-Schmidt-Turkel (JST) scheme [27, 17] is employed. This scheme which is a combination of first- and third-order terms, is defined as,

$$\vec{d} = \epsilon^{(2)} \Delta x^3 \frac{\lambda}{p} \left| \frac{\partial^2 p}{\partial x^2} \right| \frac{\partial \vec{w}}{\partial x} - \epsilon^{(4)} \Delta x^3 \lambda \frac{\partial^3 \vec{w}}{\partial x^3},$$

where $\epsilon^{(2)}$ and $\epsilon^{(4)}$ are constants and λ is the eigenvalue vector of the Jacobian matrix of the Navier-Stokes equations. In the discrete form, this artificial flux for the node $\left(i+\frac{1}{2}, j\right)$ is defined as

$$\vec{d}_{i+\frac{1}{2},j} = \vec{d}^{(2)}_{i+\frac{1}{2},j} - \vec{d}^{(4)}_{i+\frac{1}{2},j},$$

where the first term is the first-order and the latter is the third-order component. The $\vec{d}^{(2)}_{i+\frac{1}{2},j}$ term is stated as

$$\vec{d}^{(2)}_{i+\frac{1}{2},j} = \nu^{(2)} \frac{1}{2} \left(\tilde{\lambda}_{\xi_{i+1,j}} + \tilde{\lambda}_{\xi_{i,j}} \right) \left(\vec{w}_{i+1,j} - \vec{w}_{i,j} \right),$$

where, λ is the scaled spectral radii of the Navier-Stokes equations [44]. These scaled parameters are defined as follows

$$\tilde{\lambda}_\xi = \left[1 + \left(\frac{\lambda_\xi}{\lambda_\eta} \right)^{\frac{2}{3}} \right] \lambda_\xi, \qquad \tilde{\lambda}_\eta = \left[1 + \left(\frac{\lambda_\eta}{\lambda_\xi} \right)^{\frac{2}{3}} \right] \lambda_\eta,$$

and are employed to improve the convergence of the solver on highly stretched grids [44]. The $\nu^{(2)}_{i,j}$ term is proportional to the pressure gradient and defined as

$$\nu^{(2)}_{i,j} = \max\left(\sigma_{i,j}, \sigma_{i+1,j}\right), \quad \text{and} \quad \sigma_{i,j} = \frac{|p_{i+1,j} - 2p_{i,j} + p_{i-1,j}|}{p_{i+1,j} - 2p_{i,j} + p_{i-1,j}}.$$

In the high pressure gradient regions such as shock waves, this term increases the dissipation and stabilizes the numerical solution by changing the unstable central scheme into an upwind biasing algorithm around discontinuities [27, 44]. The third-order dispersive term is defined as follows

$$\vec{d}^{(4)}_{i+\frac{1}{2},j} = \nu^{(4)}\Lambda_{i+\frac{1}{2},j}\left(\vec{w}_{i+2,j} - 3\vec{w}_{i+1,j} + 3\vec{w}_{i,j} - \vec{w}_{i-1,j}\right),$$

where

$$\nu^{(4)} = \max\left[0, \left(\frac{1}{32} - \nu^{(2)}\right)\right].$$

Since the third-order term has the tendency to introduce oscillations around discontinuities such as shock waves, the $\nu^{(4)}$ coefficient activates it only over smooth regions of the flow [44].

2.5.5 Discrete Boundary Conditions

In the following subsections the far-field and wall boundary conditions are discussed in the discrete form. In order to achieve reasonable convergence of the numerical solution of the discretized equations, some constraints on the theoretical definition of the boundary conditions are sometimes considered [44].

- Wall boundary

  The wall boundary conditions are imposed on the surface of the body. In this work, no-slip wall boundary conditions are applied [11, 17, 44].

- Far-field boundary

  The far-field boundary conditions are imposed based on Riemann invariants. In order to extrapolate the velocity components for far-field ghost and interior cells, the outgoing and inward characteristic waves are respectively calculated based on the specified boundary conditions [11]. The details about the far-field boundary conditions are explained in reference [17].

2.6 Time Integration Method

In order to reach a steady state solution, a time integration method must be employed to march the solution in time. A modified version of the Runge-Kutta algorithm [38] which has second-order accuracy [44], is used in this research. The residual of the Navier-Stokes equations is evaluated in several stages inside the real time interval between $n\Delta t$ and $(n+1)\,\Delta t$ as follows,

$$\begin{aligned}
\vec{w}^{(0)} &= \vec{w}^{(n)} \\
\vec{w}^{(1)} &= \vec{w}^{(0)} - \alpha_1 \Delta t \vec{R}\left(w^{(0)}\right) \\
&\vdots \\
\vec{w}^{(k)} &= \vec{w}^{(0)} - \alpha_k \Delta t \vec{R}\left(w^{(k-1)}\right); \quad k = 1, 2, \ldots, M \\
&\vdots \\
\vec{w}^{(n+1)} &= \vec{w}^{(M)},
\end{aligned}$$

where M is the number of stages. The Runge-Kutta algorithm combines these computed residuals at different stages in order to construct a second-order approach in time. The stability of the numerical scheme is augmented by modifying the convective and dissipative fluxes in every stage of the Runge-Kutta algorithm. In the present work, a five stage modified Runge-Kutta algorithm [38] is used for the time integration where in each stage the dissipative and convective fluxes are treated as follows

$$\begin{aligned}
\vec{R}^{(k)} &= \vec{C}^{(k)} + \vec{D}^{(k)} \\
\vec{C}^{(k)} &= \vec{C}\left(w^{(k)}\right) \\
\vec{D}^{(k)} &= \beta_k \vec{D}\left(w^{(k)}\right) + \left(1-\beta_k\right)\vec{D}\left(w^{(k-1)}\right).
\end{aligned}$$

The β_k coefficients are defined as below in order to increase the stability of the equations along the real axis.

$$\beta_1 = 1, \quad \beta_2 = 0, \quad \beta_3 = 0.56 \quad \beta_4 = 0, \quad \beta_5 = 0.44.$$

The α_k coefficients are chosen as

$$\alpha_1 = \frac{1}{4}, \quad \alpha_2 = \frac{1}{6}, \quad \alpha_3 = \frac{3}{8}, \quad \alpha_4 = \frac{1}{2}, \quad \alpha_5 = 1.$$

The coefficients assure the maximum stability along the imaginary axis.

2.7 Convergence Acceleration Techniques

Three different techniques are employed to increase the convergence rate and reduce the required time to reach a steady state solution. These methods include local time stepping, residual averaging, and multigrid. Details on these methods are excluded in this thesis and can be found in reference [44].

2.8 Flow Preconditioning

At the limit of the incompressible flow regime, compressible flow solvers suffer from the ill-conditioned nature of the governing equations and the low accuracy of the poorly scaled artificial dissipation fluxes [47]. These two effects reduce the convergence rate of the flow solver. To improve the accuracy and convergence of the solver for incompressible cases, the Weiss-Smith preconditioner is used [47]. By multiplying the Weiss-Smith preconditioner matrix, the convective and dissipative fluxes are augmented in order to improve the condition number and stiffness of the governing equations. This restores the accuracy and convergence of the compressible flow solver as the Mach number approaches zero. This preconditioner matrix which augments the Jacobian matrix of the Navier-Stokes equations, is expressed in entropy form as follows

$$P_S = \begin{pmatrix} \beta & 0 & 0 & 0 \\ 0 & 1 & 0 & 0 \\ 0 & 0 & 1 & 0 \\ 0 & 0 & 0 & 1 \end{pmatrix},$$

where β is a constant in the order of the square of the Mach number ($\beta = O\left(M^2\right)$). By applying the transformation matrices [47], the preconditioner matrix is converted into the conservative flow variable form $\left(P = T_{SC}^T P_S T_{CS}^T\right)$ [47]. Consequently, this matrix is pre-multiplied by the Jacobian matrix of the Navier-Stokes equations as follows

$$
\begin{aligned}
P^{-1}\frac{\partial \vec{w}}{\partial t} + \frac{\partial \vec{F}_i}{\partial \xi_i} &= 0,\\
P^{-1}\frac{\partial \vec{w}}{\partial t} + A\frac{\partial \vec{w}}{\partial \xi_i} &= 0,\\
\frac{\partial \vec{w}}{\partial t} + PA\frac{\partial \vec{w}}{\partial \xi_i} &= 0.
\end{aligned}
$$

To scale the preconditioned fluxes for the artificial dissipation terms, the inverse of the preconditioning matrix augments the dissipative fluxes as follows

$$\vec{d} = P^{-1}\left[\epsilon^{(2)}\Delta x^3 \frac{\lambda}{p}\left|\frac{\partial^2 p}{\partial x^2}\right|\frac{\partial \vec{w}}{\partial x} - \epsilon^{(4)}\Delta x^3 \lambda \frac{\partial^3 \vec{w}}{\partial x^3}\right].$$

2.9 Turbulence Model

The eddy viscosity in the RANS equations can be computed by various types of turbulence models such as algebraic, one-equation, and two-equation models. In the present work, a modified form of the $k - \omega$ SST model originally proposed by Menter [39], has been employed. The conservative form of the $k - \omega$ SST-sust turbulence model [55] which is suitable for external flows, is as follows,

$$\frac{D\rho k}{Dt} = \tau_{ij}\frac{\partial u_i}{\partial x_j} - \beta^* \rho\omega k + \frac{\partial}{\partial x_j}\left[(\mu + \sigma_k \mu_t)\frac{\partial k}{\partial x_j}\right] + \beta^* \rho \omega_\infty k_\infty, \tag{2.3}$$

$$\frac{D\rho\omega}{Dt} = \frac{\gamma}{\nu_t}\tau_{ij}\frac{\partial u_i}{\partial x_j} - \beta\rho\omega^2 + \frac{\partial}{\partial x_j}\left[(\mu + \sigma_k\mu_\omega)\frac{\partial \omega}{\partial x_j}\right] + 2(1-F_1)\frac{\rho\sigma_{\omega 2}}{\omega}\frac{\partial k}{\partial x_j}\frac{\partial \omega}{\partial x_j} + \beta\rho\omega_\infty^2, \tag{2.4}$$

where k is turbulent kinetic energy and ω is specific dissipation. Every term of the $k-\omega$ SST-sust turbulence model is identical to the Menter's standard $k-\omega$ SST turbulence model [39] except the last terms. These ambient terms eliminate the non-physical decay of the turbulence variables at the far-field boundary. The F_1 blending function is defined as

$$F_1 = \tanh\left(\text{arg}_1^4\right), \tag{2.5}$$

where

$$\text{arg}_1 = \min\left[\max\left(\frac{\sqrt{k}}{0.09\omega d}, \frac{500\nu}{d^2\omega}\right), \frac{4\rho\sigma_{\omega 2}k}{CD_{k\omega}d^2}\right].$$

In the above equation, d, is the minimum distance from the wall, and $CD_{k\omega}$ is defined as

$$CD_{k\omega} = \max\left(2\rho\sigma_{\omega 2}\frac{1}{\omega}\frac{\partial k}{\partial x_j}\frac{\omega}{x_j}, 10^{-20}\right).$$

This blending function gradually transforms the Wilcox $k-\omega$ in the near wall region into the standard $k-\epsilon$ model in the outer wake and free shear layer regions. By using the blending function, F_1, any constant ϕ, can be computed based on ϕ_1 from the Wilcox $k-\omega$ model and ϕ_2 from the standard $k-\epsilon$ model

$$\phi = F_1\phi_1 + (1 - F_1)\,\phi_2.$$

The, ϕ_1, can be any of the following constants from the Wilcox $k-\omega$ model

$$\sigma_{k1} = 0.85, \quad \sigma_{\omega 1} = 0.5, \quad \beta_1 = 0.075,$$
$$\beta^* = 0.09, \quad \kappa = 0.41, \quad \gamma_1 = \beta_1/\beta - \sigma_{\omega 1}\kappa^2/\sqrt{\beta^*},$$

and the ϕ_2 constant can be any of the standard $k-\epsilon$ model constants as follows

$$\sigma_{k2} = 1.0, \quad \sigma_{\omega 2} = 0.856, \quad \beta_2 = 0.0828,$$
$$\beta^* = 0.09, \quad \kappa = 0.41, \quad \gamma_2 = \beta_2/\beta - \sigma_{\omega 2}\kappa^2/\sqrt{\beta^*}.$$

The turbulent eddy viscosity, μ_t, is defined as follows

$$\mu_t = \frac{\rho a_1 k}{\max(a_1\omega, \Omega F_2)}. \tag{2.6}$$

In this definition Ω is the absolute value of vorticity and $a_1 = 0.31$. The function F_2 is given by

$$F_2 = \tanh\left(\arg_2^2\right), \tag{2.7}$$

where

$$\arg_2 = \max\left(\frac{2\sqrt{k}}{0.09\omega d}, \frac{500\nu}{d^2\omega}\right).$$

This function modifies the definition of the turbulent eddy viscosity in order to avoid the overprediction of the shear stress especially in the presence of adverse pressure gradients [39]. The recommended far-field boundary conditions are $k_{\text{far-field}} = 10^{-6} U_{\infty}^{2}$ and $\omega_{\text{far-field}} = \frac{5U_{\infty}}{L}$. The two constants for the wall boundary conditions are $k_{\text{wall}} = 0$ and $\omega_{\text{wall}} = 10 \frac{6\nu}{\beta_1 (\Delta d_1)^2}$. Since the turbulence model is solved decoupled from the flow solver, then equations (2.3) and (2.4) should be solved for primitive variables, k, and, ω.

2.10 Trnasitional Boundary Layer

A laminar boundary layer which usually forms in low Reynolds number flows has a layer by layer structure. Each layer of the fluid slides over the adjacent layers and exchange of mass, momentum, or energy takes place in microscopic scales between the adjacent layers [18]. On the other hand, in a turbulent boundary forming in high Reynolds numbers, the exchange of mass, momentum, or energy happens between several layers. The fluid particles can move between the flow layers randomly and in macroscopic scales to form the eddies [18]. As a result of the intense mixing in a turbulent boundary layer, the gradient of the velocity profile is steeper and consequently the turbulent shear stress is larger; therefore turbulent boundary layers are more dissipative and the thickness of the boundary layer is greater than that of laminar flows [18].

Transition from laminar to turbulent flow are due to diverse reasons and through various processes. The following items can trip a laminar to a fully turbulent boundary layer; high Reynolds number, adverse pressure gradient, freestream turbulence intensity, wall roughness, and temperature [30] are just some but are the most important causes of boundary layer transition. The transition process can be gradually completed during the growth of Tollmien-Schlichting (T-S) wave instabilities, bypass transition, separated flow transition, and wake induced transition [30]. When the freestream turbulence intensity is less than 1%, the two-dimensional Tollmien-Schlichting (T-S) waves grow linearly along the boundary layer and their behaviour gradually becomes nonlinear and finally changes to three-dimensional disturbances. These disturbances produce the turbulent spots that merge and form a fully turbulent boundary layer.

In three-dimensional boundary layers where the flow direction is not perpendicular to the field isobars such as that found on swept wings, crossflow instability instead of streamwise (T-S) is the primary transition mechanism [58]. Crossflow instability waves are formed due to surface roughness or high freestream turbulence intensity and the unstable modes of these waves grow due to the adverse crossflow pressure gradient [58]. The evolution of the crossflow (CF) instabilities is similar to the growth of Tollmien-Schlichting (T-S) waves in two-dimensional boundary layers. High level of freestream turbulence intensity ($1\% \leq Tu$) can bypass the early stages of natural transition. In bypass transition, after the formation of the turbulent spots, a fully turbulent flow is produced by the coalescence of these spots. In separated flow transition, the low momentum laminar boundary layer separates and forms a laminar separation bubble (LSB). Based on inviscid instability theory [50], the produced laminar shear layer becomes unstable and transition to turbulent flow occurs. Because of the presence of a pressure gradient, this transitional shear layer is re-energized and reattaches as a fully turbulent flow. The wake induced transition occurs when a turbulent wake flow contaminates a laminar boundary layer, by increasing the freestream turbulence intensity to trip the boundary layer to a fully turbulent regime. For example the turbulent wake behind a wind turbine tower can contaminate the laminar flow over the downstream wind turbine blades [5].

2.11 Transition Model

The $\gamma - \tilde{Re}_{\theta t}$ correlation-based transition model has been designed to predict the transition region from laminar to turbulent flows using local flow variables [30, 37]. Menter et al. [31, 40, 41] first presented this model for transitional flows in various engineering applications. Recently Langtry et al. [32] published the modified version of the $\gamma - \tilde{Re}_{\theta t}$ transition model with a complete set of correlations for general use in modern CFD codes. In this model, a transport equation is solved for the turbulence intermittency (γ) and another for the transport of the momentum-thickness Reynolds number ($\tilde{Re}_{\theta t}$),

$$\frac{D\rho\gamma}{Dt} = P_\gamma - D_\gamma + \frac{\partial}{\partial x_j}\left[\left(\mu + \frac{\mu_t}{\sigma_f}\right)\frac{\partial \gamma}{\partial x_j}\right],$$

$$\frac{D\rho\tilde{Re}_{\theta t}}{Dt} = P_\theta - \frac{\partial}{\partial x_j}\left[\sigma_{\theta t}\left(\mu + \mu_t\right)\frac{\partial \tilde{Re}_{\theta t}}{\partial x_j}\right].$$

Similar to the turbulence model, the left-hand-side of the transition model equations includes the unsteady and advection terms. The production of the turbulence intermittency factor, P_γ, is defined as

$$P_\gamma = F_{\text{length}} c_{a1} \rho S [\gamma F_{\text{onset}}]^{0.5} (1 - c_{e1}\gamma).$$

This term employs F_{length} which is an empirical correlation to control the length of the transition process [32], and defined as,

$$F_{\text{length}} = \begin{cases} 398.189e^{-1} - 119.270e^{-4}\tilde{Re}_{\theta t} - 132.567e^{-6}\tilde{Re}_{\theta t}^{2} & \tilde{Re}_{\theta t} < 400, \\ 263.404 - 123.939e^{-2}\tilde{Re}_{\theta t} + 194.548e^{-5}\tilde{Re}_{\theta t}^{2} - 101.695e^{-8}\tilde{Re}_{\theta t}^{3} & 400 \leq \tilde{Re}_{\theta t} < 596, \\ 0.5 - 3.0e^{-4}\left(\tilde{Re}_{\theta t} - 596.0\right) & 596 \leq \tilde{Re}_{\theta t} < 1200, \\ 0.3188 & 1200 \leq \tilde{Re}_{\theta t}. \end{cases}$$

To increase the accuracy of the prediction of the skin friction coefficient at high Reynolds numbers, the following modification of the F_{length} is applied,

$$F_{\text{length}} = F_{\text{length}}\left(1 - F_{\text{sublayer}}\right) + 40.0F_{\text{sublayer}},$$

where $F_{\text{sublayer}} = e^{-\left(\frac{R_\omega}{0.4}\right)^2}$, $R_\omega = \frac{\rho d^2 \omega}{500\mu}$, and d is the minimum distance from the wall. The function F_{onset} which is responsible for the location of the onset of transition from laminar to fully turbulent flow is described as,

$$F_{\text{onset}} = \max\left(F_{\text{onset2}} - F_{\text{onset3}}, 0\right).$$

The definition of F_{onset2} is

$$F_{\text{onset2}} = \min\left(\max\left(F_{\text{onset1}}, F_{\text{onset1}}^4\right), 2.0\right), \quad F_{\text{onset1}} = \frac{Re_v}{2.193Re_{\theta c}}, \tag{2.8}$$

where $Re_v = \frac{\rho d^2 S}{\mu}$ and S is the magnitude of the strain tensor. The following proposed correlation [32] is used to calculate, $Re_{\theta c}$ based on the local momentum thickness Reynolds number, $\tilde{Re}_{\theta t}$, as follows,

$$Re_{\theta c} = \begin{cases} \tilde{Re}_{\theta t} - \Big(396.035e^{-2} - 120.656e{-}4\tilde{Re}_{\theta t} & \\ +868.230e{-}6\tilde{Re}_{\theta t}^{2} - 696.506e^{-9}\tilde{Re}_{\theta t}^{3} + 174.105e^{-12}\tilde{Re}_{\theta t}^{4}\Big) & \tilde{Re}_{\theta t} \leq 1870, \\ \tilde{Re}_{\theta t} - \Big[593.11 + 0.482\left(\tilde{Re}_{\theta t} - 1870.0\right)\Big] & \tilde{Re}_{\theta t} > 1870. \end{cases}$$

The function F_{onset3} is

$$F_{\text{onset3}} = \max\left(1. - \left(\frac{R_T}{2.5}\right)^3, 0\right) \quad , \quad R_T = \frac{\rho k}{\mu\omega}.$$

The destruction of the intermittency factor is obtained by

$$D_\gamma = c_{a2}\rho\Omega\gamma F_{\text{turb}}(c_{e2}\gamma - 1),$$

where $F_{\text{turb}} = e^{-\left(\frac{R_T}{4}\right)^4}$ [31]. The following constants are used in the transport equation for the turbulence intermittency factor, γ

$$c_{e1} = 1.0, \quad c_{a1} = 2.0, \quad c_{e2} = 50, \quad c_{a2} = 0.06, \quad \sigma_f = 1.0.$$

The production term of the transport equation for the momentum thickness Reynolds number, P_θ, is given by

$$P_\theta = c_{\theta t}\frac{(\rho U)^2}{500\mu}(Re_{\theta t} - \tilde{Re}_{\theta t})(1 - F_{\theta t}).$$

This term keeps the transported variable, $\tilde{Re}_{\theta t}$, outside the boundary layer as much as possible, close to the correlated $Re_{\theta t}$, which is obtained as follows [32]

$$Re_{\theta t} = \begin{cases} \left[1173.51 - 589.428Tu + \frac{0.2196}{Tu^2}\right] F\left(\lambda_\theta\right) & Tu \leq 1.3, \\ 331.50\left[Tu - 0.5658\right]^{-0.671} F\left(\lambda_\theta\right) & Tu > 1.3. \end{cases} \tag{2.9}$$

In the above relation the turbulence intensity is defined as $Tu = 100\frac{\sqrt{2k/3}}{U}$ and $\lambda_\theta = \frac{\rho\theta^2}{\mu}\frac{dU}{ds}$ [32]. The function, $F(\lambda_\theta)$, is obtained by the following relations [32]

$$F(\lambda_\theta) = \begin{cases} 1 - \left[-12.986\lambda_\theta - 123.66{\lambda_\theta}^2 - 405.689{\lambda_\theta}^3\right] e^{-\left(\frac{Tu}{1.5}\right)^{1.5}} & \lambda_\theta \leq 0, \\ 1 + 0.275\left[1 - e^{(-35.0\lambda_\theta)}\right] e^{-\left(\frac{Tu}{0.5}\right)} & \lambda_\theta > 0. \end{cases}$$

To improve the robustness of the numerical solution of the transition model, the following limits are applied to some of the parameters

$$-0.1 \leq \lambda_\theta \leq 0.1, \qquad Tu \geq 0.027, \qquad Re_{\theta t} \geq 20.$$

Here the blending function, $F_{\theta t}$, which allows the diffusion of the $\tilde{Re}_{\theta t}$ over the entire domain is obtained by

$$F_{\theta t} = \min\left(\max\left(F_{\text{wake}} e^{-\left(\frac{y}{\delta}\right)^4}, 1.0 - \left[\frac{\gamma - 1/c_{e2}}{1.0 - 1/c_{e2}}\right]^2\right), 1.0\right),$$

where $\delta = \frac{375\mu\Omega}{\rho U^2} Re_{\theta t}$. The function F_{wake} which turns off the blending function in the wake of airfoils is described as

$$F_{\text{wake}} = e^{-\left(\frac{Re_\omega}{10^5}\right)^2}, \quad \text{and} \quad Re_\omega = \frac{\rho\omega\ y^2}{\mu}.$$

The constant coefficients of the transport equation for the $\tilde{Re}_{\theta t}$ are

$$c_{\theta t} = 0.03, \quad \text{and} \quad \sigma_{\theta t} = 2.0.$$

In order to increase the capability and improve the accuracy of the transition model to simulate laminar separation bubbles (LSB) and predict the separation-induced transition, the following modification is applied to the intermittency factor, γ

$$\gamma_{\text{eff}} = \max\left(\gamma, \gamma_{\text{sep}}\right).$$

The definition of the separation-induced intermittency factor, γ_{sep}, is

$$\gamma_{\text{sep}} = \min\left[2\max\left(0, \left(\frac{Re_v}{3.235 Re_{\theta c}}\right) - 1\right) F_{\text{reattach}}, 2\right] F_{\theta t}, \tag{2.10}$$

where $F_{\text{reattach}} = e^{-\left(\frac{R_T}{20}\right)^4}$ is responsible for the reattachment of the fully turbulent flow after the transition bubble.

At the outlet and wall boundaries, a zero-flux boundary condition is employed for both transition model equations. The turbulence intermittency factor at the inlet boundary is determined by $\gamma_{\text{inlet}} = 1.0$ and the $\tilde{Re}_{\theta t \text{inlet}}$ is computed from equation (2.9) based on the inlet turbulence intensity, Tu_{inlet}. [32].

2.11.1 Numerical Implementation of the Transition and Turbulence Models

The transition and turbulence models are solved decoupled from the governing equations of the flow field. The advection terms in the transition and turbulence equations are discretized by a first-order scheme while the dissipation and diffusion terms use a second-order numerical discretization. In order to increase the stability of the numerical solution of the transition and turbulence equations, a first-order artificial dissipation term is added to each equation. In two-dimensional space each equation of the discretized transition and turbulence models produces a pentadiagonal partial differential equation (PDE) system. To solve each pentadiagonal system implicitly, the alternating direction implicit (ADI) scheme is employed to split these systems of equations. In each direction the constructed tridiagonal system can be solved by using a direct method such as the Thomas algorithm [17]. The $k-\omega$ SST turbulence model and the $\gamma - \tilde{Re}_{\theta t}$ transition model equations are solved in every multigrid cycle of the RANS solver. The transition and turbulence models are only updated on the finest grid of a multigrid cycle and on the coarser grids the transition and turbulence variables are frozen and their restricted updated values on the finest grid are used.

2.11.2 Modifications to the $k-\omega$ SST Turbulence Model

The integration of the $\gamma - \tilde{Re}_{\theta t}$ transition model, requires modifications of the $k-\omega$ SST model to allow the turbulence model to be gradually activated along the boundary layer upon the onset of transition. The interaction of the $\gamma - \tilde{Re}_{\theta t}$ transition model with the $k-\omega$ SST turbulence model is through the following two modifications.

First, the production and destruction terms of the original transport equation for the turbulent kinetic energy are modified such that they are scaled by the effective turbulence intermittency factor, γ_{eff} to progressively increase the level of turbulent kinetic energy, k, along the boundary layer. The original production, P_k, and destruction, D_k, are redefined based on Langtry and Menter [32] as

$$\tilde{P_k} = \gamma_{\text{eff}} P_k, \qquad \tilde{D_k} = \min\left(\max\left(\gamma_{\text{eff}}, 0.1\right) D_k, 1.0\right),$$

where the production term, $P_\omega = \frac{\gamma}{\nu_t} P_k$, of the transport equation for the specific dissipation, ω, is determined based on the original, production term, P_k and is not modified by the transition model variables.

Second, the F_1 blending function in the cross diffusion term in the transport equation for ω, equation (2.4) is modified as follows

$$F_1 = \max\left(F_{1\mathrm{orig}}, F_3\right),$$

where $F_3 = e^{-\left(\frac{R_d}{120}\right)^8}$ and $R_d = \frac{\rho d \sqrt{k}}{\mu}$.

2.11.3 Proposed Modifications to the $\gamma - \tilde{Re}_{\theta t}$ Transition and $k - \omega$ SST Turbulence Models

The following modifications are applied to address three issues that were observed through our implementation of the $\gamma - \tilde{Re}_{\theta t}$ transition model.

- **New definition of the eddy viscosity**

  Fluctuations in the skin friction coefficients within the transition zone were observed for cases with stronger adverse pressure gradients typically due to an increase in the angle of attack. The fluctuations are caused by an over-prediction of the shear stress as the turbulence model is slowly beginning to be active since the intermittency factor is rapidly increasing to unity. In spite of providing a smooth skin friction coefficient in the fully turbulent regime, Menter's original definition (2.6) for the turbulence eddy viscosity results in fluctuations in the skin friction coefficients within the transition region. We employ the following modified definition by Malan et al. [37]

$$\mu_t = \rho k \cdot \min\left[\frac{1}{\max\left(\omega, SF_2/a_1\right)}, \frac{0.6}{\sqrt{3}S}\right],$$

where S is the magnitude of the strain tensor and the additional term places a further limit on the turbulent eddy viscosity. By using this definition the wall shear stress evolves smoothly through the transition process. The obtained total drag coefficients and the distribution of the skin friction coefficients, demonstrated in Chapter 5, are in good agreement with the experimental results for laminar-turbulent flows.

- **Treatment of the far-field boundary conditions**

  Numerical dissipation of the turbulence intensity from the inlet boundary to the leading edge of the airfoil was observed. This leads to a dissimilar turbulence intensity at the leading edge of the airfoil when compared to the experimental data. The freestream turbulence model variables, k_∞ and ω_∞, are computed based on standard definitions [59] from the freestream turbulence intensity, Tu_∞, and the ratio of the viscosities, $R_T = \left(\frac{\mu_t}{\mu}\right)_\infty$, as follows

$$k_\infty = (3/2)\left(Tu_\infty U_\infty\right)^2, \qquad \omega_\infty = \frac{\rho_\infty k_\infty}{R_T \mu_\infty}.$$

  However, they are further modified by the following relations [8]

$$\begin{aligned} \omega_\infty &= \left(\beta s/U_\infty + 1/\omega_\infty\right)^{-1}, \qquad (2.11) \\ k_\infty &= k_\infty \left(\beta \omega_\infty s/U_\infty\right)^{-\beta^*/\beta}, \end{aligned}$$

where s is the axial distance from the leading edge to the far-field (inlet) boundary cells and U_∞ is the dimensional freestream velocity. This modification compensates for the numerical dissipation of the turbulence variables from the freestream (inlet) boundary to the leading edge of the airfoil and provides the required turbulence intensity at the airfoil leading edge. Equation (2.11) is employed to initialize the freestream turbulence kinetic energy, k_∞ and dissipation, ω_∞ for the entire computational domain.

- **Modification of the $F_{\textbf{onset}}$**

  The last observation was that at higher angles of attack, the accuracy of the prediction of the transition point decreased. The primary correlation function that predicts the location of the transition point as stated in equation (2.8) is the F_{onset1} function which is a ratio of the vorticity to the momentum-thickness Reynolds number and a constant 2.193, where the magnitude of the constant is based on achieving a value of unity for F_{onset} within a Blasius boundary layer. However, as noted by Langtry et al. [32] the relationship between the vorticity and momentum-thickness Reynolds number is a function of the pressure gradient. A study [32] of the relative error between the maximum value of the vorticity Reynolds number and the momentum-thickness Reynolds number as a function of the boundary layer shape factor, reveals that for moderate shape factors of $(2.3 < H < 2.9)$, the error is less than 10%, however the error grows rapidly for higher shape factor values. Langtry and Menter [32] offered a modification of the intermittency factor for predicting separation-induced transition as shown in equation (2.10), where the constant that controls the relationship between Re_v and Re_{θ_c} is increased to 3.235. However, at higher angles of attack, the adverse pressure gradient grows and hence the correlation function, F_{onset}, needs to be rescaled. Results shown later in this work, will demonstrate repeatedly that at higher than 5 degrees angle of attack and/or higher Reynolds numbers the model underpredicts the transition point. Introducing new functions that modify the equations due to changes in the freestream conditions would be impractical and diminish the prime motivation of the approach where transition is predicted based on local quantities instead of global parameters or integrated values. In this work, we investigated the role of the correlation function for the onset of transition and propose a modified $F_{\text{onset1}} = \frac{Re_v}{3.29 Re_{\theta c}}$ correlation function and validated the model for two airfoils at various Reynolds numbers and angles of attack.

CHAPTER 3
Numerical Optimization Algorithms

Aerodynamic shape optimization and design based on CFD and flow control (transition prediction) approaches can be treated as optimization problems constrained by systems of partial differential equations [44]. Two types of numerical optimization techniques have been used to solve aerodynamic shape design problems: gradient-based methods such as steepest decent and sequential quadratic programming, etc., and non-gradient-based such as genetic algorithms, nonlinear simplex, stochastic, etc.

Non-gradient based approaches offer the possibility of locating the global optimum; however, the need for a large number of function evaluations render this approach intractable for aerodynamic design optimization based on solutions of the Navier-Stokes equation. Its ability to explore a large design space, entitles it to be employed together with low-fidelity equations such as potential flow to survey a large range of planform variables to investigate various aircraft configurations within the conceptual design stage.

In this work, the goal is to design natural laminar flow airfoils using the RANS equation together with transition-turbulence models. The computational cost of the fluid solver at a single flight condition requires approximately one wall clock hour and hence a non-gradient based approach would be infeasible. Therefore, a gradient-based approach using a smoothed steepest descent algorithm will be employed and presented in the following sub-sections.

3.1 Gradient-based Optimization Algorithms

In the following subsections the original steepest descent and smoothed steepest descent methods are discussed.

3.1.1 Steepest Descent

In each design cycle a step length, α, and search direction, $\vec{p}$, are employed in order to update the design variable, $\vec{x}$,

$$\vec{x}^{n+1} = \vec{x}^{n} + \alpha\vec{p}. \tag{3.1}$$

For the step length, α, a small constant value which satisfies the Wolf's conditions or a line search method can be used [44]. In order to find the search direction, $\vec{p}$, the optimization problem is defined as follows

$$\min f(\vec{x}) \quad \text{w.r.t} \quad \vec{x} \in \mathbb{R}^{m},$$

where $f(\vec{x})$ is a continuous function of the design variable vector, $\vec{x}$ that has m components. Considering equation (3.1), Taylor's expansion of the function $f(\vec{x})$ is written around the design variable, $\vec{x}$, as follows

$$f(\vec{x} + \alpha\vec{p}) = f(\vec{x}) + \alpha\vec{p}^{T}\nabla f(\vec{x}) + \frac{1}{2}\alpha^{2}\vec{p}^{T}\nabla^{2} f(\vec{x})\vec{p} + ..., \tag{3.2}$$

where $\nabla f(\vec{x})$ and $\nabla^2 f(\vec{x})$ are the gradient vector and Hessian matrix respectively. The second term in equation (3.2), $\alpha\vec{p}^T\nabla f(\vec{x})$, expresses the change of the function $f(\vec{x})$ along the search direction $\vec{p}$. By minimizing this term, the function $f(\vec{x})$ is minimized as well. Hence the optimization problem is stated as follows

$$\begin{aligned}&\min\ \vec{p}^T\nabla f(\vec{x}) \text{ w.r.t. } \vec{x}\in\mathbb{R}^m\\ &\text{subject to } ||\vec{p}|| = 1.\end{aligned}$$

By using the definition of the dot product between two vectors and the fact that $||\vec{p}|| = 1$, this term is described as

$$\vec{p}^T\nabla f(\vec{x}) = ||\vec{\nabla} f||\cos\theta,$$

where θ is the angle between the $\vec{p}$ and $\vec{\nabla} f$. In order to minimize the above equation, $\cos\theta$ must equal to -1. As a result the search direction, $\vec{p}$, is counter parallel to the gradient vector of the objective function and is defined as

$$\vec{p} = -\frac{\vec{\nabla} f}{||\vec{\nabla} f||}.$$

By considering the norm of the gradient vector as a factor for the step length, α, the search direction, $\vec{p}$, can be defined as the negative of the gradient vector

$$\vec{p} = -\vec{\nabla} f,$$

and the design variable for the next design cycle is defined as

$$\vec{x}^{n+1} = \vec{x}^{n} - \alpha \vec{\nabla} f.$$

By choosing the negative gradient vector as the design search direction, the steepest descent method assures the minimization of the cost function.

3.1.2 Smoothed Steepest Descent Method

In this modified version of the steepest descent method, the obtained gradient in each design iteration is smoothed. Using the smoothed gradient of the cost function accelerates the convergence of the optimization process. The smoothed gradient allows the use of larger step lengths which reduces the number of design iterations and accelerates the design and optimization process. Also the smoothed gradient of the cost function guarantees the smoothness of the design variables in each design iteration [44]. This property is valuable for aerodynamic shape optimization since the design variables which are the surface grid points, remain smooth during the optimization process. The non-smooth gradient of the cost function, $\vec{\nabla} f$, which was previously used to update the design variable vector, $\vec{x}$,

$$\vec{x}^{n+1} = \vec{x}^{n} + \vec{\delta} x = \vec{x}^{n} - \alpha \vec{\nabla} f,$$

is replaced by the smoothed gradient, $\vec{\overline{\nabla f}}$, through the following equation

$$\vec{\overline{\nabla f}} - \epsilon \frac{\partial^2}{\partial \xi^2} \vec{\overline{\nabla f}} = \vec{\nabla} f.$$

Using a large smoothing parameter, ϵ, allows a faster convergence of the optimizer since a larger step length can be employed [44]; however, too large a value would alter the search direction considerably and convergence of the optimization problem is no longer guaranteed. To show the effect of using the smoothed gradient on the optimization process, the first-order variation of the cost function is computed as follows

$$
\begin{aligned}
\delta f &= -\int\int \vec{\nabla} f \alpha \overline{\vec{\nabla} f} d\xi \\
&= -\alpha \int\int \left(\overline{\vec{\nabla} f} - \epsilon \frac{\partial^2}{\partial \xi^2} \right) \overline{\vec{\nabla} f} d\xi \\
&= -\alpha \int\int \overline{\vec{\nabla} f}^2 d\xi + \alpha \int\int \left(\epsilon \frac{\partial^2}{\partial \xi^2} \overline{\vec{\nabla} f} \right) \overline{\vec{\nabla} f} d\xi.
\end{aligned}
$$

Integration by parts leads to

$$
\delta f = -\alpha \int\int \left(\overline{\vec{\nabla} f}^2 + \epsilon \left(\frac{\partial \overline{\vec{\nabla} f}}{\partial \xi} \right)^2 \right) d\xi \leq 0.
$$

The obtained result is valid if both α and ϵ are positive.

3.2 Constrained Optimization

In this section the minimization of a function subject to constraints is discussed. The quadratic penalty method which is employed in the present work, formulates the constrained optimization problem as an unconstrained problem by defining a new objective function that augments the original objective function with a quadratic penalty function that contains the constraints. The constrained optimization is defined as,

$$\begin{aligned}
&\min f(x) \ \ \text{w.r.t.} \quad x \in \mathbb{R}^m, \\
&\text{subject to} \quad C_j = 0, \qquad j = 1, \dots, n,
\end{aligned}$$

where C_j are equality constraints, and n is the number of constraints [22]. A new objective function is defined by an additional term for each constraint. The additional term has the property that it is positive when the current iteration for the design variable vector, $\vec{x}$, violates the constraint and zero otherwise. The new objective function based on the quadratic penalty functions and the original cost function is defined as follows

$$Q(\vec{x}\ ;\ \mu_j) = f(\vec{x}) + \frac{1}{2}\sum_{j}^{m} \mu_j \ C(\vec{x})_j^{\ 2},$$

where μ_j are the penalty parameters and perform as a positive weight on the constraints, C_j. As the weight on the constraint increases, the constraint value approaches zero and the augmented objective function approaches the true objective. The new unconstrained optimization problem is described as

$$\min Q(\vec{x}\ ;\ \mu_j) \ \ \text{w.r.t.} \quad x \in \mathbb{R}^m \quad \text{where} \quad j = 1, \dots, n.$$

Since the new objective function, $Q(\vec{x}\ ;\ \mu_j)$, is a linear combination of $f(\vec{x})$ and C_js, therefore it remains smooth and differentiable. Thus all the algorithms suitable for unconstrained optimization can be employed for the optimization of $Q(\vec{x}\ ;\ \mu_j)$. In the present work the smoothed steepest algorthim (section 3.1.2) is used with the quadratic penalty function method.

3.3 Design Variables

The design variables are one of the crucial choices for a successful optimization and design procedure. In the present work, the surface grid points defining the airfoil shape are chosen to be the design variables. In the discrete computational domain the airfoil shape translates to mesh points. There are several other ways to change the airfoil shape such as Hicks-Henne bump functions [16] and the B-spline curves [34].

3.3.1 Mesh Points

Jameson [24, 25] proposed the concept of using mesh points for aerodynamic shape optimization. This point-wise method increases the number of design variables and if the finite difference method is used to compute the gradient, the computation would be intractable. Since, in the present work the discrete adjoint approach which does not need any flow re-evaluation is employed, it is feasible to use mesh points as design variables. However to avoid a discontinuous airfoil surface, the smoothed steepest descent method (subsection 3.1.2) is used.

CHAPTER 4

Discrete Adjoint Approach for the $\gamma - \tilde{Re}_{\theta t}$ Transition and the $k - \omega$ SST Turbulence Models

In this chapter the discrete adjoint equations for the discrete form of the governing equations, the $k - \omega$ SST, and $\gamma - \tilde{Re}_{\theta t}$ transition models are presented. Next the chapter list the various objective functions employed in this work, as well as their corresponding discrete adjoint boundary conditions. Lastly, the gradient of the cost function and the employed mesh perturbation technique are discussed.

4.1 Introduction

Consider an objective function, $I = I(\vec{w}, \vec{x}_s)$, to be minimized, where $\vec{w}$ is the flow variable vector, and $\vec{x}_s$ are the surface mesh points that define the airfoil surface. Since the residual of the flow solver, which is a function of the flow variables, $\vec{w}$, and surface points, $\vec{x}_s$, is assumed to be zero,

$$\vec{R}(\vec{w}, \vec{x}_s) = 0,$$

the gradient of the objective function, $I(\vec{w}, \vec{x}_s)$, with respect to the surface points, $\vec{x}_s$, is obtained by defining the Lagrangian function

$$L(\vec{w}, \vec{x}_s, \vec{\psi}) = I(\vec{w}, \vec{x}_s) + \vec{\psi}^T \vec{R}(\vec{w}, \vec{x}_s),$$

where the governing equation is introduced as a constraint and $\vec{\psi}$ is the Lagrange multiplier or adjoint vector. The sensitivity of the Lagrangian function with respect to the design variable vector, where in this work the surface mesh points are designated as the design variables, can be expanded as,

$$\frac{dL}{d\vec{x}_s} = \frac{\partial I}{\partial \vec{x}_s} + \frac{\partial I}{\partial \vec{w}}\frac{\partial \vec{w}}{\partial \vec{x}_s} + \vec{\psi}^T \left[\frac{\partial \vec{R}}{\partial \vec{w}}\frac{\partial \vec{w}}{\partial \vec{x}_s} + \frac{\partial \vec{R}}{\partial \vec{x}_v}\frac{\partial \vec{x}_v}{\partial \vec{x}_s} \right],$$

where $\vec{x}_v = \vec{x}_v(\vec{x}_s)$, the volume mesh points is a function of the surface mesh points, $\vec{x}_s$. To eliminate the flow variable sensitivities, we may rewrite the expression as

$$\frac{dL}{d\vec{x}_s} = \left[\frac{\partial I}{\partial \vec{w}} + \vec{\psi}^T \frac{\partial \vec{R}}{\partial \vec{w}} \right] \frac{\partial \vec{w}}{\partial \vec{x}_s} + \left[\frac{\partial I}{\partial \vec{x}_s} + \vec{\psi}^T \frac{\partial \vec{R}}{\partial \vec{x}_v}\frac{\partial \vec{x}_v}{\partial \vec{x}_s} \right], \tag{4.1}$$

and choose $\vec{\psi}^T$ such that the left term of equation (4.1) is zero, then the adjoint equation [22, 23, 25, 26] is defined as,

$$\frac{\partial I}{\partial \vec{w}} + \vec{\psi}^T \frac{\partial \vec{R}}{\partial \vec{w}} = 0, \tag{4.2}$$

where $\frac{\partial \vec{R}}{\partial \vec{w}}$ is the Jacobian of the governing equations with respect to the flow variables.

4.2 Formulation of the Discrete Adjoint Equations for the Turbulence and Transition Models

In steady state the primitive form of the $k-\omega$ SST turbulence model are written as,

$$\begin{aligned}
&\mu_t\left(\frac{\partial u_i}{\partial x_j}\right)^2-\beta^*\rho\omega k+\frac{\partial}{\partial x_i}\left[(\mu+\sigma_{k1}\mu_t)\frac{\partial k}{\partial x_i}\right]+\beta^*\rho\omega_{\text{amb}}k_{\text{amb}}-\rho u_i\frac{\partial k}{\partial x_i}=0,\\
&\frac{\gamma}{\nu_t}\mu_t\left(\frac{\partial u_i}{\partial x_j}\right)^2-\beta_1\rho\omega^2+\frac{\partial}{\partial x_i}\left[(\mu+\sigma_{\omega 1}\mu_t)\frac{\partial \omega}{\partial x_i}\right]+\beta_1\rho\omega_{\text{amb}}^2-\rho u_i\frac{\partial \omega}{\partial x_i}\\
&\qquad+2\left(1-F_1\right)\frac{\rho\sigma_{\omega 2}}{\omega}\frac{\partial k}{\partial x_i}\frac{\partial \omega}{\partial x_i}=0,
\end{aligned}\tag{4.3}$$

and the primitive equations of the $\gamma-\tilde{Re}_{\theta t}$ transition model are as follows,

$$\begin{aligned}
&F_{\text{lenght}}c_{a1}\rho S[\gamma F_{\text{onset}}]^{0.5}(1-c_{e1}\gamma)-c_{a2}\rho\Omega\gamma F_{\text{turb}}(c_{e2}\gamma-1)+\frac{\partial}{\partial x_j}\left[\left(\mu+\frac{\mu_t}{\sigma_f}\right)\frac{\partial\gamma}{\partial x_j}\right]\\
&\qquad-\rho u_i\frac{\partial\gamma}{\partial x_i}=0,\\
&c_{\theta t}\frac{(\rho U)^2}{500\mu}(Re_{\theta t}-\tilde{Re}_{\theta t})(1-F_{\theta t})+\frac{\partial}{\partial x_j}\left[\sigma_{\theta t}\left(\mu+\mu_t\right)\frac{\partial\gamma}{\partial x_j}\right]-\rho u_i\frac{\partial\tilde{Re}_{\theta t}}{\partial x_i}=0.
\end{aligned}\tag{4.4}$$

According to section 4.1, the linear adjoint operator (equation 4.2) can be written as,

$$A^T\cdot\vec{\psi}=\vec{C},\tag{4.5}$$

where A^T is the transpose of the Jacobian matrix of the flow residual, and $\vec{C}$ is the derivative of the cost function with respect to the flow variables. There are multitude of techniques in computing the exact Jacobian, spanning from reverse-mode automatic differentiation (AD) [22], the complex-step approach [22], and hand-derivation [22, 44]. In this work, we chose the hand-derivation, as opposed to AD as unoptimized AD has a tendency to be slower as well as the complex-step approach.

The primary disadvantage is the time-consuming nature of developing the discrete adjoint equations through a hand-derivation. By adding a pseudo time term, the adjoint equation (equation 4.5) is defined as,

$$\frac{\partial \vec{\psi}}{\partial t} + R(\vec{\psi}) = 0,$$

where $R(\vec{\psi}) = A^T\vec{\psi} - \vec{C}$ is the residual of the adjoint equation. The derivation procedure of the residual of the discrete adjoint equations for the $\gamma - \tilde{Re}_{\theta t}$ transition model and $k-\omega$ SST turbulence model for the ADI scheme is described in Appendix A. Hence the discrete adjoint equations for the transition and turbulence models for each control volume (i, j) can be written as follows,

$$\begin{aligned} \frac{\partial \psi_{m,ij}}{\partial t} &= J^D_{m,i+1j}\psi_{m,i+1j} + J^D_{m,i-1j}\psi_{m,i-1j} \\ &\quad + J^D_{m,ij}\psi_{m,ij} + J^D_{m,ij+1}\psi_{m,ij+1} + J^D_{m,ij-1}\psi_{m,ij-1}, \qquad m = 5, \dots, 8. \end{aligned} \tag{4.6}$$

where J^D shows the entries of the pentadiagonal matrix of the ADI scheme for the domain cells. Due to the usage of $m = 1, \dots, 4$ for the adjoint variables of the Navier-Stokes equations, $m = 5, 6$ are employed for the adjoint variables of the turbulence model and $m = 7, 8$ are for the transitional adjoint variables. To simplify the notation for the subscripts and avoid a secondary subscript, we have chosen to eliminate the comma between indices i, and j in the subscript. For an example, $ij - 1$, denotes $i, j - 1$. The entries of the pentadiagonal matrix for the adjoint equation of the turbulent kinetic energy, k, are defined as,

$$\begin{aligned}
J^D_{5,i-1j} &= \left[-\rho_{i-1j}\frac{u^-_{i-1}}{\Delta x_{i-1}} + \frac{1}{\Delta x_{i-1}}\left(\frac{\mu+\sigma_{k1}\mu_t}{\Delta x}\right)_{i-\frac{1}{2}} + 2\left(1-F_{1,i-1j}\right)\frac{\rho_{i-1j}\sigma_{\omega 2}}{\omega_{i-1j}}\frac{\omega_{ij}-\omega_{i-2j}}{\left(2\Delta x_{i-1}\right)^2}\right],\\
J^D_{5,ij-1} &= \left[-\rho_{ij-1}\frac{u^-_{j-1}}{\Delta x_{j-1}} + \frac{1}{\Delta x_{j-1}}\left(\frac{\mu+\sigma_{k1}\mu_t}{\Delta x}\right)_{j-\frac{1}{2}} + 2\left(1-F_{1,ij-1}\right)\frac{\rho_{ij-1}\sigma_{\omega 2}}{\omega_{ij-1}}\frac{\omega_{ij}-\omega_{ij-2}}{\left(2\Delta x_{j-1}\right)^2}\right],\\
J^D_{5,ij} &= \Bigg\{2\beta^*\rho_{ij}\omega_{ij} - \rho_{ij}\left(\frac{u^+_i-u^-_i}{\Delta x_i} + \frac{u^+_j-u^-_j}{\Delta x_j}\right) - \frac{1}{\Delta x_i}\left[\left(\frac{\mu+\sigma_{k1}\mu_t}{\Delta x}\right)_{i+\frac{1}{2}} + \left(\frac{\mu+\sigma_{k1}\mu_t}{\Delta x}\right)_{i-\frac{1}{2}}\right]\\
&\quad -\frac{1}{\Delta x_j}\left[\left(\frac{\mu+\sigma_{k1}\mu_t}{\Delta x}\right)_{j+\frac{1}{2}} + \left(\frac{\mu+\sigma_{k1}\mu_t}{\Delta x}\right)_{j-\frac{1}{2}}\right]\Bigg\},\\
J^D_{5,i+1j} &= \left[\rho_{i+1j}\frac{u^+_{i+1}}{\Delta x_{i+1}} + \frac{1}{\Delta x_{i+1}}\left(\frac{\mu+\sigma_{k1}\mu_t}{\Delta x}\right)_{i+\frac{1}{2}} - 2\left(1-F_{1,i+1j}\right)\frac{\rho_{i+1j}\sigma_{\omega 2}}{\omega_{i+1j}}\frac{\omega_{i+2j}-\omega_{ij}}{\left(2\Delta x_{i+1}\right)^2}\right],\\
J^D_{5,ij+1} &= \left[\rho_{ij+1}\frac{u^+_{j+1}}{\Delta x_{j+1}} + \frac{1}{\Delta x_{j+1}}\left(\frac{\mu+\sigma_{k1}\mu_t}{\Delta x}\right)_{j+\frac{1}{2}} - 2\left(1-F_{1,ij+1}\right)\frac{\rho_{ij+1}\sigma_{\omega 2}}{\omega_{ij+1}}\frac{\omega_{ij+2}-\omega_{ij}}{\left(2\Delta x_{j+1}\right)^2}\right].
\end{aligned}$$

The entries of the pentadiagonal matrix for the adjoint equation of the specific dissipation, ω, are defined as,

$$
\begin{aligned}
J^D_{6,i-1j} &= \left[-\rho_{i-1j}\frac{u^-_{i-1}}{\Delta x_{i-1}} + \frac{1}{\Delta x_{i-1}}\left(\frac{\mu+\sigma_{\omega 1}\mu_t}{\Delta x}\right)_{i-\frac{1}{2}} + 2\left(1-F_{1,i-1j}\right)\frac{\rho_{i-1j}\sigma_{\omega 2}}{\omega_{i-1j}}\frac{k_{ij}-k_{i-2j}}{\left(2\Delta x_{i-1}\right)^2}\right], \\
J^D_{6,ij-1} &= \left[-\rho_{ij-1}\frac{u^-_{j-1}}{\Delta x_{j-1}} + \frac{1}{\Delta x_{j-1}}\left(\frac{\mu+\sigma_{\omega 1}\mu_t}{\Delta x}\right)_{j-\frac{1}{2}} + 2\left(1-F_{1,ij-1}\right)\frac{\rho_{ij-1}\sigma_{\omega 2}}{\omega_{ij-1}}\frac{k_{ij}-k_{ij-2}}{\left(2\Delta x_{j-1}\right)^2}\right], \\
J^D_{6,ij} &= \Bigg\{2\beta^*\rho_{ij}k_{ij} + 4\beta\rho_{ij}\omega_{ij} - \rho_{ij}\left(\frac{u^+_i-u^-_i}{\Delta x_i} + \frac{u^+_j-u^-_j}{\Delta x_j}\right) \\
&\quad -\frac{1}{\Delta x_i}\left[\left(\frac{\mu+\sigma_{\omega 1}\mu_t}{\Delta x}\right)_{i+\frac{1}{2}} + \left(\frac{\mu+\sigma_{\omega 1}\mu_t}{\Delta x}\right)_{i-\frac{1}{2}}\right] - \frac{1}{\Delta x_j}\left[\left(\frac{\mu+\sigma_{\omega 1}\mu_t}{\Delta x}\right)_{j+\frac{1}{2}} + \left(\frac{\mu+\sigma_{\omega 1}\mu_t}{\Delta x_{j-\frac{1}{2}}}\right)_{j-\frac{1}{2}}\right] \\
&\quad -\left(1-F_{1,ij}\right)\frac{\rho_{ij}\sigma_{\omega 2}}{\omega^2_{ij}}\left[\frac{k_{i+1j}-k_{i-1j}}{\Delta x_i}\frac{\omega_{i+1j}-\omega_{i-1j}}{\Delta x_i} + \frac{k_{ij+1}-k_{ij-1}}{\Delta x_j}\frac{\omega_{ij+1}-\omega_{ij-1}}{\Delta x_j}\right]\Bigg\}, \\
J^D_{6,i+1j} &= \left[\rho_{i+1j}\frac{u^+_{i+1}}{\Delta x_{i+1}} + \frac{1}{\Delta x_{i+1}}\left(\frac{\mu+\sigma_{\omega 1}\mu_t}{\Delta x}\right)_{i+\frac{1}{2}} - 2\left(1-F_{1,i+1j}\right)\frac{\rho_{i+1j}\sigma_{\omega 2}}{\omega_{i+1j}}\frac{k_{i+2j}-k_{ij}}{\left(2\Delta x_{i+1}\right)^2}\right], \\
J^D_{6,ij+1} &= \left[\rho_{ij+1}\frac{u^+_{j+1}}{\Delta x_{j+1}} + \frac{1}{\Delta x_{j+1}}\left(\frac{\mu+\sigma_{\omega 1}\mu_t}{\Delta x}\right)_{j+\frac{1}{2}} - 2\left(1-F_{1,ij+1}\right)\frac{\rho_{ij+1}\sigma_{\omega 2}}{\omega_{ij+1}}\frac{k_{ij+2}-k_{ij}}{\left(2\Delta x_{j+1}\right)^2}\right].
\end{aligned}
$$

The entries of the pentadiagonal matrix for the adjoint equation of the intermittency factor, γ, are defined as,

$$J^D_{7,i-1j} = \left[-\rho_{i-1j} \frac{u^-_{i-1}}{\Delta x_{i-1}} + \frac{1}{\Delta x_{i-1}} \left(\frac{\mu + \frac{\mu_t}{\sigma_f}}{\Delta x} \right)_{i-\frac{1}{2}} \right],$$

$$J^D_{7,ij-1} = \left[-\rho_{ij-1} \frac{u^-_{j-1}}{\Delta x_{j-1}} + \frac{1}{\Delta x_{j-1}} \left(\frac{\mu + \frac{\mu_t}{\sigma_f}}{\Delta x} \right)_{j-\frac{1}{2}} \right],$$

$$\begin{aligned} J^D_{7,ij} = \Bigg\{ & F_{lenght} c_{a1} \rho S F^{0.5}_{onset} \left(\frac{1}{\sqrt{\gamma}} - c_{e1} \sqrt{\gamma} \right) - c_{a2} \rho \Omega F_{turb} \left(2 c_{e2} \gamma - 1 \right) \\ & -\rho_{ij} \left(\frac{u^+_i - u^-_i}{\Delta x_i} + \frac{u^+_j - u^-_j}{\Delta x_j} \right) - \frac{1}{\Delta x_i} \left[\left(\frac{\mu + \frac{\mu_t}{\sigma_f}}{\Delta x} \right)_{i+\frac{1}{2}} + \left(\frac{\mu + \frac{\mu_t}{\sigma_f}}{\Delta x} \right)_{i-\frac{1}{2}} \right] \\ & - \frac{1}{\Delta x_j} \left[\left(\frac{\mu + \frac{\mu_t}{\sigma_f}}{\Delta x} \right)_{j+\frac{1}{2}} + \left(\frac{\mu + \frac{\mu_t}{\sigma_f}}{\Delta x} \right)_{j-\frac{1}{2}} \right] \Bigg\}, \end{aligned}$$

$$J^D_{7,i+1j} = \left[\rho_{i+1j} \frac{u^+_{i+1}}{\Delta x_{i+1}} + \frac{1}{\Delta x_{i+1}} \left(\frac{\mu + \frac{\mu_t}{\sigma_f}}{\Delta x} \right)_{i+\frac{1}{2}} \right],$$

$$J^D_{7,ij+1} = \left[\rho_{ij+1} \frac{u^+_{j+1}}{\Delta x_{j+1}} + \frac{1}{\Delta x_{j+1}} \left(\frac{\mu + \frac{\mu_t}{\sigma_f}}{\Delta x} \right)_{j+\frac{1}{2}} \right].$$

While the entries of the pentadiagonal matrix for the adjoint equation of the momentum-thickness Reynolds number can be defined as,

$$\begin{aligned}
J^D_{8,i-1j} &= \left[-\rho_{i-1j}\frac{u^-_{i-1}}{\Delta x_{i-1}} + \frac{1}{\Delta x_{i-1}}\left(\frac{\sigma_{\theta t}\left(\mu+\mu_t\right)}{\Delta x}\right)_{i-\frac{1}{2}}\right], \\
J^D_{8,ij-1} &= \left[-\rho_{ij-1}\frac{u^-_{j-1}}{\Delta x_{j-1}} + \frac{1}{\Delta x_{j-1}}\left(\frac{\sigma_{\theta t}\left(\mu+\mu_t\right)}{\Delta x}\right)_{j-\frac{1}{2}}\right], \\
J^D_{8,ij} &= \left\{-\rho_{ij}\left(\frac{u^+_i-u^-_i}{\Delta x_i}+\frac{u^+_j-u^-_j}{\Delta x_j}\right) - \frac{1}{\Delta x_i}\left[\left(\frac{\sigma_{\theta t}\left(\mu+\mu_t\right)}{\Delta x}\right)_{i+\frac{1}{2}} + \left(\frac{\sigma_{\theta t}\left(\mu+\mu_t\right)}{\Delta x}\right)_{i-\frac{1}{2}}\right]\right. \\
&\quad \left. -\frac{1}{\Delta x_j}\left[\left(\frac{\sigma_{\theta t}\left(\mu+\mu_t\right)}{\Delta x}\right)_{j+\frac{1}{2}} + \left(\frac{\sigma_{\theta t}\left(\mu+\mu_t\right)}{\Delta x_{j-\frac{1}{2}}}\right)_{j-\frac{1}{2}}\right] - c_{\theta t}\frac{(\rho U)^2}{500\mu}(1-F_{\theta t})\right\}, \\
J^D_{8,i+1j} &= \left[\rho_{i+1j}\frac{u^+_{i+1}}{\Delta x_{i+1}} + \frac{1}{\Delta x_{i+1}}\left(\frac{\sigma_{\theta t}\left(\mu+\mu_t\right)}{\Delta x}\right)_{i+\frac{1}{2}}\right], \\
J^D_{8,ij+1} &= \left[\rho_{ij+1}\frac{u^+_{j+1}}{\Delta x_{j+1}} + \frac{1}{\Delta x_{j+1}}\left(\frac{\sigma_{\theta t}\left(\mu+\mu_t\right)}{\Delta x}\right)_{j+\frac{1}{2}}\right].
\end{aligned}$$

The i- and j-directions are the tangential and orthogonal directions to the wall boundary respectively, while u^-_j and u^+_j are defined as

$$\begin{aligned}
u^-_j &= \frac{1}{2}\left(u_j - |u_j|\right), \\
u^+_j &= \frac{1}{2}\left(u_j + |u_j|\right).
\end{aligned} \tag{4.7}$$

Since in the present work the discrete adjoint equations for the Reynolds-averaged Navier-Stokes equations [44] are solved separately from the discrete adjoint equations for the transition and turbulence models through a loose-coupling approach, a series of coupling terms are derived and added to the equations as source terms. The following terms are added to the right-hand-side (RHS) of the adjoint equations for the Navier-Stokes equations

$$\begin{aligned}
\text{RHS}(\psi_2) &= \psi_5 \frac{\partial k}{\partial x} + \psi_6 \frac{\partial \omega}{\partial x} + \psi_7 \frac{\partial \gamma}{\partial x} + \psi_8 \frac{\partial \tilde{R}e_{\theta t}}{\partial x}, \\
\text{RHS}(\psi_3) &= \psi_5 \frac{\partial k}{\partial y} + \psi_6 \frac{\partial \omega}{\partial y} + \psi_7 \frac{\partial \gamma}{\partial y} + \psi_8 \frac{\partial \tilde{R}e_{\theta t}}{\partial y}.
\end{aligned}$$

The coupling terms which are added to the residual of the discrete adjoint equations for the $k - \omega$ SST turbulence and $\gamma - \tilde{R}e_{\theta t}$ transition models are as follows,

$$\begin{aligned}
\text{RHS}(\psi_5) &= \frac{\partial \mu}{\partial k} \left(\psi_2 \frac{\partial^2 U}{\partial x^2} + \psi_3 \frac{\partial^2 U}{\partial y^2} \right), \\
\text{RHS}(\psi_6) &= \frac{\partial \mu}{\partial \omega} \left(\psi_2 \frac{\partial^2 U}{\partial x^2} + \psi_3 \frac{\partial^2 U}{\partial y^2} \right), \\
\text{RHS}(\psi_7) &= \frac{\partial \mu}{\partial \gamma} \left(\psi_2 \frac{\partial^2 U}{\partial x^2} + \psi_3 \frac{\partial^2 U}{\partial y^2} \right), \\
\text{RHS}(\psi_8) &= \frac{\partial \mu}{\partial \tilde{R}e_{\theta t}} \left(\psi_2 \frac{\partial^2 U}{\partial x^2} + \psi_3 \frac{\partial^2 U}{\partial y^2} \right).
\end{aligned}$$

These terms couple the adjoint counterpart for the momentum equations of the Reynolds-averaged Navier-Stokes equations to the adjoint equations for the transition and turbulence models respectively.

4.2.1 Discrete adjoint boundary conditions

In contrast to the continuous adjoint approach where the boundary conditions are separate equations, the discrete adjoint boundary conditions appear as source terms in the equations of the interior cells adjacent to the wall and far-field boundaries.

- Inlet boundary

The inlet Dirichlet boundary conditions [32, 37] for the turbulence and transition models are defined as

$$k_\infty = 10^{-6}U_\infty^2, \qquad \omega_\infty = \frac{\rho_\infty k_\infty}{10\mu_\infty},$$
$$\gamma_\infty = 1.0, \qquad \tilde{R}e_{\theta t\infty} = 1173.5 - 589.428Tu_\infty + \frac{0.2196}{Tu_\infty^2}.$$

By introducing the inlet boundary conditions into the mathematical derivation of the discrete adjoint equations, the entries of the pentadiagonal matrix for the boundary cell, ψ_{ij}, are altered as follows

$$J^B_{5,ij} = J^D_{5,ij} + \rho_{ij}\frac{u_j^-}{\Delta x_j} - \frac{1}{\Delta x_j}\left(\frac{\mu + \sigma_{k1}\mu_t}{\Delta x_{j-\frac{1}{2}}}\right)_{j-\frac{1}{2}},$$
$$J^B_{6,ij} = J^D_{6,ij} + \rho_{ij}\frac{u_j^-}{\Delta x_j} - \frac{1}{\Delta x_j}\left(\frac{\mu + \sigma_{\omega 1}\mu_t}{\Delta x_{j-\frac{1}{2}}}\right)_{j-\frac{1}{2}},$$
$$J^B_{7,ij} = J^D_{7,ij} + \rho_{ij}\frac{u_j^-}{\Delta x_j} - \frac{1}{\Delta x_j}\left(\frac{\mu + \frac{\mu_t}{\sigma_f}}{\Delta x_{j-\frac{1}{2}}}\right)_{j-\frac{1}{2}},$$
$$J^B_{8,ij} = J^D_{8,ij} + \rho_{ij}\frac{u_j^-}{\Delta x_j} - \frac{1}{\Delta x_j}\left(\frac{\sigma_{\theta t}\left(\mu + \mu_t\right)}{\Delta x_{j-\frac{1}{2}}}\right)_{j-\frac{1}{2}}, \qquad i \in \Omega, j \in \delta\Omega_{\text{inlet}},$$

where J^B are the entries of the pentadiagonal matrix for the boundary cell.

- Outlet boundary

  At the outlet, the turbulence and transition models employ Neumann boundary conditions [32, 37]. Here the normal gradients of the variables at the outlet boundary are zero as follows

$$\frac{\partial k}{\partial \eta}_{outlet} = \frac{\partial \omega}{\partial \eta}_{outlet} = \frac{\partial \gamma}{\partial \eta}_{outlet} = \frac{\partial \tilde{R}e_{\theta t}}{\partial \eta}_{outlet} = 0.$$

By applying the outlet boundary conditions of the turbulence and transition models into the discrete adjoint approach, the entries of the pentadiagonal matrix for the outlet boundary cell (i, j) can be represented as

$$\begin{aligned}
J^B_{5,ij} &= J^D_{5,ij} - \rho_{ij}\frac{u_i^-}{\Delta x_i} + \frac{1}{\Delta x_i}\left(\frac{\mu + \sigma_{k1}\mu_t}{\Delta x_{i+\frac{1}{2}}}\right)_{i+\frac{1}{2}}, \\
J^B_{6,ij} &= J^D_{6,ij} - \rho_{ij}\frac{u_i^-}{\Delta x_i} + \frac{1}{\Delta x_i}\left(\frac{\mu + \sigma_{\omega 1}\mu_t}{\Delta x_{i+\frac{1}{2}}}\right)_{i+\frac{1}{2}}, \\
J^B_{7,ij} &= J^D_{7,ij} - \rho_{ij}\frac{u_i^-}{\Delta x_i} + \frac{1}{\Delta x_i}\left(\frac{\mu + \frac{\mu_t}{\sigma_f}}{\Delta x_{i+\frac{1}{2}}}\right)_{i+\frac{1}{2}}, \\
J^B_{8,ij} &= J^D_{8,ij} - \rho_{ij}\frac{u_i^-}{\Delta x_i} + \frac{1}{\Delta x_i}\left(\frac{\sigma_{\theta t}\left(\mu + \mu_t\right)}{\Delta x_{i+\frac{1}{2}}}\right)_{i+\frac{1}{2}}, \qquad i \in \delta\Omega_{\text{outlet}}, j \in \Omega.
\end{aligned}$$

- Wall boundary

At the wall boundary, the definition of the boundary conditions are dissimilar, where the transition model employs a Neumann boundary condition, while the turbulence model uses Dirichlet [32, 37]. The wall boundary conditions for the turbulence model are defined as follows,

$$k_{wall} = 0, \qquad \omega_{wall} = \frac{6\mu_\infty}{\beta\rho_\infty y^2}.$$

By employing the wall boundary conditions of the turbulence model into the discrete adjoint approach, the entries of the pentadiagonal matrix for the boundary cell (i, j) change and are defined as,

$$J^B_{5,ij} = J^D_{5,ij} - \rho_{ij} \frac{u^+_j}{\Delta x_j} - \frac{1}{\Delta x_j} \left(\frac{\mu + \sigma_{k1} \mu_t}{\Delta x_{j+\frac{1}{2}}} \right)_{j+\frac{1}{2}},$$

$$J^B_{6,ij} = J^D_{6,ij} - \rho_{ij} \frac{u^+_j}{\Delta x_j} - \frac{1}{\Delta x_j} \left(\frac{\mu + \sigma_{\omega 1} \mu_t}{\Delta x_{j+\frac{1}{2}}} \right)_{j+\frac{1}{2}}, \qquad i \in \delta\Omega_{\text{wall}}, j \in \delta\Omega_{\text{wall}}.$$

The transition model employs Neumann zero flux boundary conditions for both equations [32, 37],

$$\frac{\partial \gamma_{wall}}{\partial n} = 0, \qquad \frac{\partial \tilde{R}e_{\theta t,wall}}{\partial n} = 0.$$

The Neumann type wall boundary conditions of the transition model are introduced into the discrete adjoint approach, and the entries of the pentadiagonal matrix are altered as follows,

$$J^B_{7,ij} = J^D_{7,ij} + \rho_{ij} \frac{u^+_j}{\Delta x_j} + \frac{1}{\Delta x_j} \left(\frac{\mu + \frac{\mu_t}{\sigma_f}}{\Delta x_{j-\frac{1}{2}}} \right)_{j-\frac{1}{2}},$$

$$J^B_{8,ij} = J^D_{8,ij} + \rho_{ij} \frac{u^+_j}{\Delta x_j} + \frac{1}{\Delta x_j} \left(\frac{\sigma_{\theta t} \left(\mu + \mu_t\right)}{\Delta x_{j-\frac{1}{2}}} \right)_{j-\frac{1}{2}}, \qquad i \in \delta\Omega_{\text{wall}}, j \in \delta\Omega_{\text{wall}}.$$

The discrete derivatives of the cost function with respect to the field variables $\left(\frac{\partial I}{\partial k_{ij}}, \frac{\partial I}{\partial \omega_{ij}}, \frac{\partial I}{\partial \gamma_{ij}}, \frac{\partial I}{\partial \tilde{R}e_{\theta tij}} \right)$ should be added to the right-hand-side of the discrete adjoint equation of the domain, boundary cells or both as source terms [44, 22]. The discrete adjoint equations are derived by hand; however, some parts of the hand derivation of the transition and turbulence models have been verified through the MAPLE software. For the sake of completeness, the continuous adjoint approach is presented in Appendix B. The consistency of the adjoint approaches is shown in section B.2.2

by recovering the continuous adjoint equations from the discrete adjoint equations for the transition and turbulence models in the limit that the mesh width reduces to zero. The discrete adjoint equations for the $\gamma - \tilde{Re}_{\theta t}$ transition model and $k - \omega$ SST turbulence model form a four pentadiagonal PDE system. An alternating direction implicit (ADI) scheme similar to the turbulence and transition models is employed to solve the derived equations.

4.3 Cost Function

In this section the various cost functions employed to design NLF airfoils, are explained. For each cost function, the derivative of the function with respect to the state variable must be added to the right-hand-side of the corresponding costate discrete adjoint equation (4.6). The derivative of the cost functions associated with the state variables for the Navier-Stokes equations have been derived in reference [44]; therefore only the source terms of the discrete adjoint equations for the $k - \omega$ SST turbulence model and $\gamma - \tilde{Re}_{\theta t}$ transition model are described as follows:

- Drag Coefficient

  The drag coefficient is a boundary cost function which does not have any domain contribution and therefore its derivative is shown only as the source term of the discrete adjoint equations for the boundary cells. In the physical domain, the aerodynamic normal force coefficient is defined as follows,

$$C_n = \frac{1}{c}\left[\int_0^c \left(C_{p,l} - C_{p,u}\right) dx_1 + \int_{\mathrm{LE}}^{\mathrm{TE}} \left(C_{f,u} - C_{f,l}\right) dx_2\right], \qquad (4.8)$$

and the following equation describes the aerodynamic axial force coefficient as,

$$C_a = \frac{1}{c}\left[\int_{\mathrm{LE}}^{\mathrm{TE}} \left(C_{p,u} - C_{p,l}\right) dx_2 + \int_0^c \left(C_{f,u} - C_{f,l}\right) dx_1\right]. \tag{4.9}$$

In the above equations c is the airfoil chord length while LE and TE stand for the airfoil leading edge and trailing edge points. In addition C_p and C_f are the pressure and skin friction coefficients respectively. Finally the u and l indices are for the upper and lower airfoil surfaces. The drag coefficient which constitutes pressure and skin friction components, is defined as follows,

$$I_D = C_d = C_n \cos\alpha - C_a \sin\alpha,$$

where α is the angle of attack. The contributions of this function in the discrete adjoint equations for the Navier-Stokes equations are stated in reference [44] in detail. To derive the discrete adjoint boundary source terms, the drag is differentiated with respect to the transition and turbulence state variables. The derivative of the skin friction drag with respect to q can be defined as,

$$\frac{\partial C_d}{\partial q} = \frac{\partial C_d}{\partial \mu_t}\frac{\partial \mu_t}{\partial P_k}\frac{\partial P_k}{\partial q},$$

where q is any one of the transition or turbulence state variables, $(\gamma, \tilde{Re}_{\theta t}, k, \omega)$.

- Lift Coefficient

  To maintain or maximize the lift coefficient a quadratic penalty function is defined as below

$$I_L = \frac{1}{2}\left(C_l - C_{l_T}\right)^2,$$

where C_{l_T} is the target lift coefficient. For cases, where the lift is to be maintained, then the initial lift coefficient is employed, while a higher target value is utilized if lift maximization is sought. According to equations 4.8 and 4.9, the lift coefficient which has pressure and skin friction components, is defined as below,

$$C_l = C_n \sin\alpha + C_a \cos\alpha.$$

Similar to the drag coefficient, the contributions of the lift coefficient to the adjoint equations for the RANS solver are explained in reference [44]. The derivative of the skin friction component of the lift coefficient with respect to q can be expressed as,

$$\frac{\partial C_l}{\partial q} = \frac{\partial C_l}{\partial \mu_t} \frac{\partial \mu_t}{\partial P_k} \frac{\partial P_k}{\partial q},$$

where q again is any one of the transition and turbulence variables dependent to the corresponding adjoint equation. The lift coefficient only has contributions to the boundary cells.

- Production of Turbulent Kinetic Energy

  Reduction of the turbulent kinetic energy decreases the turbulence intensity or eddy viscosity over the entire domain. As the level of the turbulent viscosity is reduced the transition points are postponed and the viscous component of drag is minimized. More details about the idea and effectiveness of this cost function will be presented and discussed in section 6.2. The production of turbulent kinetic energy as a cost function is specifically applied to the adjoint variables of the transition and turbulence models. This function is defined as follows,

$$I_{P_k} = \sum P_k = \sum \gamma_{\text{eff}} \mu_t S^2 \qquad \text{in} \quad \Omega.$$

To add the effect of this cost function into the right hand side of the discrete adjoint equations for the transition and turbulence models, a chain rule equation is employed as follows,

$$\frac{\partial P_k}{\partial q} = \frac{\partial P_k}{\partial \mu_t} \frac{\partial \mu_t}{\partial q},$$

where q is representative of every transition and turbulence variable for the computational cell. Unlike the previous two cost functions that were integrals over the wall boundary, in this case, the production of the turbulent kinetic energy cost function would appear as source terms in the discrete adjoint equations for the $\gamma{-}\tilde{R}e_{\theta t}$ transition and $k{-}\omega$ SST turbulence models and are defined respectively as

$$\begin{aligned}
\text{RHS}(\psi_5)^{new} &= \text{RHS}(\psi_5)^{old} + \frac{\rho\gamma S^2}{\omega}, \\
\text{RHS}(\psi_6)^{new} &= \text{RHS}(\psi_6)^{old} - \frac{\rho\gamma k S^2}{\omega^2}, \\
\text{RHS}(\psi_7)^{new} &= \text{RHS}(\psi_7)^{old} + \mu_t S^2, \\
\text{RHS}(\psi_8)^{new} &= \text{RHS}(\psi_8)^{old}, \qquad\qquad \text{in} \quad \Omega.
\end{aligned}$$

The mentioned cost functions will be investigated for their effectiveness to design new natural laminar flow (NLF) airfoils by postponing the transition points and minimizing the pressure and skin friction drag components while maintaining or maximizing the lift coefficient.

4.4 Gradient of the Cost Function

As explained in section 4.1, the solution of the discrete adjoint equations removes the dependency of the gradient of the cost function to the flow variables and only the gradient is calculated with respect to the variation of the grid perturbation. After solving the discrete adjoint equations, the gradient of the cost function (equation 4.1) can be written as follows,

$$\frac{dL}{d\vec{x}_s} = \frac{\partial I}{\partial \vec{x}_s} + \vec{\psi}^T \frac{\partial \vec{R}}{\partial \vec{x}_v} \frac{\partial \vec{x}_v}{\partial \vec{x}_s},$$

where $\frac{\partial I}{\partial \vec{x}_s}$ is the variation of the cost function with respect to the perturbation of the surface mesh points. The $\frac{\partial \vec{R}}{\partial \vec{x}_v}$ is the variation of the residual associated to the variation of the volume grid points while $\frac{\partial \vec{x}_v}{\partial \vec{x}_s}$ is the mesh sensitivity. To compute the gradient each geometry surface point or design variable is perturbed and the corresponding residual is re-evaluated. For the residual re-evaluation the grid should be re-generated which is computationally very costly. To avoid the grid re-generation, Jameson et al. [24, 25] introduced the following method for the structured grids to modify the location of the grid points according to the perturbation of the airfoil surface. The arc length from a grid point of a grid index line to its corresponding perturbed geometry surface point is calculated. Then the ratio of the arc length is computed versus the distance of the perturbed surface point from the far-field. Based on the ratio the new location of the grid point is updated as follow

$$\begin{cases} x_{Ij}^{new} = x_{Ij}^{old} + C_j \left(x_{I1}^{new} - x_{I1}^{old} \right) \\ y_{Ij}^{new} = y_{Ij}^{old} + C_j \left(y_{I1}^{new} - y_{I1}^{old} \right) \end{cases} \qquad \text{for} \quad j = 1, 2, ..., j_{max},$$

where C_j is defined as

$$C_j = 1 - (3 - 2N_j)\, N_j^2 \quad \text{and} \quad N_j = \frac{\sum_l^j \sqrt{(x_{Il} - x_{Il-1})^2 + (y_{Il} - y_{Il-1})^2}}{\sum_l^{j_{max}} \sqrt{(x_{Il} - x_{Il-1})^2 + (y_{Il} - y_{Il-1})^2}}.$$

The mentioned algorithm relates the variation of the surface points or design variables to the variation of the grid point locations of the corresponding grid line. The grid perturbation scheme is very robust and its robustness has been specifically verified for two-dimensional viscous grids [29]. This simple method guarantees the smoothness of the modified grids without any grid point cross-overs. More details about this mesh modification algorithm can be found in reference [44].

CHAPTER 5
Flow Solver Results

In this chapter a thorough validation of the developed laminar-turbulent flow solver is performed against the NLF(1)-0416 airfoil [51] and S809 wind turbine profile [52] experimental data.

5.1 Introduction

The following two airfoils are chosen to validate the accuracy and the capability of the new transitional flow solver. The first test case is the NLF(1)-0416 airfoil which was initially designed for general aviation applications [51] but has been successfully used for wind turbine blades [49]. The second test case is the S809 airfoil which is specially designed for stall-regulated horizontal axis wind turbine blades [52]. Figures 5–1(a) and 5–1(b) illustrate the NLF(1)-0416 and S809 profiles using a 512×256 structured C-type grid. To provide a thorough examination of the new transitional solver, an extensive grid sensitivity study to investigate the role of the grid density in both the x-direction and y-direction of the grids on the accuracy of the skin friction coefficient, the length of the laminar separation bubble, and the location of the transition point, will be presented. Convergence of the flow solver as well as the transition and turbulence solvers will be examined. The numerical results will be compared to experimental and other numerical solutions [5, 32], when available, such as pressure coefficient distributions, transition points versus angles of attack, and drag polars at various Reynolds numbers. The Reynolds number and angle of attack effect on the

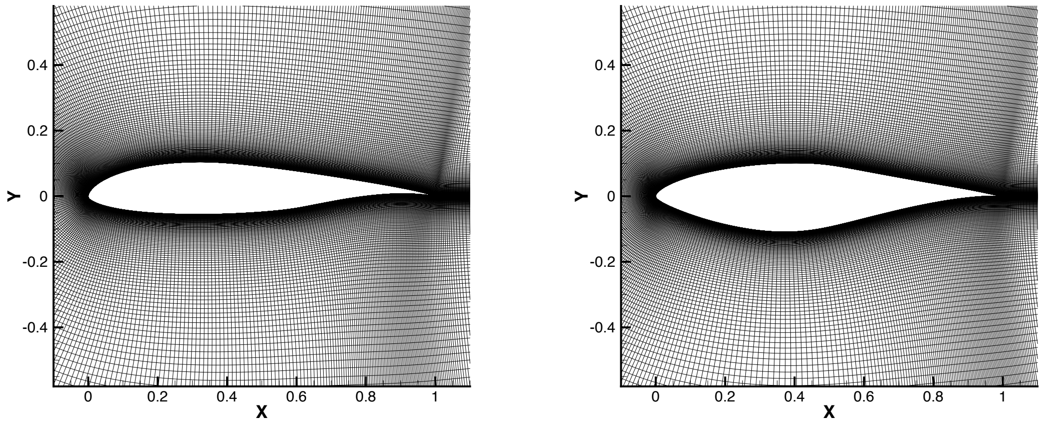

(a) NLF(1)-0416 (b) S809

Figure 5–1: 512 × 256 structured C-type grid

size and position of the laminar separation bubble, the transition point, as well as the proper modelling of the turbulent flow separation will be thoroughly analyzed and compared to observations by Somers [52].

5.2 Convergence

The S809 wind turbine airfoil at a Reynolds number of 2×10^6 and an angle of attack of 1 degree is considered for the convergence study of the flow, $k - \omega$ SST turbulence, and $\gamma - \tilde{Re}_{\theta t}$ transition models. The density residual of the flow solver reduces by five orders within 2000 multigrid cycles. This level of convergence is sufficient to achieve global convergence and ensure that the lift and drag coefficients have converged, which typically converged within 500 multigrid cycles, accurate up to four decimal places. The residual convergence of the $\gamma - \tilde{Re}_{\theta t}$ transition model and the $k - \omega$ SST turbulence model are described in figure 5–2. The turbulent kinetic energy, k, and specific dissipation, ω, achieve a ten order and machine zero convergence, respectively, within 1000 multigrid cycles. The turbulence intermittency factor, γ, is reduced by ten orders, while the momentum-thickness Reynolds number, $\tilde{Re_{\theta t}}$ attains a six order reduction within 1000 multigrid cycles. The turbulence intensity level, Tu_∞ is set to 0.2% based on the recommendation of Langtry and Menter [32], and the ratio of viscosities, $\left(\frac{\mu_t}{\mu}\right)_\infty$ is initialized to ten for all cases presented in this paper. The initial and farfield values at the upstream boundary for the turbulent kinetic energy, k, and specific dissipation, ω, are calculated via equation (2.11), while at the downstream outlet boundary, a zeroth order extrapolation is employed. In the case of the transition model, the turbulence intermittency factor, γ, is initialized to unity in the entire domain and fixed at the same value at the farfield inlet boundary. The momentum-thickness Reynolds number, $\tilde{Re_{\theta t}}$, is only a function of the turbulence intensity level and computed from equation (2.9). As mentioned in section 2.3, the three solvers are loosely coupled where the transition and turbulence models are updated at the fine grid level of every multigrid cycle.

5.3 Grid Study

The NLF(1)-0416 airfoil at a Reynolds number of 2×10^6 and an angle attack of 1 degree, is chosen to perform a grid study of the transition model. To study the effect of the grid density along the streamwise and normal to the wall directions, the grid study is first performed in the x-direction and secondly along the y-direction separately. The proper grid density in the stream wise direction is required to ensure an accurate simulation of the transitional model to precisely resolve the transition point, while the y^+ study is to ensure that the turbulent boundary layer is accurately simulated. In the x-direction the coarse grid is a 384×256 structured C-type mesh

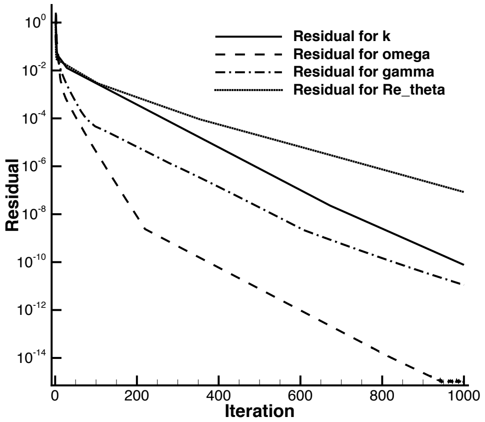

Figure 5–2: Convergence of the transition and turbulence models

where 256 nodes are on the airfoil surface. The wall spacing is 1×10^{-5} chords, and here the y^{+} is approximately 0.1 for all grids. The distance to the farfield boundary is at approximately 15 chord lengths from the leading edge of the airfoil. The medium and fine grids are generated by increasing the number of points on the airfoil surface by 128 points consecutively, while maintaining the wall distance and the number of grid points in the wake region. Figure 5–3 illustrates the effect of the grid density in the x-direction on the skin friction coefficient. Experimental results show a laminar separation bubble at approximately 40% on the upper surface [51]. As the grid size is increased, the skin friction distribution along the laminar region, remains unaffected; however, a laminar separation bubble at 40% is evident for the medium and fine grids and absent on the coarse grid. A comparison of the corresponding lift and drag coefficient values for each grid are presented in table 5–1. The values remain largely similar for the lift coefficient and identical for the drag coefficients

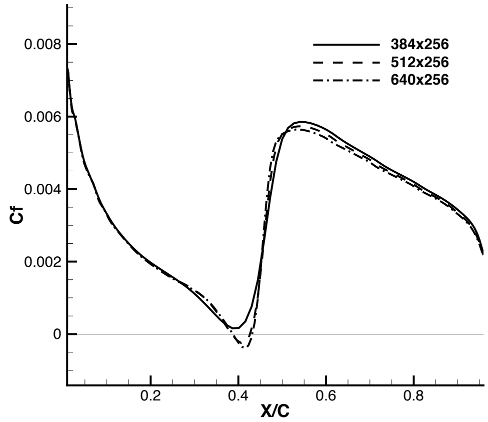

Figure 5–3: Effect of grid density in the x-direction on the convergence of the skin friction coefficient

among the three grids. It is interesting to note that the drag coefficient of the coarse grid seems to be unaffected by the absence of the laminar separation bubble on the upper surface. This is primarily due to the fact that even if the bubble was not captured, the transition point remains unaffected and hence it did not affect the total viscous contribution to the drag coefficient. Based on this study the 512×256 grid is sufficient to accurately resolve the transition point.

Table 5–1: Effect of Grid Density in the x-direction on the Convergence of Lift and Drag Coefficient

Cases	Lift Coefficient	Drag Coefficient	Pressure Drag	Viscous Drag
384×256	0.582	0.0069	0.0019	0.0050
512×256	0.577	0.0069	0.0019	0.0050
640×256	0.574	0.0069	0.0019	0.0050

A similar analysis is repeated to investigate the role of y^+ on the accuracy of the skin friction coefficient and the location of the transition point. Four grids with various y^+ values are generated while keeping the number of points in both the x- and y-directions the same as well as the expansion rate of the grids in the y-direction. The 512 × 256 grid with a y^+ of 0.1 from the grid study in the x-direction forms the base grid, where the wall spacing is 1×10^{-5} chord lengths and the distance to the farfield boundary is 15 chords. The 0.075, 0.15, and 0.3 y^+ grids are generated by changing the distance to the wall of the first grid cell. Figure 5–4 illustrates the distribution of the skin friction coefficient for the upper surface for the four grids. As the y^+ is refined, the turbulent portion of the skin friction converges, while the transition point as well as the size of the laminar separation bubble remains the same for all grids, since the latter is governed by the grid resolution in the x-direction. Table 5–2 shows that by decreasing the y^+, the lift and drag coefficients converge.

In conclusion, the $\gamma - \tilde{Re_\theta}$ transition model predicts the size and the location of the laminar separation bubble accurately and converges to a unique distribution of the skin friction coefficient for the 512 × 256 grid with a y^+ of 0.1 and as such it will be used as the minimum required grid size for all subsequent studies presented in this work.

Table 5–2: Effect of Average y^+ on the Convergence of Lift and Drag Coefficient

Cases	Y^+	Lift Coefficient	Drag Coefficient	Pressure Drag	Viscous Drag
512×256	0.3	0.585	0.0065	0.0018	0.0047
512×256	0.15	0.579	0.0068	0.0019	0.0049
512×256	0.1	0.577	0.0069	0.0019	0.0050
512×256	0.075	0.577	0.0069	0.0019	0.0050

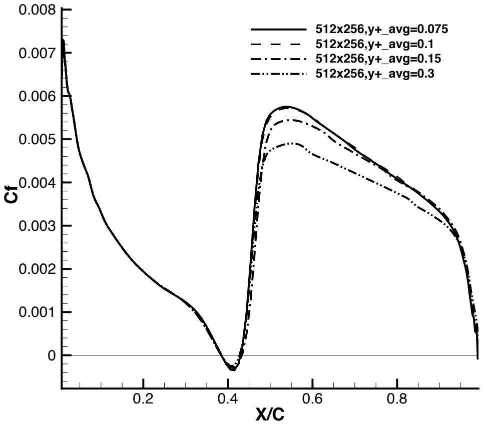

Figure 5–4: Effect of average y^+ on the convergence of the skin friction coefficient

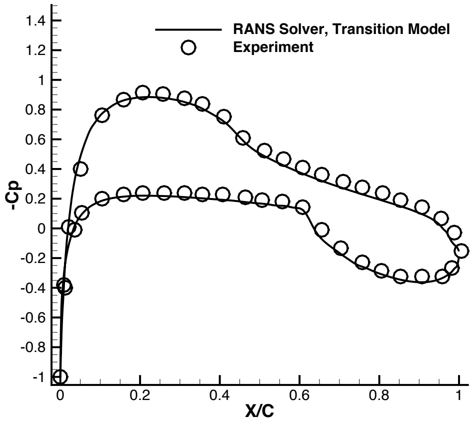

Figure 5–5: Pressure coefficient distribution for the NLF(1)-0416 airfoil

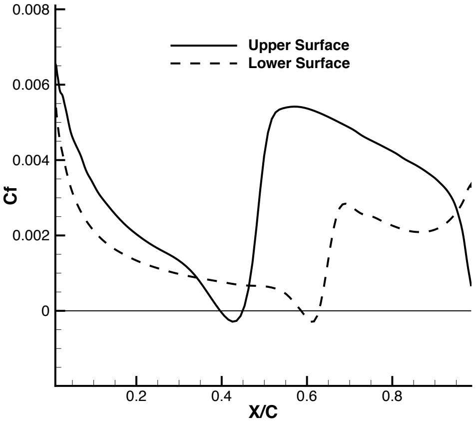

Figure 5–6: Skin friction coefficient distribution for the NLF(1)-0416 airfoil

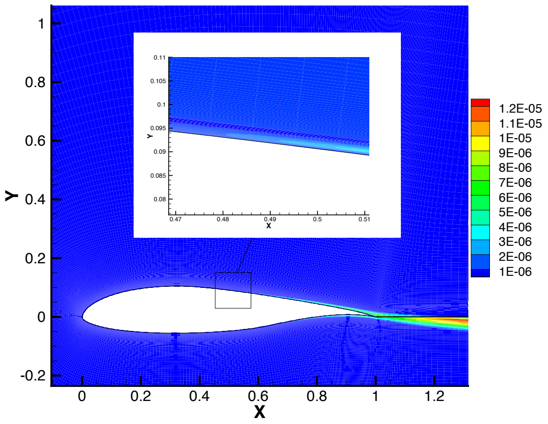

Figure 5–7: Distribution of turbulent eddy viscosity, μ_t for the NLF(1)-0416 airfoil

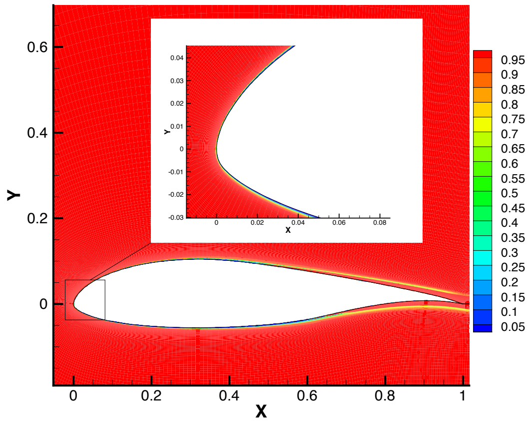

Figure 5–8: Distribution of turbulent intermittency factor, γ for the NLF(1)-0416 airfoil

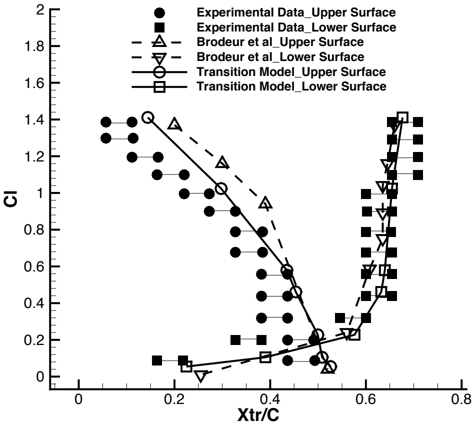

Figure 5–9: Transition points at different angles of attack for the NLF(1)-0416 airfoil at Re = 2×10^6

5.4 NLF(1)-0416 Airfoil

The pressure coefficient distribution around the NLF(1)-0416 airfoil at a Reynolds number 2×10^6 and angle of attack of 0 degree is compared with the experimental data [51] in figure 5–5. A good agreement between the laminar-turbulent flow solver and the experiment are observed. The favourable pressure gradient over the upper surface is maintained up to 20% of the airfoil chord, and approximately constant thereafter until the 45% chord position. Favourable pressure gradient is maintained over 60% of the lower surface, terminating at a transition point as illustrated by the kink in the pressure distribution. Laminar separation bubbles are present at these locations as demonstrated in figure 5–6 and reported by the experimental data [51] due to adverse pressure gradients. The laminar separation bubbles, reattaches as fully turbulent boundary layers on both upper and lower surfaces. Figure 5–7 illustrates the distribution of the turbulent eddy viscosity, μ_t, where the value is at its minimum of $1 \times 10^{-6}\mathrm{kg/(ms\sqrt{K})}$ everywhere in the flow, except for the region of the turbulent boundary layer. The insert in figure 5–7 demonstrates a close-up view of the transition region, where the contour illustrates that the eddy viscosity is gradually increasing from the 45% chord position. In figure 5–8, the contour of the intermittency factor, γ is illustrated, where the value in a large majority of the flow is unity, except in the laminar boundary layer where the value is nil. Since the intermittency factor is computed through a transport equation, the effects of this are evident in figure 5–8 where γ is convected downstream while bounding the turbulent boundary layer from the transition point. The intermittency factor progressively reaches a value of unity just aft of the trailing edge.

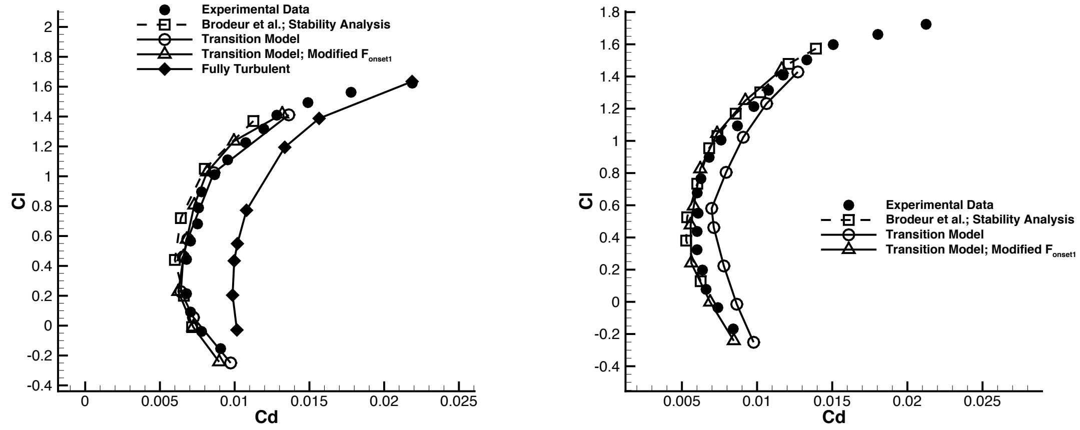

(a) Re = 2×10^6

(b) Re = 4×10^6

Figure 5–10: Drag polar for the NLF(1)-0416 airfoil

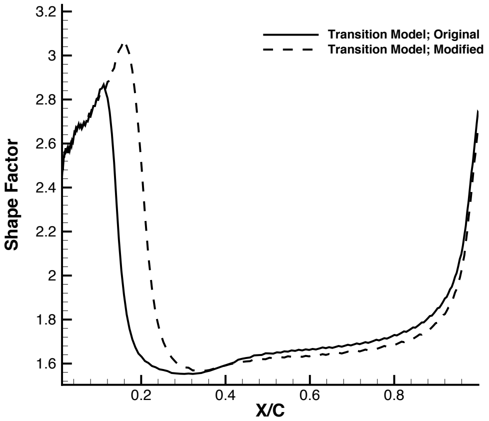

Figure 5–11: Shape factor distribution for the NLF(1)-0416 airfoil

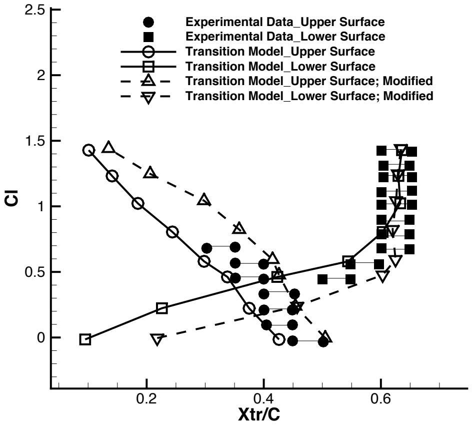

Figure 5–12: Transition points at different angles of attack for the NLF(1)-0416 airfoil at Re = 4×10^6

Figure 5–9 compares the locations of the transition points obtained by the experimental results [51], the numerical results of Brodeur et al. [5] which are based on the e^n approach, and the $\gamma - \tilde{Re}_\theta$ transition model at various angles of attack at a Reynolds number of 2×10^6. The figure correlates the transition location to the lift coefficient. There are two points reported by the experimental data at each lift coefficient. The first point corresponds to the end of the laminar region while the second indicates the turbulent reattachment point. The numerical transition points reported in this work conforms to the latter. The general trend of the movement of the computed transition point is to start around the mid-chord and move towards the trailing edge on the upper surface while on the lower surface, transition starts at 20% and moves rapidly to about 60% at a lift coefficient of 0.2 and remains relatively steady with a gentle increase to the 70% chord position. At low lift coefficients, analogous to an angle of attack range of -3.5° to 0°, the transition model provides comparable results to that reported by Brodeur et al. [5]. However, as the lift coefficient increases, the model places the transition point slightly closer to the experimental data for both surfaces. At lower lift coefficients, transition is due to the presence of a laminar separation bubble, while at higher lift coefficients natural transition occurs. Figure 5–9 illustrates that the $\gamma - \tilde{Re}_\theta$ transition model demonstrates its ability to simulate both types of laminar-turbulent transition processes, within a robust numerical framework where the convergence of the residuals remain unaffected and all parameters associated with the transition and turbulence models were kept frozen during the entire study.

The drag polar obtained from the present laminar-turbulent flow solver is compared to the experimental data [51] and the numerical results of Brodeur et al. [5] in figure 5–10(a). The drag coefficient predicted by the transition model compares very well for a wide range of lift coefficients, while, the fully turbulent simulations over predicts the drag by approximately 30 counts except at the maximum lift coefficient of 1.6, where transition occurs near the leading edge. To study the effect of Reynolds number on the accuracy and capability of the laminar-turbulent flow solver, the drag polar at a Reynolds number of 4×10^6 is compared in figure 5–10(b) against the experimental results. The transition model shows an acceptable agreement at high lift coefficients due to the fact that transition occurs closer to the leading edge, but over predicts the drag coefficients at other lift coefficients. These results were obtained with the original constant of 2.193 based on Langtry and Menter's [32] model which regulates the ratio between the vorticity, Re_v, and momentum-thickness Reynolds numbers, Re_{θ_c}. The modified correlation, F_{onset}, developed in this work and detailed in subsection 2.11.3, compares very well at all lift coefficients. To better understand the effect of the modification, in figure 5–11, the boundary layer shape factor distribution for the upper surface is compared between the original and modified models at a Reynolds number of 4.0×10^6 and an angle of attack of $7°$. The original model allows the flow to develop to a point where the shape factor reaches a value of 2.9, which places it at the upper bound of the range for moderate shape factors, $2.3 < H < 2.9$. Employing the modified calibration constant allows the laminar flow to further develop, where the boundary layer shape factor grows slightly above 3, and shifts the transition point towards the trailing edge by less then 5% of the chord; thereby lowering the viscous drag contribution. To further validate the model, the transition points are compared between the two models in figure 5–12, where the modified model places the transition location closer to the experimental turbulence reattachment point at all lift coefficients. This supports the observation that at higher Reynolds numbers, the transition point moves towards the leading edge due to a moderate increase in the adverse pressure gradient, resulting in larger boundary layer shape-factors, thus a recalibration of the original F_{onset} correlation function is necessary. The recalibration of the F_{onset} correlation function has no effect at a Reynolds number of 2×10^6 as illustrated in figure 5–10(a). For Reynolds numbers higher than 4×10^6, further experimental data and numerical investigations are required to validate the modified $\gamma - \tilde{R}e_{\theta t}$ transition model. However, Langtry et al. [31] have shown the effect of having the $\gamma - \tilde{R}e_{\theta t}$ transition model in comparison with fully turbulent solutions for high Reynolds number cases such as Eurocoptor airframe at Reynolds number of 30×10^6 [31]. Using the transition model reduces the predicted drag around 5% in comparison with the fully turbulent solution without having any effect on the convergence of the flow solver [31].

5.5 S809 Wind Turbine Profile

This section presents the validation of the laminar-turbulent flow solver with the $\gamma - \tilde{R}e_{\theta}$ transition model for the S809 wind turbine profile. Figure 5–13 compares the distribution of the pressure coefficients around the S809 wind turbine profile at the designed Reynolds number of 2×10^6 and an angle of attack of 0 degree to the experimental results [52]. The pressure distribution agrees very well with the experimental data. Figure 5–14 illustrates the distribution of the skin friction

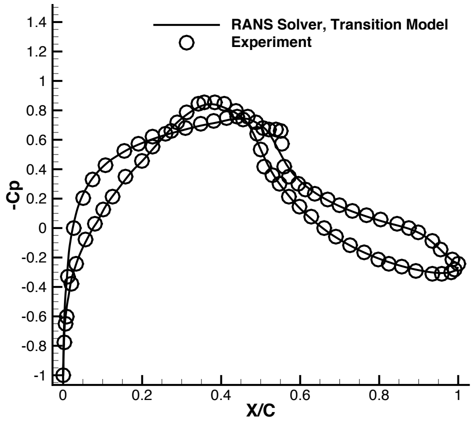

Figure 5–13: Pressure coefficient distribution for the S809 airfoil

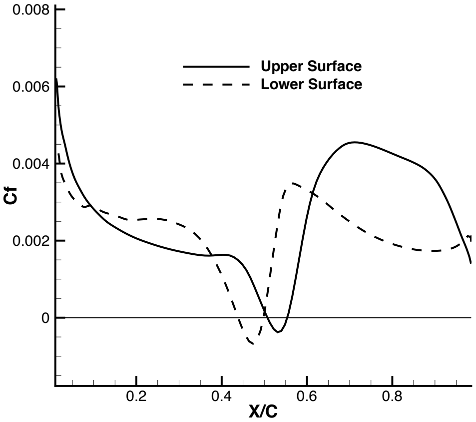

Figure 5–14: Skin friction coefficient distribution for the S809 airfoil

coefficient for the upper and lower surfaces. The negative values of the skin friction coefficients indicate the formation of laminar separation bubbles at the midchord for the upper surface and forward of the midchord for the lower. This observation agrees very well with the experimental data [52]. As the angle of attack is increased, the laminar separation bubble on the upper surface decreases in length and moves forward as illustrated in figure 5–15. The bubble is smallest at an angle of attack of 5° and disappears thereafter as the angle is increased further.

Figure 5–16 compares the location of the transition points predicted by the $\gamma - \tilde{Re}_\theta$ transition model at a Reynolds number of 2×10^6 against experimental results [52] and the numerical results of Langtry et al. [32]. To maintain consistency with the experimental data [52], the reported numerically computed transition point corresponds to the turbulent reattachment point. The obtained numerical results are in excellent agreement with the experimental data [52]. At angles of attack below 5°,

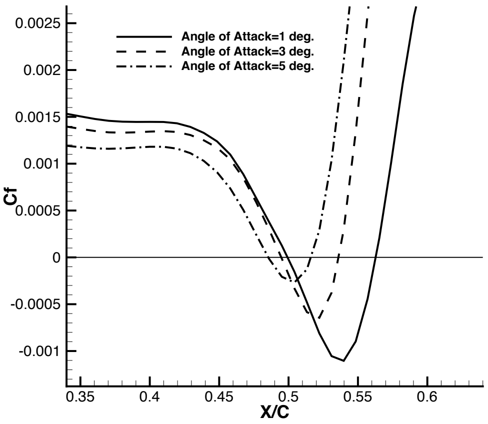

Figure 5–15: Effect of angle of attack on the size of the laminar separation bubble over the upper surface of the S809 airfoil

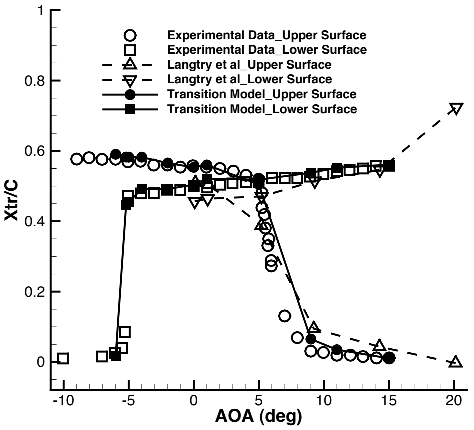

Figure 5–16: Transition points at different angles of attack for the S809 airfoil

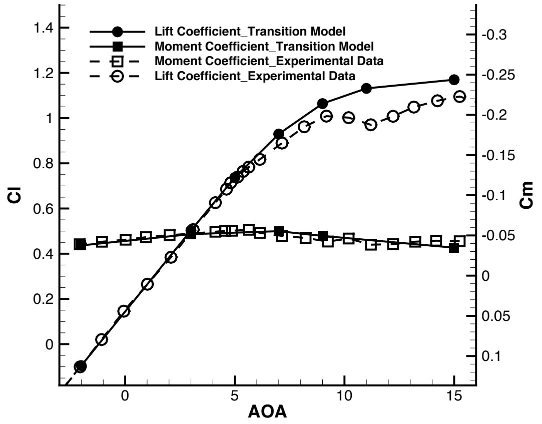

Figure 5–17: Lift and moment coefficients at different angles of attack for the S809 airfoil

the upper surface transition point remains approximately aft of the midchord. As the angle increases further, transition moves forward steadily and remains at the leading edge from an angle of attack of 9°. The laminar separation bubble on the upper surface is the primary mechanism of the boundary-layer transition to turbulent flow up to an angle of attack of 5°. On the lower surface, the numerical result reports that transition hovers approximately at the midchord for a large range of angles of attack and jumps to the leading edge at -6°, compared to -5.2° as that described by the experimental results. A laminar separation bubble is present for angles of attack of -5.6° and greater, but the bubble length decreases between angles 0° and -5° until natural transition occurs at the leading edge at -6° with a turbulent separation at the trailing edge.

Next we evaluate the sectional characteristics by first investigating the lift curve slope as well as the moment coefficient and finally the drag polar at various Reynolds numbers. Figure 5–17, compares the lift and moment coefficients at various angles of attack with the experimental data [52]. The numerical results compares very well from -2° up to 9°. An illustration of the streamlines around the trailing-edge over the upper surface for various angles of attack are presented in figure 5–18. At an angle of 5°, a very small amount of turbulent trailing-edge separation occurs. The amount of separation increases slowly from 5° to 9°, which agrees very well to experimental observations [52]. At 11° the lift coefficient does not experience a reduction as that observed experimentally. Figure 5–18, demonstrates that the turbulent separation moves forward to the 70% chord position. We believe that the discrepancy in the lift coefficient is largely due to the fact that the turbulence model was unable to capture the correct size of the turbulent separation. At 15°, the lift coefficient is slightly over predicted and the turbulent separation jumps to the midchord as reported by the experimental data. The calculated moment coefficients agree very well with the experimental data over the entire range of angles of attack. The numerical lift curve slope at all angles is akin to results reported by Sorensen [54].

Figure 5–19 illustrates the drag polar at various Reynolds numbers. Since the S809 airfoil was designed to operate at a Reynolds number of 2×10^6, we will initially compare the results at this Reynolds number before validating at other Reynolds numbers. The S809 wind turbine airfoil can maintain a low drag coefficient for a wide range of angles of attack from around -5 to 5 degrees which are respectively the lower and upper limits of the laminar bucket. The airfoil was specifically designed to achieve low profile-drag coefficients for a range of lift coefficients. Both the original and modified transition models, with the recalibrated F_{onset} function, agree very well at low lift coefficients within the laminar region. However, at the lower laminar bucket, the modified model predicts more accurate drag coefficients at an equivalent lift, resulting in a well defined laminar bucket. We believe that the presence of a greater adverse pressure gradient, increases the boundary layer shape factor and thus the error between the maximum value of the vorticity Reynolds number and the momentum-thickness Reynolds number increases; therefore requiring a recalibration of the F_{onset} function. The upper limit of the laminar bucket occurs at an angle of attack of 5° at a lift coefficient of 0.74 and both models compare well to the experimental data. As expected the fully turbulent solutions over predict the drag coefficients.

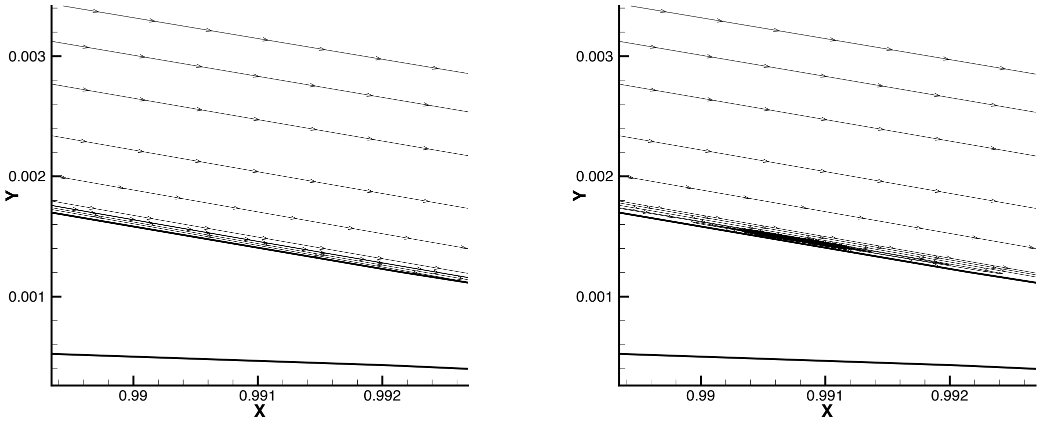

(a) Angle of attack of 5 degrees (b) Angle of attack of 7 degrees

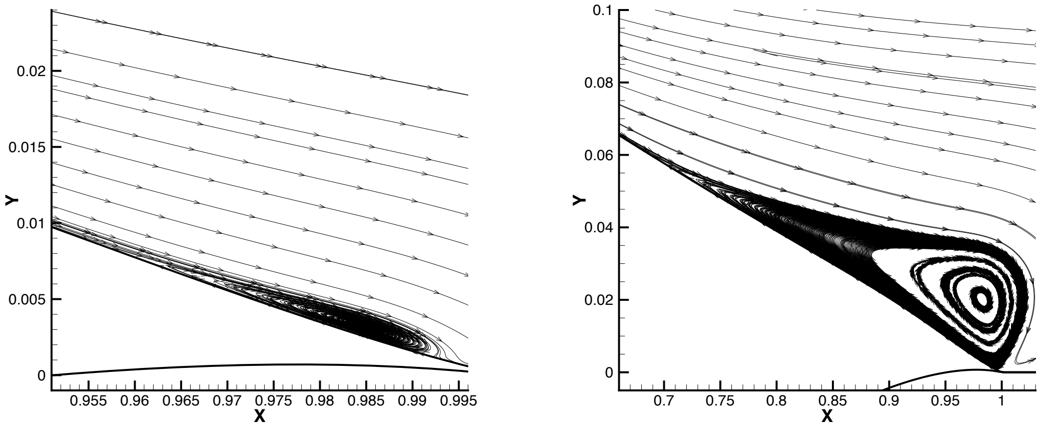

(c) Angle of attack of 9 degrees (d) Angle of attack of 11 degrees

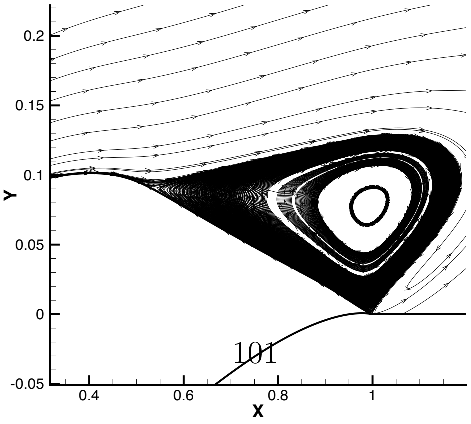

(e) Angle of attack of 15 degrees

Figure 5–18: Turbulent separated regions at various angles of attack

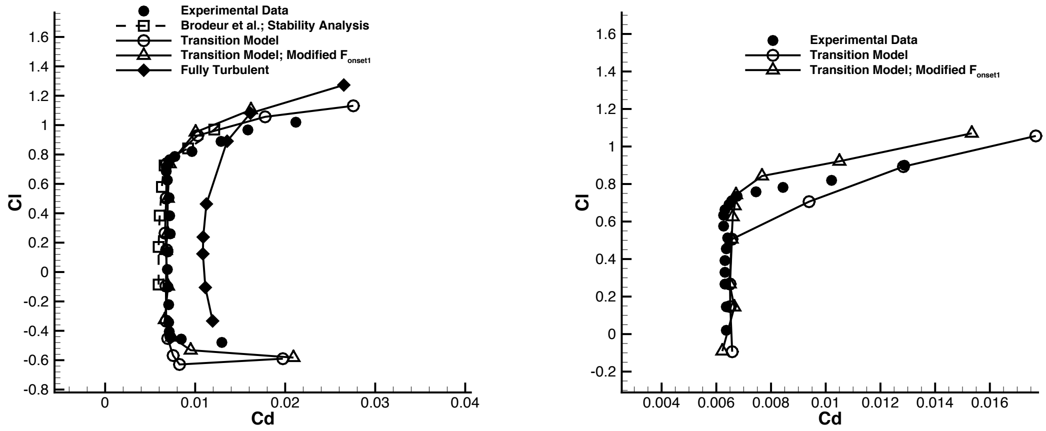

(a) Re = 2.0×10^6

(b) Re = 2.5×10^6

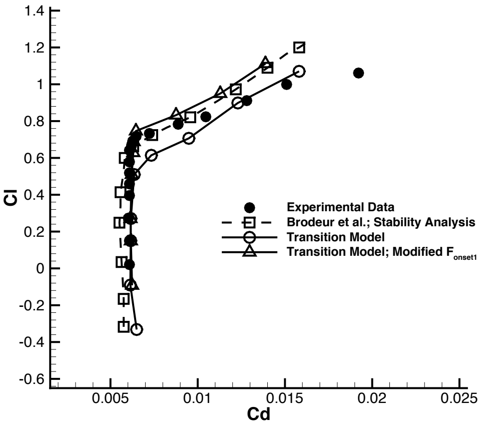

(c) Re = 3.0×10^6

Figure 5–19: Drag polar for the S809 airfoil

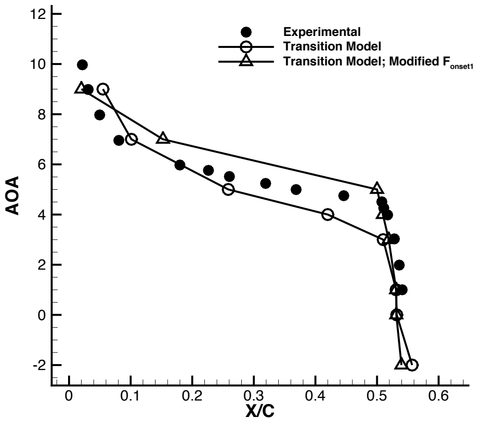

Figure 5–20: Transition points at different angles of attack for the S809 airfoil at $Re = 3.0 \times 10^6$

As the Reynolds number increases to 2.5×10^6, figure 5–19(b), the modified model predicts the upper limit of the bucket with greater accuracy; however, similar to the 2×10^6 Reynolds number case, the difference is negligible at low lift coefficients. The same is true at a Reynolds number of 3.0×10^6, as illustrated in figure 5–19(c). In figure 5–20 the obtained transition points from the modified and original transition models are compared to the experimental data at a Reynolds number of 3.0×10^6 for the upper surface. The figure illustrates that the original model, prematurely moves the transition point towards the leading edge as the adverse pressure gradient increases; thereby over predicting the drag coefficient. While the modified model, follows closer the experimental transition points. The obtained results show that as the Reynolds number increases, the modified transition model improves the accuracy of the transition points and drag polars in comparison with the experimental data.

CHAPTER 6
Optimization Results

In this section, the optimization of the NLF(1)-0416 and S809 airfoils using the $\gamma - Re_{\theta t}$ transition and $k - \omega$ SST turbulence models and their adjoint counterparts for various flight conditions will be demonstrated. In addition, the effectiveness of the choice of cost functions to reduce the total drag coefficient for the new framework is investigated.

6.1 Introduction

The aerodynamic shape optimization framework is employed to design new NLF airfoils for minimizing the drag, while maintaining or maximizing the lift. The presented adjoint-based design code is employed to optimize the NLF(1)-0416 and S809 airfoils. The airfoil shape is modified to maintain a favourable pressure gradient and postpone the onset of transition over the upper and lower surfaces. This reduces the total drag especially the skin friction component while the lift is maintained or maximized. The results demonstrate the capability of the developed adjoint-based optimization and design framework to design new natural laminar flow (NLF) airfoils.

6.2 Optimization Results Using the $k - \omega$ SST Turbulence and $\gamma - \tilde{Re}_{\theta t}$ Transition Models

In transonic flow, especially in the presence of a shock wave, pressure drag is a dominant component of the total drag. Aerodynamic shape optimization minimizes the total drag by removing the shock and reducing the pressure drag with marginal reduction or sometimes an increase in the skin friction drag. At transonic Mach numbers, the sensitivity of the drag coefficient with respect to the surface geometry tends to peak in the vicinity of shock waves and this greatly influences the optimization algorithm and the resulting search direction. For the choice of parametrization, the modified geometry experiences very localized changes, typically a slight curvature reduction immediately upstream of the shock wave. On the other hand, in low subsonic flows where the skin friction drag is dominant, the sensitivity is less concentrated at particular geometrical locations and aims towards much larger transformation of the airfoil geometry. Hence our immediate goal before a multitude of optimization cases are explored is to establish cost functions that best exploit the design space spanned by the design variables. Here the use of the production of the turbulence kinetic energy, k, as a possible alternative or supplementary cost function to the total drag coefficient will be investigated to reduce the skin friction drag. Unlike the drag coefficient, the production of the turbulence kinetic energy appears as a source term in the transport equation bearing it's name. It's non-zero within the turbulent boundary layer and is proportional to the eddy viscosity as well as the magnitude of the vorticity vector based on the $k - \omega$ SST-V version of the model.

In figure 6–1, the effect of the production of k as a supplementary cost function to total drag coefficient is illustrated. The figure demonstrates that its sensitive not only to the design variables in the immediate vicinity but is affected by a large range of surface grid points. To show the effectiveness of using the production of turbulent kinetic energy (TKE) as the cost function in addition to the total drag, the NLF(1)-0416 airfoil is redesigned to maintain lift and reduce the total drag with

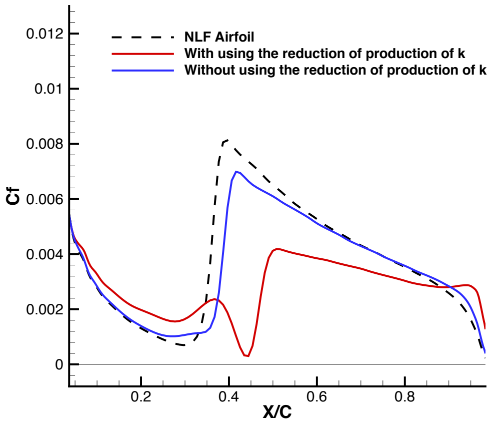

Figure 6–1: Distribution of skin friction coefficient of NLF(1)-0416 airfoil at 5°; effect of employing the production of k as the cost function

and without using the production of k as the cost function. Table 6–1 describes that when the production of k is added, the skin friction component of drag is reduced more than the case where only the total drag is minimized as long as the initial lift coefficient is maintained during the optimization process for both cases. In figure 6–1 the skin friction distributions over the upper surface of the optimized airfoils with and without employing the production of k are compared. As the production of turbulent kinetic energy decreases, the turbulent viscosity level is lowered and the transition point is postponed, and consequently the skin friction component of the total drag which is proportional to μ_t, is reduced, resulting in a greater reduction in the total drag. In both cases the initial lift coefficient is constrained and is well maintained during the optimization process.

Figure 6–2 compares the initial and optimized airfoil shapes. With the addition of the production of k as a cost function, the airfoil camber increases and the

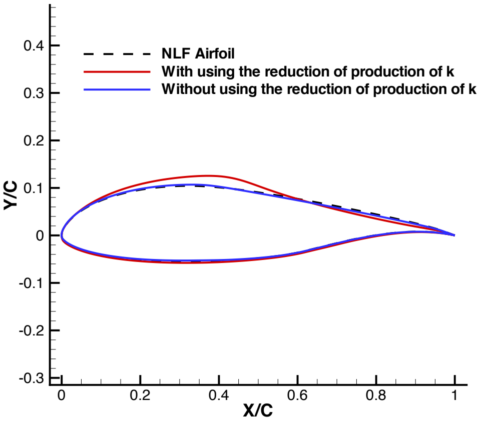

Figure 6–2: Shape modifications of NLF(1)-0416 airfoil at 5°; effect of employing prod_k as the cost function

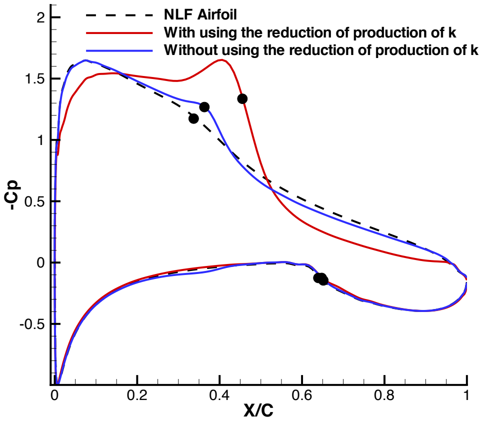

Figure 6–3: Distribution of pressure coefficient of NLF(1)-0416 airfoil at 5°; effect of employing prod_k as the cost function

Table 6–1: Comparison of drag coefficients for the NLF(1)-0416 and optimized airfoils at 5° with and without using the reduction of prod_k as the cost function

Cases	C_d	C_{dp}	C_{df}
NLF(1)-0416	0.0086	0.0032	0.0054
Optimized with prod_k	0.0074	0.0029	0.0045
Optimized without prod_k	0.0083	0.0030	0.0053

curvature is modified to maintain the favourable pressure gradient and postpone the transition point. Figure 6–3 illustrates that when the production of k is excluded from the cost function, the optimizer is unable to extend the favourable pressure gradient and the laminar flow over the airfoil.

To investigate the effect of the addition of the production of k further, we compare the adjoints of k, in figures 6–4(a) and 6–4(b). The adjoint solution demonstrates the sensitivity of the objective function to perturbations to the residual of the governing equation. The adjoint values are mostly active in the fully turbulent region extending from the transition point, demonstrating that perturbations of the residual of k in this region would contribute towards the reduction of the objective function. However, in figure 6–4(b), when the production of the turbulent kinetic energy is excluded from the cost function, a contour plot of the adjoint of k does not display the gradient within the boundary layer displayed in figure 6–4(a). In the case of the $\gamma - Re_{\theta t}$ model, figure 6–5 presents the distribution of the adjoint values for γ. The value is largely zero except for the transition region as illustrated by the insert in figure 6–5(a). The adjoint solution correctly highlights the location of the transition point and demonstrates its sensitivity towards the reduction in the production of the turbulent kinetic energy. The largest magnitude is centred approximately at 35% of the chord, which was earlier demonstrated in figure 6–1 as the transition location. Removal of the production of the turbulent kinetic energy from the cost function, produces an adjoint of γ that is largely nil throughout the computational domain. As presented in Chapter 4, the gradient of the objective function with respect to the design variable is equivalent to the dot product of the adjoint solution to the sensitivity of the residual to the design variable. The adjoint solution operates as a weighting function, and as such de-emphasizes the contribution of the transition point to the reduction of the total drag coefficient.

This investigation establishes the need for the addition of the production of the turbulent kinetic energy to the objective function to demonstrate successful reduction in the total drag coefficient via reduction of the skin friction drag. All subsequent cases in this chapter will employ both the drag coefficient and the production of k.

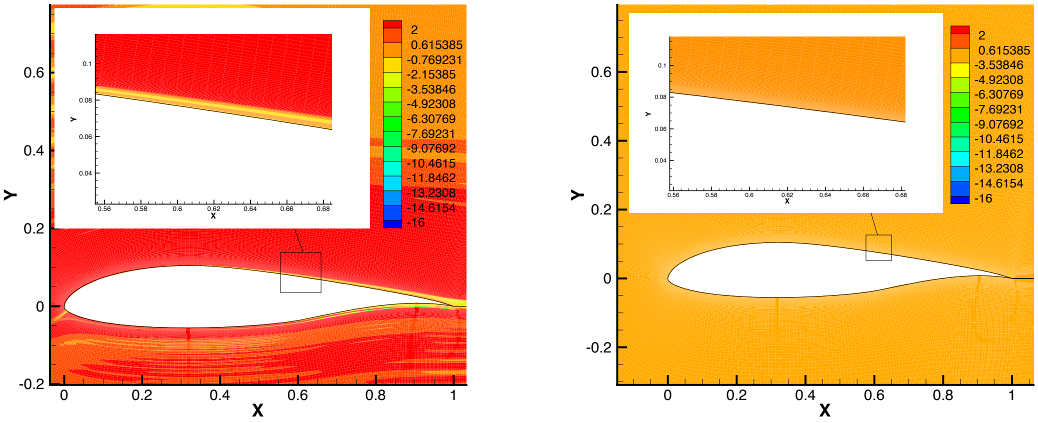

(a) With using the reduction of prod_k (b) Without using the reduction of prod_k

Figure 6–4: Distributions of adjoint costate of k at 5 degrees with and without using the reduction of prod_k as the cost function

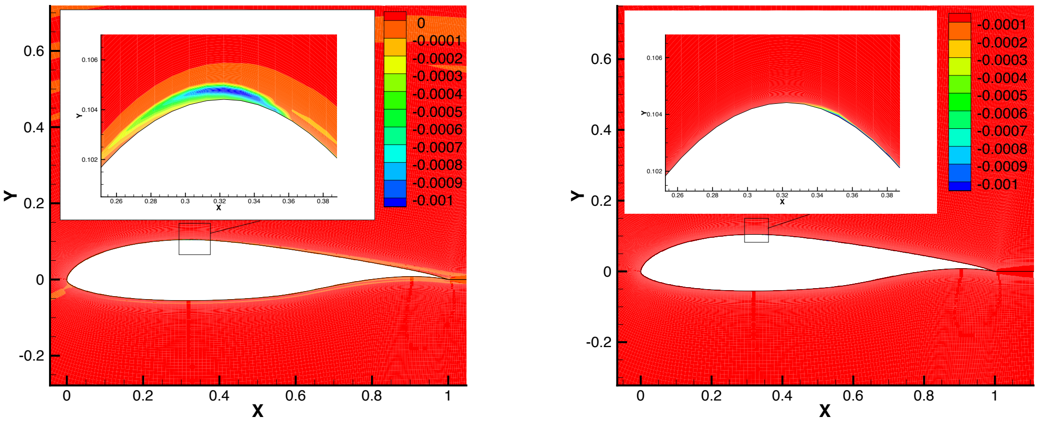

(a) With using the reduction of prod_k (b) Without using the reduction of prod_k

Figure 6–5: Distributions of adjoint costate of γ at 5 degrees with and without using the reduction of prod_k as the cost function

6.3 NLF(1)-0416 Airfoil; Minimize Drag, while Maintain C_l

In the subsequent sections, several cases will explore the use of the γ-$Re_{\theta t}$ transition model to improve the aerodynamic performance of the NLF(1)-0416 and S809 airfoils by primarily reducing the drag coefficient. In the first case, we will minimize the drag coefficient, while maintaining the lift coefficient at a typical cruising lift coefficient for a small general aviation aircraft. This is in sharp contrast to the typical approach of designing high lift-to-drag ratio airfoils at low Reynolds numbers. We believe this to be a more realistic test case to demonstrate the developed methodology. The performance of the redesigned airfoil at various angles of attack will be investigated to demonstrate the approach. In the second case, we will explore the ability of the model to design high lift-to-drag airfoils.

6.3.1 Angle of Attack of 0 Degree

In this subsection, the ability of the approach at redesigning the NLF(1)-0416 airfoil at a Reynolds number of 2×10^6 and an angle of attack of zero degrees, where the lift coefficient is 0.46, will be investigated. The objective is to minimize the total drag and the production of the turbulent kinetic energy with respect to the airfoil geometry, subject to maintaining the lift and pitching moment coefficients, while the chord-wise thickness distribution is allowed to vary within 10% of the original thickness distribution. The rationale for this choice is in line with our decision to employ the new framework to design airfoils that are applicable for general aviation type aircraft. Absence of a thickness constraint would allow the optimizer to investigate classical Liebeck type airfoils, where the low thickness ratio in much of the aft portion of the airfoil may not be suitable for general or commercial aircraft.

Table 6–2: Comparison of the drag coefficients for the NLF(1)-0416 and optimized airfoils at 0°; maintain the lift and reduce the drag

Cases	C_d	C_{dp}	C_{df}
NLF(1)-0416	0.0066	0.0018	0.0048
Optimized	0.0055	0.0014	0.0041

Table 6–2 lists the initial and optimized lift, drag, and pitching moment coefficients. The total drag during the optimization process is reduced by 11 counts and its history is shown in figure 6–6. The skin friction drag decreases by 7 counts while the pressure component is reduced by 4 drag counts. The pitching moment is maintained with about a 2% tolerance, while lift is kept within a percent where its history is presented in figure 6–7. Figure 6–8 illustrates the initial and final skin friction coefficients, where the upper transition point moves towards the trailing edge from 44% to 61% of the chord position. In addition to the movement of the upper transition point which extends the laminar flow, the reduction of the turbulent viscosity assists in the reduction of the skin friction by 7 drag counts. The extension of the laminar flow region and the reduction of the skin friction drag in the turbulent region has decreased the overall boundary layer height and hence a modest reduction of 4 drag counts is achieved for the pressure drag component. In figure 6–9 the distributions of the pressure coefficients are shown. The airfoil shape is altered to maintain the favourable pressure gradient as much as possible in order to augment the boundary layer stability and postpone the onset of transition. The initial and optimized airfoil shapes are compared in figure 6–10. The increased camber of the airfoil surface increases the favourable pressure gradient region, thus allowing the airfoil to maintain the lift coefficient and promote the extension of the laminar boundary layer over the

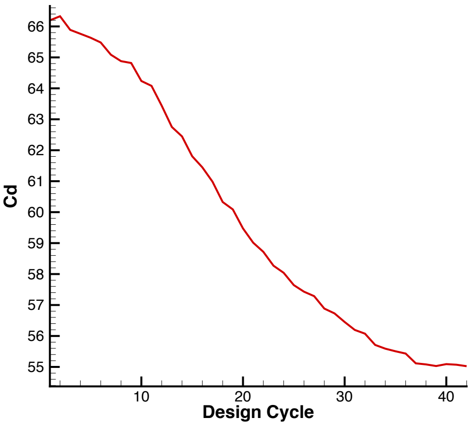

Figure 6–6: Drag Coefficient History at 0°

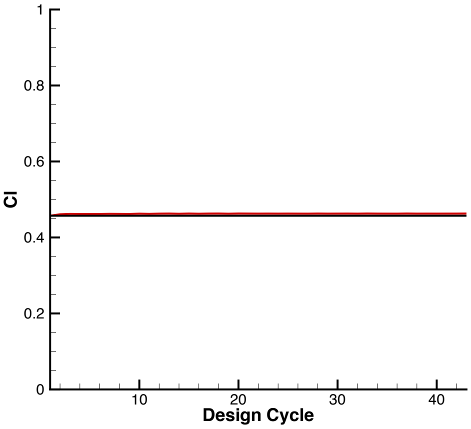

Figure 6–7: Lift Coefficient History at 0°

upper airfoil surface in order to reduce drag. A concave type pressure recovery is developed in the post transition region. Modifications to the lower surface geometry is marginal with negligible change to the pressure and skin friction distributions. This is primarily due to the lower sensitivities of the lift and drag coefficients with respect to the lower surface geometry compared to the upper surface. It is important to note that this is generally not the occurrence as will be demonstrated in the following cases.

An important characteristic of NLF airfoils are their presumably lower performance in fully turbulent flow. In figure 6–11 the drag polar of the optimized and initial airfoils are compared for transitional and fully turbulent flows. Along the drag polar for transitional flow, the optimized airfoil generates less or equivalent levels of drag for the entire range of angles of attack except at 9° where the drag increases. At low angles of attack the fully turbulent drag remains the same as that of the initial

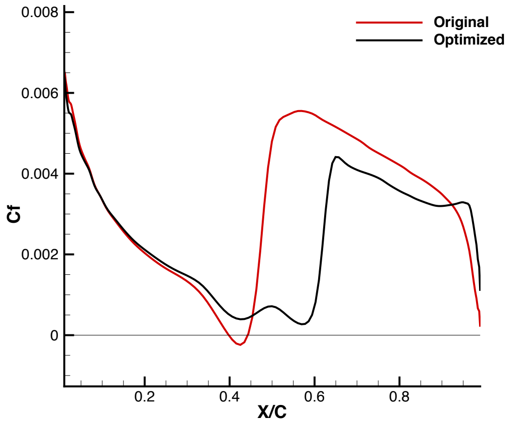

Figure 6–8: Distribution of skin friction coefficient for the upper surface of NLF(1)-0416 airfoil at 0°; maintaining lift and reducing drag

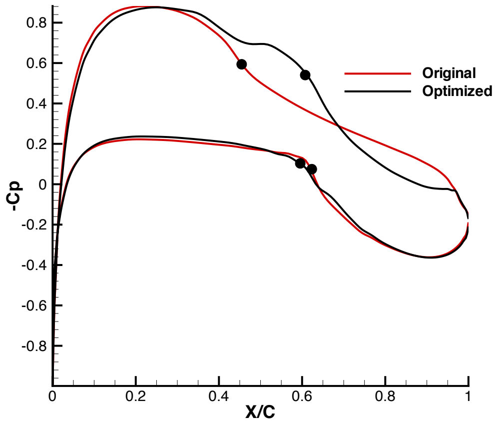

Figure 6–9: Distribution of pressure coefficient of NLF(1)-0416 airfoil at 0°; maintaining lift and reducing drag

airfoil while at higher angles the drag begins to increase. In figures 6–12 and 6–13 the drag and lift coefficients of the NLF(1)-0416 and optimized airfoils at various angles of attack are compared. The optimized airfoil has lower drag coefficients at low angles of attack around 0° which is the design point, while it begins to rise at higher angles. In addition, the lift coefficients for the optimized airfoil are well maintained at all angles of attack in comparison with the NLF(1)-0416 airfoil. This study demonstrates that a single point optimization of an airfoil to extend the laminar region for the purpose of drag reduction is able to produce an airfoil with comparable fully turbulent flow performance. The investigation is not complete since a multipoint optimization together with a constraint on the performance at fully turbulent flows is warranted. The illustrated study is a first attempt and a multipoint optimization should be part of future work.

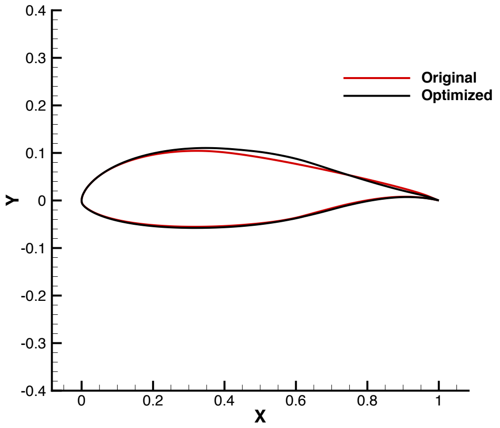

Figure 6–10: Shape modifications of NLF(1)-0416 airfoil at 0°; maintaining lift and reducing drag

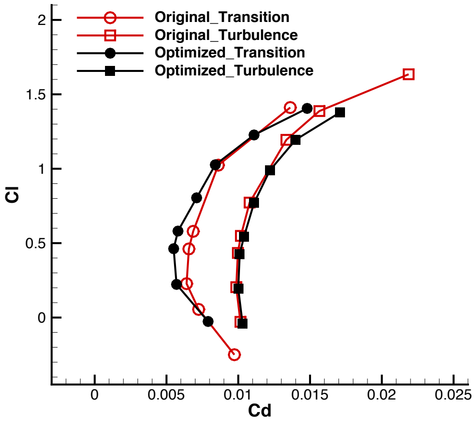

Figure 6–11: Drag polar for the optimized and NLF(1)-0416 airfoils at 0°

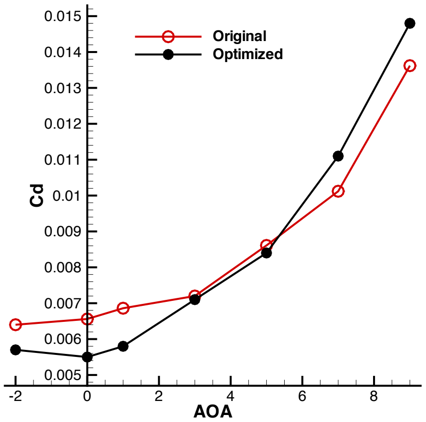

Figure 6–12: Drag coefficient versus angle of attack for the initial and optimized airfoil at 0°

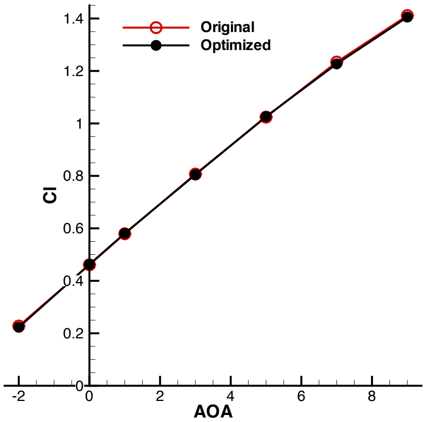

Figure 6–13: Lift coefficient versus angle of attack for the initial and optimized airfoil at 0°

Table 6–3: Effect of y^+ on the lift and drag coefficients of the optimized airfoil at 0°

Y^+	C_d	C_{dp}	C_{df}
0.1	0.0055	0.0014	0.0041
0.075	0.0054	0.0013	0.0041

To ensure that the observed reduction in the skin friction and pressure drags are accurate, a y^+ study is performed on the final airfoil shape while keeping the overall grid size constant. The rationale for this decision is based on the grid study presented in Chapter 2. To determine the effect of y^+ on the optimized airfoil, a new grid with $y^+ = 0.075$ is generated. Table 6–3 demonstrates that the two grids differ by one drag count, confirming the reductions observed in the skin friction and pressure drags during the optimization process.

6.3.2 Angle of Attack of 5 Degrees

In this subsection, the NLF(1)-0416 airfoil is redesigned at a Reynolds number of 2×10^6 and an angle of attack of 5 degrees. Also in this case, we illustrate the effectiveness of including the adjoint equations of both the transition and turbulence models. In figure 6–14 the original airfoil geometry is compared to the optimized airfoil shapes with and without using the adjoint equations of the transition and turbulence models, while in figure 6–15, the pressure distributions are compared. By employing a complete linearization of the non-linear governing equations, the airfoil geometry is modified in such a manner that the peak pressure reduces, while the favourable pressure gradient region is extended to the mid-chord. Maintaining the pressure gradient allows the upper transition point to move downstream towards the trailing edge. The corresponding airfoil shape as shown in figure 6–14, illustrates that the optimizer achieves this by increasing the camber in the forward portion of the airfoil to maintain the total lift coefficient, while simultaneously increases the favourable pressure gradient and thus allowing the transition point to move aft. In figures 6–16 and 6–17 the distributions of the skin friction coefficients are compared for the upper and lower surfaces respectively. Maintaining a favourable pressure gradient accelerates and energizes the laminar flow over the upper surface. This stabilizes the boundary layer and postpones the upper transition point from 35% to 44% of the airfoil chord length. Another interesting feature of the final design is the reduction of the camber in the pressure recovery region. Here a reflex camber is introduced, producing a Stratford-type pressure recovery, with a reduction in the turbulent shear stress as illustrated in figure 6–16. The delay in the transition from laminar to fully turbulent flow and the reduction of the turbulent shear stress lowers the total skin friction drag of the airfoil. In figure 6–18 the final distribution of the adjoint variable of the turbulent kinetic energy, k, is shown. In comparison with the initial distribution (figure 6–4(a)), the production of the turbulent kinetic energy in the vicinity of the airfoil is reduced and the level of the corresponding adjoint variable decreases. Figure 6–19(b) demonstrates the final distribution of the adjoint variable of γ. Although the adjoint variable is still active along the boundary layer especially around the transition point; however, the values have been reduced by an order of magnitude against the initial distribution (figure 6–19(a)). In the absence of the adjoint equations for the turbulence and transition models, as expected, the incomplete sensitivities are unable to change the airfoil geometry to reduce the total drag coefficient. This example demonstrates the effectiveness and the need for a

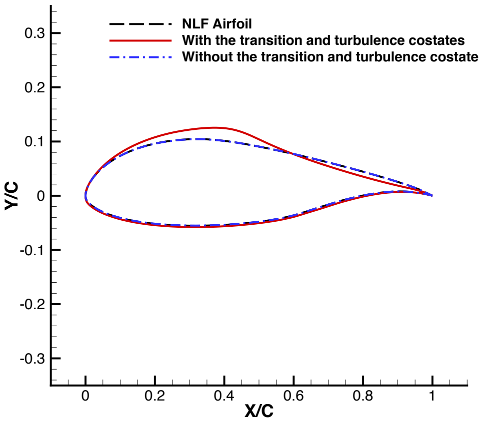

Figure 6–14: Shape modifications of NLF(1)-0416 airfoil at 5°; maintaining lift and reducing drag

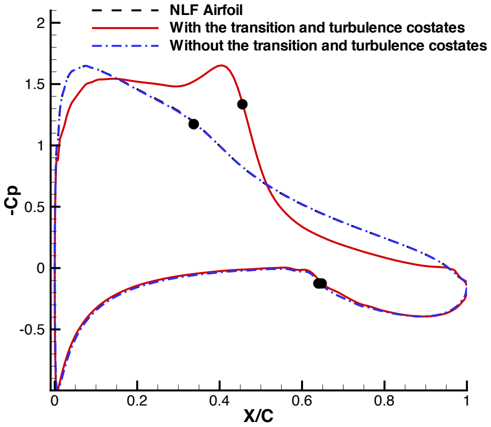

Figure 6–15: Distribution of pressure coefficient of NLF(1)-0416 airfoil at 5°; maintaining lift and reducing drag

complete adjoint system to successfully extend the laminar region and reduce the skin friction drag of the airfoil.

Table 6–4 compares the total drag coefficients as well as the pressure and skin friction drag components for the initial and optimized airfoils. Figures 6–20 and 6–21 illustrate the design history of the total drag and lift coefficients respectively. The lift coefficient is maintained while the pressure drag decreases by 3 counts, and the skin friction component is reduced by 9 drag counts. The marginal reduction in the pressure drag is primarily due to a lower boundary layer thickness due to a larger region of laminar flow as well as lower skin friction coefficients in the turbulent region. The combined effect reduces the thickness of the turbulent wake and thus contributes towards a lower pressure drag. Excluding the turbulence and transition model adjoints has no effect on the final drag coefficients. In figure 6–22 the design

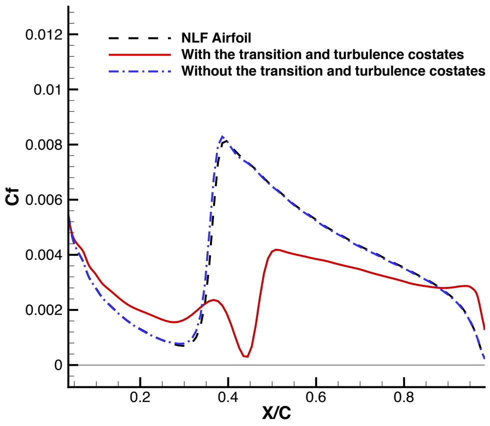

Figure 6–16: Distribution of skin friction coefficient for the upper surface of NLF(1)-0416 airfoil at 5°; maintaining lift and reducing drag

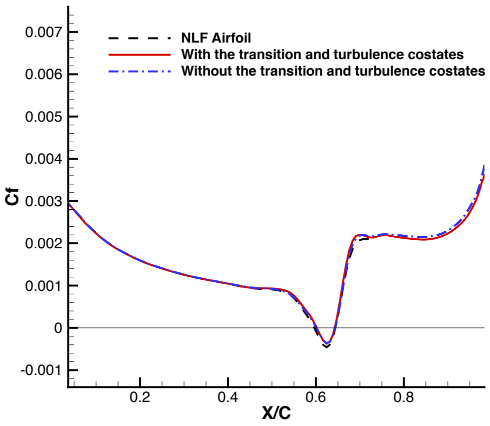

Figure 6–17: Distribution of skin friction coefficient for the lower surface of NLF(1)-0416 airfoil at 5°; maintaining lift and reducing drag

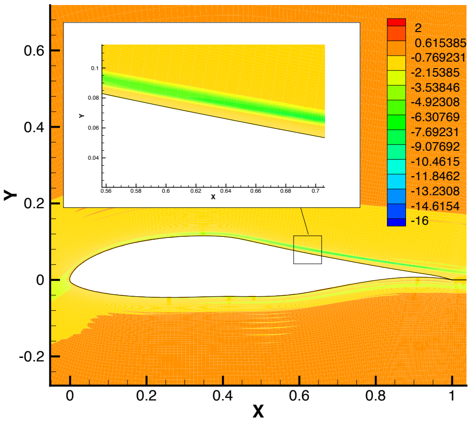

Figure 6–18: Final distribution of adjoint costate of k for the optimized airfoil at 5 degrees

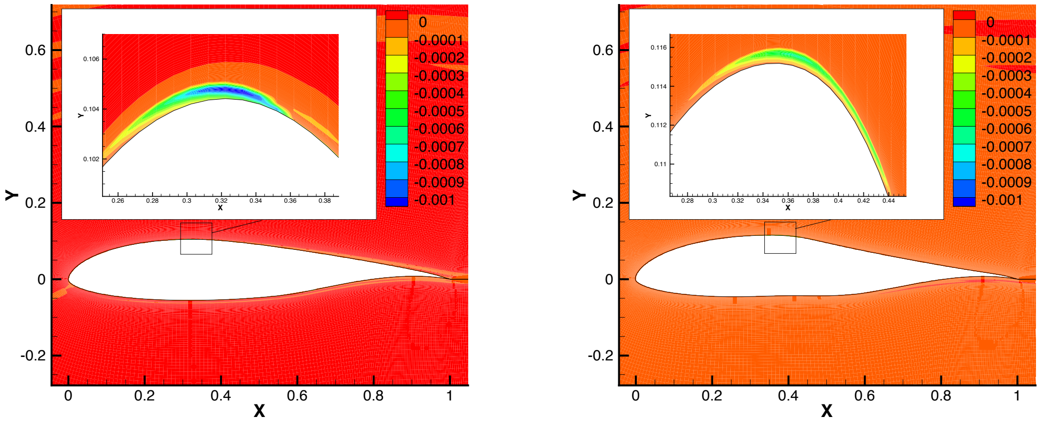

(a) Initial distribution

(b) Final distribution

Figure 6–19: Distribution of adjoint costate of γ for NLF(1)-0416 and optimized airfoils at 5 degrees

Table 6–4: Comparison of the drag coefficients for the NLF(1)-0416 and optimized airfoils at 5° with and without using adjoint variables of the transition and turbulence models to maintain the lift and reduce the drag

Cases	C_d	C_{dp}	C_{df}
NLF(1)-0416	0.0086	0.0032	0.0054
Optimized with the costates	0.0074	0.0029	0.0045
Optimized without the costates	0.0086	0.0032	0.0054

history of the airfoil moment coefficient is demonstrated, and the pitching moment is maintained within 10%.

Figure 6–23 compares the drag coefficients of the initial and optimized airfoils at various angles of attack. The drag coefficients around the angle of attack of 5° where the optimization is performed, are reduced or maintained while at negative and 9° angles of attack an increase is observed. The lift coefficients which are presented in figure 6–24, are almost maintained at all angles of attack. In figure 6–25 the

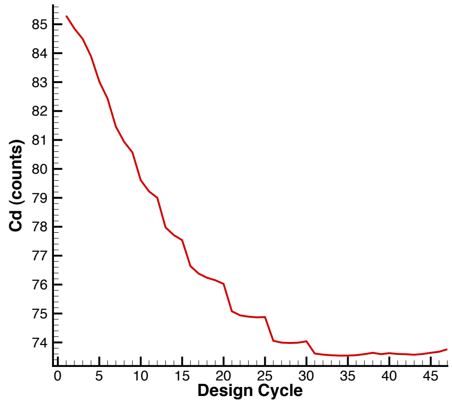

Figure 6–20: Drag Coefficient History at 5°

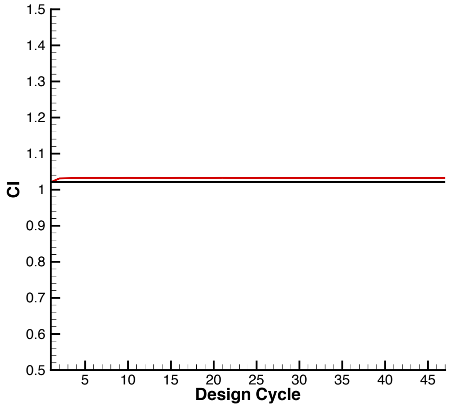

Figure 6–21: Lift Coefficient History at 5°

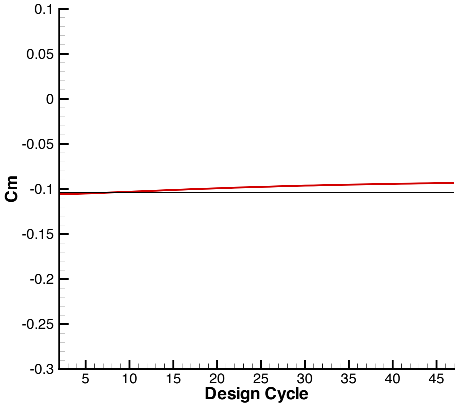

Figure 6–22: Moment Coefficient History at 5°

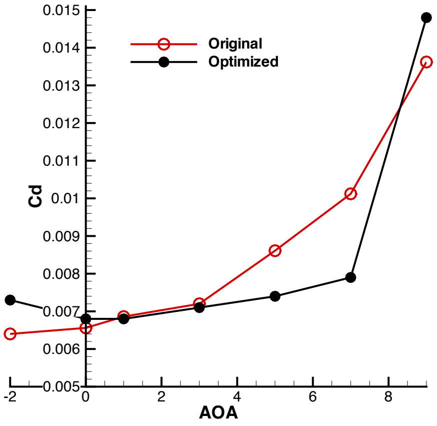

Figure 6–23: Drag coefficient versus angle of attack for the initial and optimized airfoil at 5°

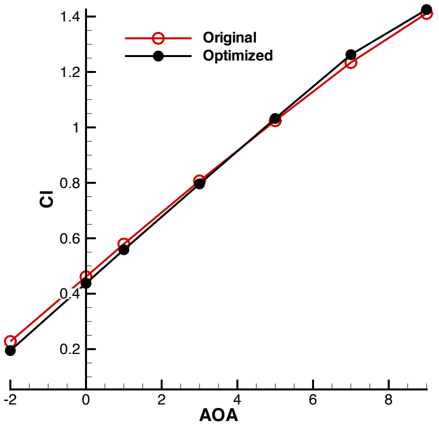

Figure 6–24: Lift coefficient versus angle of attack for the initial and optimized airfoil at 5°

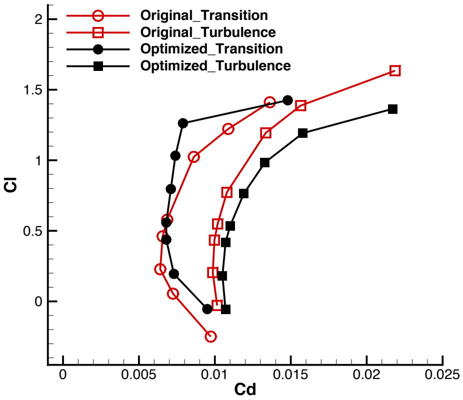

Figure 6–25: Drag polar for the optimized and NLF(1)-0416 airfoils at 5°

drag polars for the initial and optimized airfoils are shown in transitional and fully turbulent regimes. As expected since the airfoil was designed at a single design point, the largest drag reduction compared to the original airfoil is observed at an angle of attack of 5 degrees. However, for values in the vicinity of five degrees, marginal improvement is realized, with an adverse effect at lower and higher lift coefficients. The optimized airfoil in fully turbulent flow produces slightly higher drag coefficients at all angles of attack when compared to the initial airfoil. This demonstrates the importance of including the performance of NLF airfoils in fully turbulent flow as part of the design process and will be explored as part of our future work.

To ensure that the grid used in the optimization process is sufficient, a new mesh with a lower y^+ is employed for the optimized airfoil. Table 6–5 compares the obtained results from the two grids. As the y^+ decreases the pressure and skin

Table 6–5: Effect of y^+ on the lift and drag coefficients of the optimized airfoil at 5°

Y^+	C_d	C_{dp}	C_{df}
0.1	0.0074	0.0029	0.0045
0.075	0.0072	0.0028	0.0044

friction drag coefficients are within a single drag count. This illustrates that the final results from the optimization procedure are independent of the grid.

6.4 S809 Wind Turbine Profile at 9 Degrees; Minimize Drag, while Maintain C_l

To demonstrate the capability of the optimizer to minimize the pressure drag in addition to the skin friction component, the S809 airfoil is employed as the initial airfoil geometry. The angle of attack and Reynolds number are chosen to be 9 degrees and 2×10^6 respectively. At this angle, the presence of a turbulent separation bubble spanning 5% of the chord length at the trailing edge, ensures that the pressure drag is the dominant component of the total drag. Figure 6–26 compares the initial and optimized airfoil shapes. The surface curvature and camber line change to reduce the size of the turbulent separation bubble in addition to maintaining the favourable pressure gradient as much as possible to postpone the onset of transition. In figure 6–27, a comparison between the initial and final pressure distributions are presented. For the initial S809 wind turbine profile the pressure peaks are at the leading edge and transition occurs at the 3% chord location on the upper surface and 54% on the lower surface. After optimization the pressure peak decreases and the favourable pressure gradient over the upper surface extends.

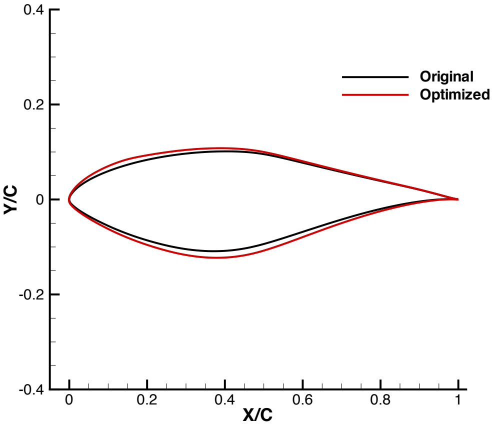

Figure 6–26: Shape modifications of the S809 airfoil at 9°; maintaining lift and reducing drag

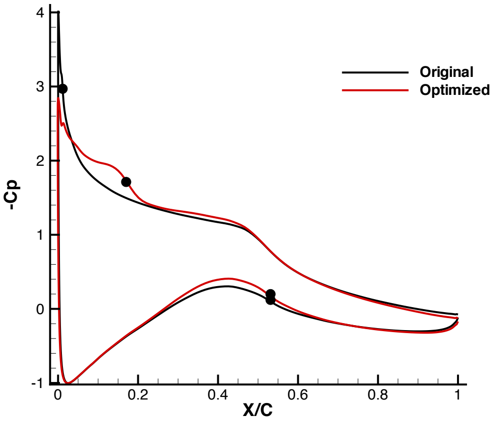

Figure 6–27: Distribution of pressure coefficient of the S809 airfoil at 9°; maintaining lift and reducing drag

In figures 6–28 and 6–29 the distributions of the skin friction coefficients before and after optimization are compared for the upper and lower airfoil surfaces respectively. The negative values of the skin friction coefficients near the trailing edge over the upper surface show the presence of a turbulent separation bubble near the trailing edge. After optimization the size of the fully turbulent separation region is reduced; as a result, the pressure drag component decreases. In addition, the upper transition point is shifted towards the airfoil trailing edge to reduce the skin friction component of the total drag by extending the laminar flow over the airfoil.

In figure 6–30 the velocity profiles at two chord-wise locations near the trailing edge are compared for the initial and optimized airfoils. The negative velocity of the initial profile shows the presence of a fully turbulent separation region at the trailing edge. After optimization the velocity profiles are less negative, showing that the size

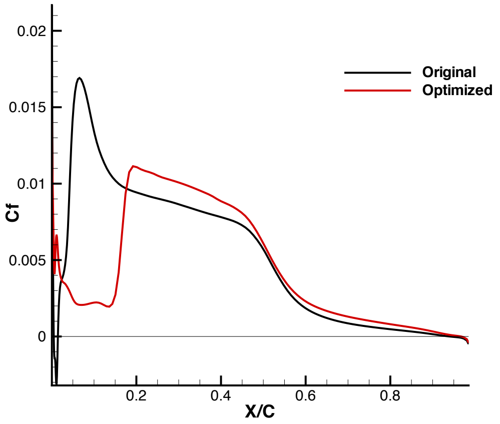

Figure 6–28: Distribution of skin friction coefficient for the upper surface of the S809 airfoil at 9°; maintaining lift and reducing drag

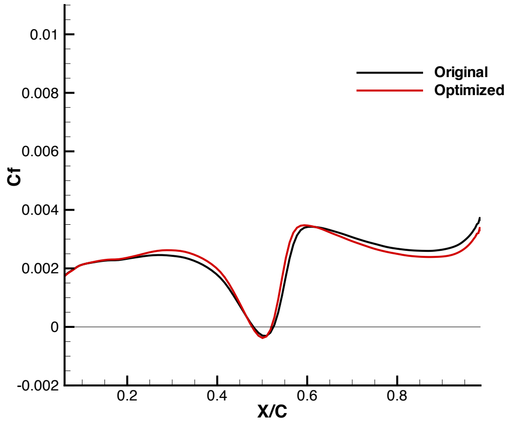

Figure 6–29: Distribution of skin friction coefficient for the lower surface of the S809 airfoil at 9°; maintaining lift and reducing drag

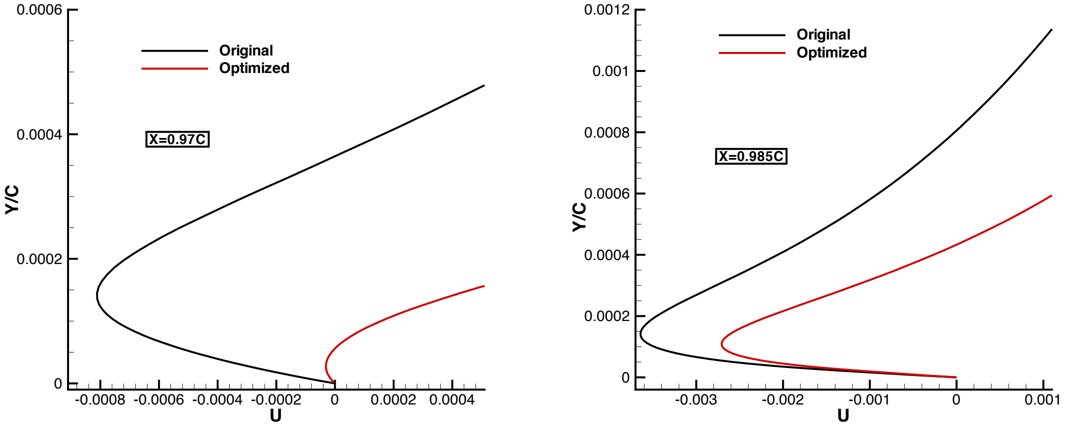

(a) At 97% of chord length

(b) At 98.5% of chord length

Figure 6–30: Velocity profiles at two chord-wise locations over the upper surface of the S809 and optimized airfoils at 9°

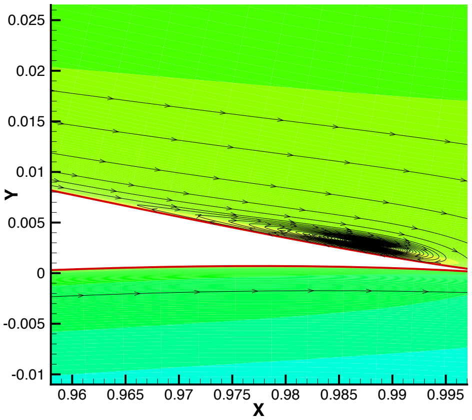

Figure 6–31: Turbulent separated region for the S809 airfoil at 9°

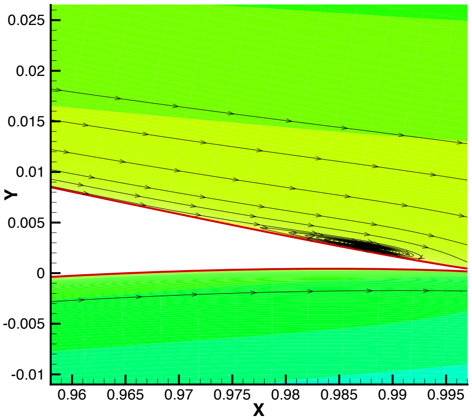

Figure 6–32: Turbulent separated region for the optimized airfoil at 9°

and intensity of the trailing edge separation region has decreased. In figure 6–31 streamlines near the trailing edge are employed to show the fully turbulent region near the trailing edge of the S809 wind turbine profile. The streamlines in figure 6–32 demonstrate that after optimization the size of the fully turbulent separated region decreases. This fully turbulent separation bubble with a smaller length and thickness reduces the pressure component of the total drag.

Table 6–6: Comparison of the drag coefficients for the S809 and optimized airfoils at 9° with using adjoint variables of the transition and turbulence models to maintain the lift and reduce the drag

Cases	C_d	C_{dp}	C_{df}
S809 Airfoil	0.0185	0.0114	0.0071
Optimized	0.0152	0.0089	0.0063

Figure 6–33 shows that the initial lift coefficient is well maintained during the optimization process while the pitching moment remains around -0.04. As presented

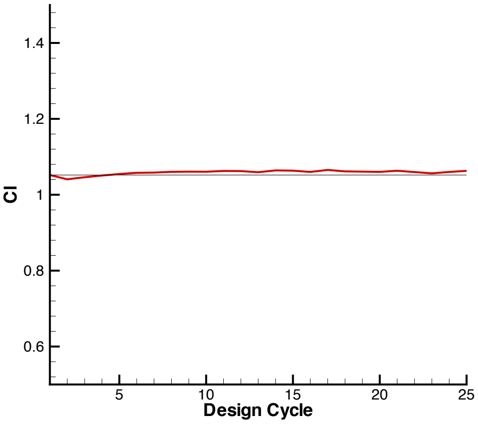

Figure 6–33: Lift Coefficient History at 9°

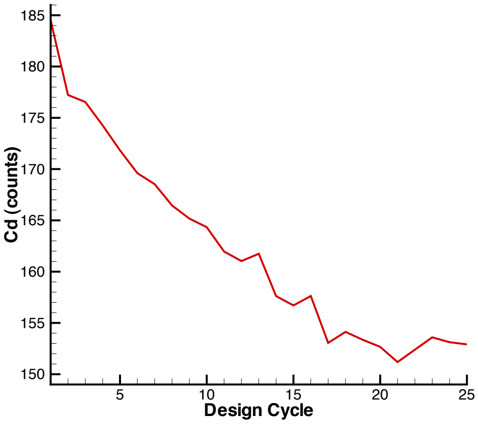

Figure 6–34: Drag Coefficient History at 9°

in table 6–6, the total drag is reduced by 33 counts where 25 drag counts are related to the pressure component and the skin friction drag decreases by 8 counts. Figure 6–34 illustrates the total drag reduction history during the optimization process.

6.5 NLF(1)-0416 Airfoil at 5 Degrees; Maximize Lift-to-Drag Ratio

In this subsection, we investigate a new objective function, where the lift-to-drag ratio is to be maximized with respect to the airfoil geometry and subject to a thickness constraint. The design is performed at the same Reynolds number of 2×10^6 at an angle of attack of 5 degrees. To achieve high lift-to-drag ratios we employed the same objective functions as that applied in the previous cases; however, here we specified a target lift coefficient instead of using the lift of the original airfoil. In this manner we were able to reuse the same adjoint boundary conditions. Similar to the former cases, the chordwise thickness distribution was maintained within 10%

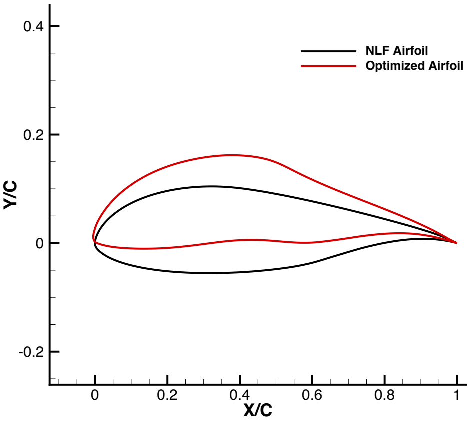

Figure 6–35: Shape modifications of NLF(1)-0416 airfoil; maximizing lift and reducing drag

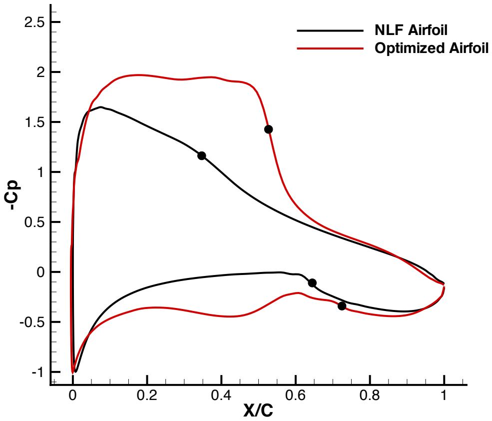

Figure 6–36: Distribution of pressure coefficient of NLF(1)-0416 airfoil; maximizing lift and reducing drag

of the original value. This test case, is identical to the second case presented in subsection 6.3, except that here a higher target lift coefficient is specified.

Figure 6–35 demonstrates the final airfoil geometry, where an extreme redesign of the initial geometry is observed. The airfoil camber has increased considerably, in the forward portion, while the aft portion experiences the same but enhanced reflex camber seen earlier. To ensure a low drag profile as well as to maintain the initial thickness distribution, the lower surface undergoes an equal amount of modification. Note that at the 60% chord location, the lower surface experiences a shift in the local surface slope. As the upper surface curvature abruptly changes at this location, the constraint to maintain the thickness distribution as well as the objective to lower the skin friction drag results in the observed lower surface geometry. Figure 6–36 illustrates the pressure distribution of the final geometry, where a large favourable

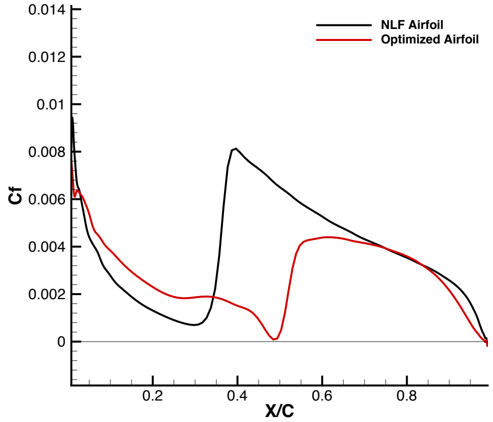

Figure 6–37: Distribution of skin friction coefficient for the upper surface of NLF(1)-0416 airfoil; maximizing lift and reducing drag

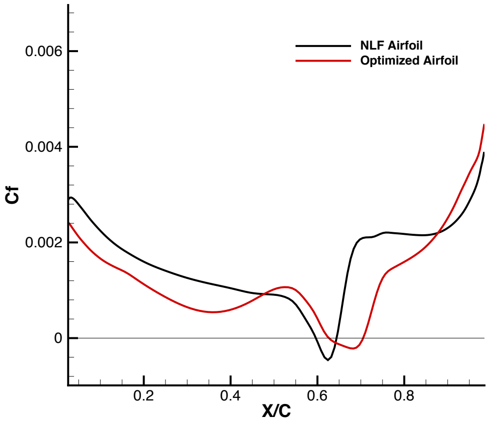

Figure 6–38: Distribution of skin friction coefficient for the lower surface of NLF(1)-0416 airfoil; maximizing lift and reducing drag

pressure gradient region with a laminar roof-top pressure profile has been achieved, thus shifting the transition point aft, while producing a Stratford-type pressure recovery in the aft portion of the airfoil to recover the freestream pressure without any trailing edge separation. This has allowed the optimized airfoil to increase the lift coefficient by 50% with a 5 drag count decrease of the total drag coefficient due to 12 counts decrease of the skin friction component and 7 counts pressure drag increase as listed in table 6–7. In figures 6–37 and 6–38 the distributions of skin friction coefficients are respectively presented for the upper and lower surfaces. The point of transition for the upper surface moves towards the trailing edge and accelerates the laminar boundary layer to postpone the boundary layer instability. The extension of the laminar flow over the airfoil increases and the skin friction drag is reduced.

Table 6–7: Comparison of the lift-to-drag ratio and drag coefficients for the NLF(1)-0416 and optimized airfoils to maximize the lift-to-drag ratio

Cases	$\frac{C_l}{C_d}$	C_l	C_d	C_{dp}	C_{df}
NLF(1)-0416	118.7	1.02	0.0086	0.0032	0.0054
Optimized Airfoil	185.2	1.500	0.0081	0.0039	0.0042
Optimized Airfoil	185.8	1.802	0.0097	0.0052	0.0045
Optimized Airfoil	180.9	1.881	0.0104	0.0059	0.0045

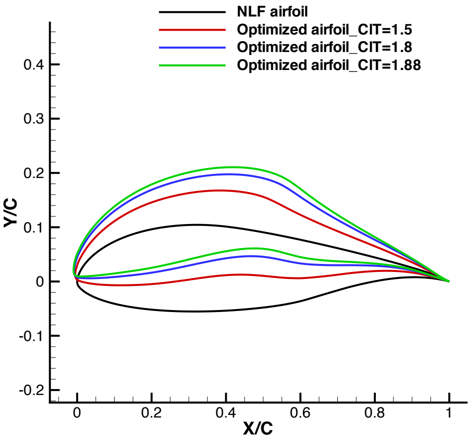

Figure 6–39: Shape modifications of NLF(1)-0416 and the optimized airfoils at 5°; maximizing lift and reducing drag

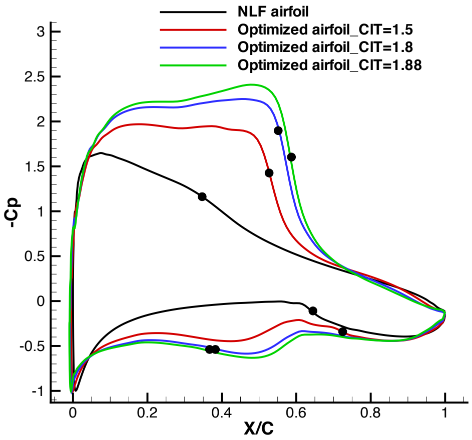

Figure 6–40: Distribution of pressure coefficient of NLF(1)-0416 the optimized airfoils at 5°; maximizing lift and reducing drag

To challenge the optimizer to achieve higher lift-to-drag ratios, we incrementally increased the lift coefficient. Figure 6–39 shows that as the lift coefficient increases the airfoil shape changes in a manner to increase the camber and as a result the minimum pressure peak decreases as shown in figure 6–40. To postpone the onset of transition over the upper surface the optimizer extends the favourable pressure gradient and maintains the achieved minimum pressure peak as much as possible. As the curvature of the airfoil increases the pressure difference between the aft and front of the airfoil increases and consequently the pressure component of the drag increases.

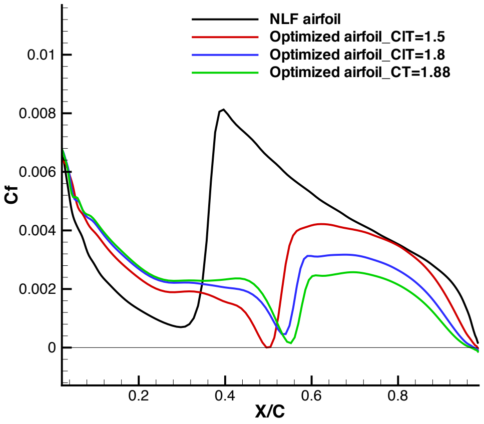

Figure 6–41: Distribution of skin friction coefficient for the upper surface of NLF(1)-0416 the optimized airfoils at 5°; maximizing lift and reducing drag

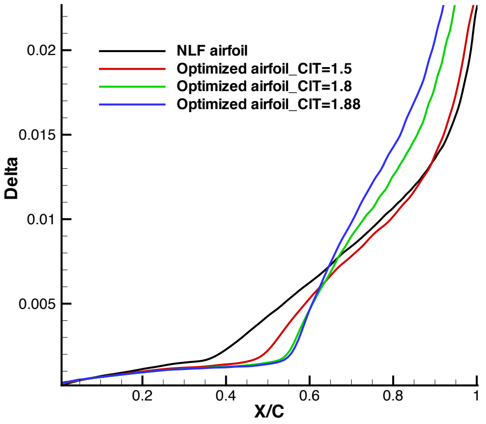

Figure 6–42: Boundary layer thickness over the upper surface of the initial and optimized airfoils at 5°; maximizing lift and reducing drag

As the lift coefficient increases, the upper transition point is delayed due to the extension of the favourable pressure gradient over the upper surface (figure 6–41). The lower transition point stays at its initial location until the airfoil camber changes in a fashion that the favourable pressure gradient can not be maintained and the lower transition point is shifted towards the leading edge. After achieving the maximum lift-to-drag ratio, as the lift increases the total drag increases and the ratio is reduced. At a target lift coefficient of 1.93, the flow over the upper surface separates due to the high airfoil camber and the lift is reduced while the pressure drag drastically increases.

Figure 6–42 illustrates the boundary layer thickness over the upper surface of the initial and optimized airfoils. The extension of the thin laminar boundary layer over the forward portion of the airfoil increases since the transition point is postponed. As the lift coefficient of the optimized airfoils increases the thickness of the fully turbulent boundary layer increases until a lift coefficient of 1.93 where the boundary layer separates and the lift coefficient decreases. The velocity distributions around the initial and optimized airfoils are shown in figure 6–43. As the lift coefficient increases the laminar boundary layer is stabilized and the flow accelerates; as a result, the point of transition shifts towards the airfoil trailing edge.

Table 6–8: Effect of y^+ on the lift and drag coefficients of the optimized airfoil at 5°; maximizing lift-to-drag ratio

Y^+	$\frac{C_l}{C_d}$	C_l	C_d	C_{dp}	C_{df}
0.1	180.9	1.881	0.0104	0.0059	0.0045
0.075	182.4	1.879	0.0103	0.0060	0.0043

A y^+ study, shown in table 6–8, confirms the reductions observed in the final drag coefficients and the final lift coefficient is within 0.002.

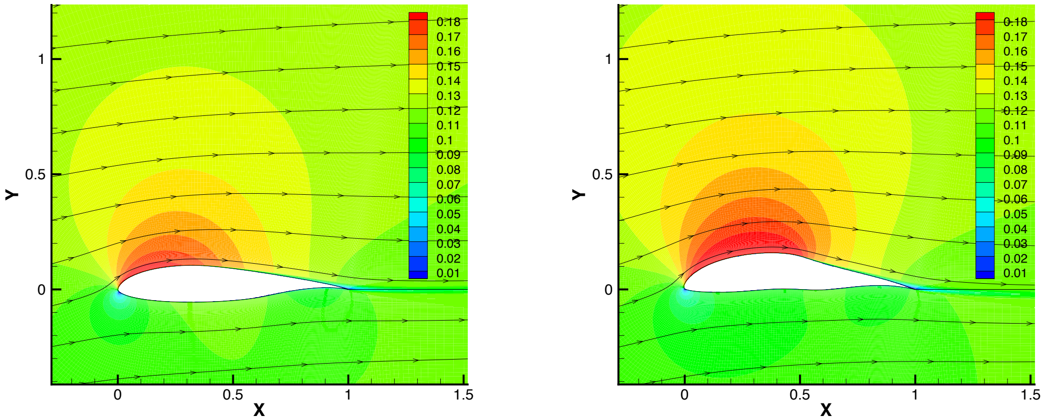

(a) NLF(1)-0416 airfoil (b) Optimized airfoil with $C_l = 1.5$

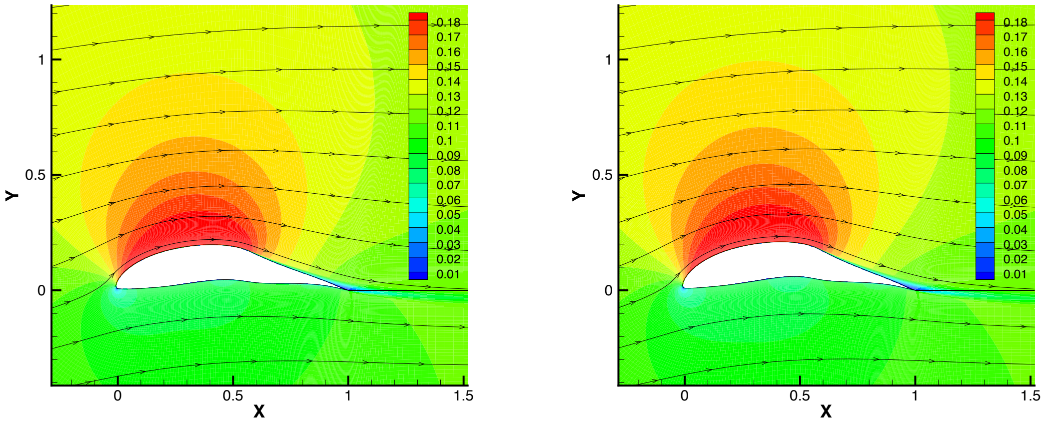

(c) Optimized airfoil with $C_l = 1.8$ (d) Optimized airfoil with $C_l = 1.88$

Figure 6–43: Velocity distributions around the NLF(1)-0416 and optimized airfoils at 5°

CHAPTER 7
Conclusion

A laminar-turbulent flow solver has been developed by employing the $\gamma - \tilde{Re}_{\theta t}$ transition model combined with the $k - \omega$ SST turbulence model. The discrete adjoint equations for the transition and turbulence models are derived and added to the adjoint-based optimization framework of a RANS solver. The new design and optimization framework has been employed to design new natural laminar flow airfoils. The first section summarizes the implementation and validation of the transitional flow solver. The second section will briefly explain the discrete adjoint approach for the transition and turbulence models and review the obtained results. In the final section potential future works are described.

7.1 Development and Validation of the Laminar-Turbulent Flow Solver

The $\gamma - \tilde{Re}_{\theta}$ transition model is employed in a preconditioned compressible RANS solver using the $k - \omega$ SST turbulence model in order to simulate the transitional flow around two profiles. A grid study demonstrated the importance of sufficient grid points both in the streamwise and normal directions to accurately place the transition location and precisely resolve the turbulent boundary layer. A sequence of numerical test on the NLF(1)-0416 airfoil and the S809 wind turbine profile based on a range of Reynolds numbers and angles of attack, demonstrated that the model was able to simulate both laminar separation bubble and attached boundary layer transitions. Sectional lift, drag, and moment coefficients compared very well against experimental data as well as other numerical results. Drag polars exemplified the effectiveness of the model over fully turbulent simulations. A modified model based on the recalibration of the F_{onset} function, demonstrated improved accuracy in the prediction of the transition point and drag coefficients at equivalent lift coefficients at higher angles of attack and Reynolds numbers. At these flow conditions, an increase in the adverse pressure gradient leads to a moderate increase in the boundary layer shape factor and a subsequent increase in the error between the maximum value of the vorticity Reynolds number and the momentum-thickness Reynolds number. The recalibrated function allowed the laminar boundary layer to develop larger than moderate shape factors, thus extending the laminar region.

7.2 Development of the Optimization Framework for the Design of Natural Laminar Flow Airfoils

The discrete adjoint equations for the $\gamma - \tilde{R}e_{\theta t}$ transition model and the $k - \omega$ SST turbulence model are derived and implemented into the optimization and design framework which is based on the discrete adjoint of the RANS equations. Using these new transition and turbulence adjoint variables with a proper cost function such as the reduction of the turbulent kinetic energy, k, in addition to the drag coefficient improves the capability of the discrete adjoint-based aerodynamic shape optimization approach. Adding the reduction of production of k to the cost function augments the sensitivity of the objective function to perturbations of the turbulence and transition models and increases the influence of the corresponding adjoint variables on the design process. The effectiveness of using the transition and turbulence adjoint equations is shown in the drag minimization of the NLF(1)-0416 airfoil while the lift is maintained at angles of attack of 1° and 5°. The obtained results at 5° show that by excluding the transition and turbulence adjoint variables, the optimizer is unable to reduce the total drag. The reduction of the turbulent kinetic energy decreases the turbulent viscosity and shear stress; as a result, the transition point is postponed and the skin friction drag component is reduced. In both cases the drag polar is compared for the original and optimized airfoils to demonstrate how single point designs affect the airfoil performance at other angles. In order to show the ability of the design framework to reduce pressure drag, the S809 airfoil at 9° is employed to minimize the total drag while the lift is maintained. In this case the optimizer is successful in reducing the size of the turbulent separation region, thereby achieving a greater decrease in the pressure drag. The last case optimized the NLF(1)-0416 airfoil shape to reduce the total drag and maximize the lift. The design framework maintains the favourable pressure gradient and delays the onset of transition in addition to increasing the camber in order to reduce the drag and increase the lift. The obtained results demonstrate the potential of the developed design framework to optimize new natural laminar flow airfoils with lower total drag without sacrificing their performance in laminar-turbulent or fully turbulent flow.

7.3 Future Works

We believe that the present work has paved the way for the $\gamma - \tilde{Re}_{\theta t}$ transition model to be incorporated within a three-dimensional adjoint-based design framework and provides the proper foundation for future works. Some of the potential topics for future research are listed below.

- Propose new correlations for the $\gamma - \tilde{Re}_{\theta t}$ transition model to simulate the laminar-turbulent boundary layers at transonic regimes.

- Modify the transition model and its correlations to model the crossflow instabilities in addition to the streamwise waves for three-dimensional flows.
- Develop a multi-point design framework to optimize airfoils at different angles of attack or Reynolds numbers.
- Include the performance of the designed airfoils in fully turbulent flow as part of the optimization process.
- Extend the two-dimensional design framework to three dimensions and add wing planform parameters such as sweep angle, taper ratio, etc. in addition to the airfoil shape as design variables.

APPENDIX A
Derivation procedure of discrete adjoint equations for the transition and turbulence models

A.1 Formulation of Discrete Adjoint Approaches for the Transition and Turbulence Models

To derive the discrete adjoint equations for the $k-\omega$ SST turbulence model and $\gamma-\tilde{Re}_{\theta t}$ transition model by hand, control theory is applied directly to the variation of the discretized transition and turbulence model equations associated with the variations of their field variables $\left(\delta k, \delta\omega, \delta\gamma, \delta\tilde{Re}_{\theta t}\right)$. In order to show the derivation of the discrete adjoint equations for the $k-\omega$ SST turbulence model and $\gamma-\tilde{Re}_{\theta t}$ transition model, each equation of these models is considered as follows

$$\frac{\partial q_{ij}}{\partial t} = R\left(q_{ij}\right),$$

where q is a turbulence or transition state variable $(k, \omega, \gamma, \tilde{Re}_{\theta t})$, $R(q)$ is the related residual as described in equations (4.3) or (4.4), and i and j denote the cell indices. To derive the discrete adjoint equations for cell (i, j), first a variation of the residual for the cell (i, j) is computed with respect to the variation of the turbulence or transition variable of the computational stencil as follows

$$\begin{aligned}\delta R(q)_{ij} = {} & A^{ij}_{i+1j}\delta q_{i+1j} + A^{ij}_{i-1j}\delta q_{i-1j} + \left(A^{ij}_{ij} + B^{ij}_{ij}\right)\delta q_{ij} \\ & + B^{ij}_{ij+1}\delta q_{ij+1} + B^{ij}_{ij-1}\delta q_{ij-1},\end{aligned}$$

where A and B are the entries of the pentadiagonal matrix for the turbulence and transition models in i- and j-directions respectively. The superscript index shows the computational cell and subscript index indicates the contribution from the neighboring cells of the computational cell. To derive the discrete adjoint equations for the cell (i, j), the contribution of the variation of the turbulence and transition state variable δq_{ij} from the variation of the other residuals are considered for the neighboring cells

$$\begin{aligned}
\delta R_{i+1j}(q) &= \cdots + A_{ij}^{i+1j}\delta q_{ij} + \cdots \\
\delta R_{i-1j}(q) &= \cdots + A_{ij}^{i-1j}\delta q_{ij} + \cdots \\
\delta R_{ij+1}(q) &= \cdots + B_{ij}^{ij+1}\delta q_{ij} + \cdots \\
\delta R_{ij-1}(q) &= \cdots + B_{ij}^{ij-1}\delta q_{ij} + \cdots \quad .
\end{aligned}$$

For each cell the turbulence or transition adjoint vector is multiplied by the variation of the residual of that cell. Then this product is summed over the entire domain as follows

$$\begin{aligned}
\sum_{i\in\Omega}\sum_{j\in\Omega}\delta R_{ij}\psi_{ij} = \cdots &+ R_{i+1j}\psi_{i+1j} + R_{i-1j}\psi_{i-1j} \\
&+ R_{ij}\psi_{ij} + R_{ij+1}\psi_{ij+1} + R_{ij-1}\psi_{ij-1} + \cdots ,
\end{aligned}$$

where i_{max} and j_{max} are the maximum number of nodes in the i- and j-directions respectively. After subsituting the expansion of the variation of the residual with respect to the variation of the state variable δq_{ij}, the terms are collected as follows

$$\begin{aligned}\sum_{i\in\Omega}\sum_{j\in\Omega}\delta R\psi = \cdots + \big[&A^{ij}_{i+1j}\psi_{i+1j} + A^{ij}_{i-1j}\psi_{i-1j} \\ &+ \left(A^{ij}_{ij} + B^{ij}_{ij}\right)\psi_{ij} + B^{ij+1}_{ij}\psi_{ij+1} + B^{ij-1}_{ij}\psi_{ij-1}\big]\,\delta q_{ij} + \cdots \quad .\end{aligned} \tag{A.1}$$

To remove the variation of the state variable δq_{ij} on the gradient, the terms that appear within the brackets in equation (A.1) must sum to zero for each control volume. These terms are then defined as the residual of the discrete adjoint equations for the turbulence and transition models,

$$\begin{aligned}R(\psi) = &A^{ij}_{i+1j}\psi_{i+1j} + A^{ij}_{i-1j}\psi_{i-1j} \\ &+ \left(A^{ij}_{ij} + B^{ij}_{ij}\right)\psi_{ij} + B^{ij}_{ij+1}\psi_{ij+1} + B^{ij}_{ij-1}\psi_{ij-1}.\end{aligned} \tag{A.2}$$

By defining J^D as the entries of the pentadiagonal matrix for the discrete adjoint of the domain cells, the equation A.2 is rearranged as follows

$$J^D_{i+1j}\psi_{i+1j} + J^D_{i-1j}\psi_{i-1j} + J^D_{ij}\psi_{ij} + J^D_{ij+1}\psi_{ij+1} + J^D_{ij-1}\psi_{ij-1} = R(\psi), \tag{A.3}$$

which describes the residual of the discrete adjoint equation for the transition or turbulence variable, q.

APPENDIX B
Continous adjoint approach

B.1 Formulation of Continuous Adjoint Approach for Navier-Stokes Equations

In aerodynamic shape optimization a cost function is optimized with respect to the shape modifications. This cost function is in form of

$$I = \int I_B dB + \int I_D dD,$$

where I_B and I_D are the boundary and flow field cost function contributions which are dependent on the flow variables vector, $\vec{w}$, and surface mesh points, $\vec{x}_s$. The variation of the surface mesh points, $\delta\vec{x}_s$, as the design variables, produces a variation in the flow variable vector, $\delta\vec{w}$; therefore the variation of the cost function can be written as,

$$\delta I = \int \left(\frac{\partial I_B}{\partial \vec{w}} \delta\vec{w} + \frac{\partial I_B}{\partial \vec{x}_s} \delta\vec{x}_s \right) dB + \int \left(\frac{\partial I_D}{\partial \vec{w}} \delta\vec{w} + \frac{\partial I_D}{\partial \vec{x}_s} \delta\vec{x}_s \right) dD.$$

On the other hand in the steady state the variation of flow field equations is described by,

$$\frac{\partial}{\partial \xi_i} \delta \left(\vec{F}_i - \vec{F}_{vi} \right) = \frac{\partial}{\partial \xi_i} \left(\frac{\partial \vec{F}_i}{\partial \vec{w}} \delta\vec{w} + \frac{\partial \vec{F}_i}{\partial \vec{x}_s} \delta\vec{x}_s - \frac{\partial \vec{F}_{vi}}{\partial \vec{w}} \delta\vec{w} - \frac{\partial \vec{F}_{vi}}{\partial \vec{x}_s} \delta\vec{x}_s \right) = 0,$$

where ξ_i is the computational domain coordinates, and $\vec{F}_i$ and $\vec{F}_{v_i}$ are the inviscid and viscous fluxes respectively as defined in subsection 2.5.1. Multiplying by a vector, $\vec{\psi}$, as Lagrange multipliers, and integrating over the field produces

$$\int \vec{\psi}^T \frac{\partial}{\partial \xi_i} \delta \left(\vec{F}_i - \vec{F}_{vi} \right) = 0.$$

Integrating by parts and then subtracting from the perturbed cost function the following equation is obtained

$$\begin{aligned} \delta I = & \int \left\{ \left[\frac{\partial I_B}{\partial \vec{w}} - \vec{\psi}^T \left(\frac{\partial \vec{F}_i}{\partial \vec{w}} - \frac{\partial \vec{F}_{vi}}{\partial \vec{w}} \right) \vec{n}_i \right] \delta \vec{w} + \left[\frac{\partial I_B}{\partial \vec{x}_s} - \vec{\psi}^T \left(\frac{\partial \vec{F}_i}{\partial \vec{x}_s} - \frac{\partial \vec{F}_{vi}}{\partial \vec{x}_s} \right) \vec{n}_i \right] \delta \vec{x}_s \right\} dB \\ & + \int \left\{ \left[\frac{\partial I_D}{\partial \vec{w}} + \frac{\partial \vec{\psi}^T}{\partial \xi_i} \left(\frac{\partial \vec{F}_i}{\partial \vec{w}} - \frac{\partial \vec{F}_{vi}}{\partial \vec{w}} \right) \right] \delta \vec{w} + \left[\frac{\partial I_D}{\partial \vec{x}_s} + \frac{\partial \vec{\psi}^T}{\partial \xi_i} \left(\frac{\partial \vec{F}_i}{\partial \vec{x}_s} - \frac{\partial \vec{F}_{vi}}{\partial \vec{x}_s} \right) \right] \delta \vec{x}_s \right\} dD. \end{aligned} \tag{B.1}$$

The vector $\vec{\psi}$ is computed in such a way that the gradient of the cost function δI is then evaluated from the variation of the surface mesh points, $\delta \vec{x}_s$, without recalculating the variation of the flow variables. The variation of the flow field variables vector, $\delta \vec{w}$, is eliminated from δI (equation B.1) by solving the adjoint equation for $\vec{\psi}$ as,

$$\frac{\partial I_D}{\partial \vec{w}} + \frac{\partial \vec{\psi}^T}{\partial \xi_i} \left(\frac{\partial \vec{F}_i}{\partial \vec{w}} - \frac{\partial \vec{F}_{vi}}{\partial \vec{w}} \right) = 0, \tag{B.2}$$

and considering the following equation as its boundary condition

$$\vec{\psi}^T \left(\frac{\partial \vec{F}_i}{\partial \vec{w}} - \frac{\partial \vec{F}_{vi}}{\partial \vec{w}} \right) \vec{n}_i = \frac{\partial I_B}{\partial \vec{w}}. \tag{B.3}$$

The continuous adjoint equation (equation B.2) and the corresponding boundary condition (equation B.3) are discretized over the domain and numerically solved. The remaining terms which are dependent on the variation of the surface mesh points, $\delta \vec{x}_s$, define the gradient of the cost function that can be used in a gradient-based optimization approach to improve the design [44].

B.2 Formulation of Continuous Adjoint Equations for the Turbulence and Transition Models

Multiplying the four new costates $(\psi_5, \psi_6, \psi_7, \psi_8)$ to the variation of the turbulence and transition equations associated with the variation of primitive field variables $\left(\delta k, \delta\omega, \delta\gamma, \delta\tilde{Re}_{\theta t}\right)$ and integrating by parts over the entire domain, the continuous adjoint equations of the $k-\omega$ SST turbulence and $\gamma-\tilde{Re}_{\theta t}$ transition models are derived

$$
\begin{aligned}
&\int\left\{\frac{\partial^2}{\partial x_i^2}\left[\left(\mu+\sigma_{k1}\mu_t\right)\psi_5\right]+\frac{\partial}{\partial x_i}\left(\psi_5\rho u_i\right)-2\frac{\partial}{\partial x_i}\left[(1-F_1)\frac{\rho\sigma_{\omega 2}}{\omega}\frac{\partial\omega}{\partial x_i}\psi_5\right]+\psi_5\rho\omega\beta^*\right\}dD=0,\\
&\int\left\{\frac{\partial^2}{\partial x_i^2}\left[\left(\mu+\sigma_{\omega 1}\mu_t\right)\psi_6\right]+\frac{\partial}{\partial x_i}\left(\psi_6\rho u_i\right)-2\frac{\partial}{\partial x_i}\left[(1-F_1)\frac{\rho\sigma_{\omega 2}}{\omega}\frac{\partial k}{\partial x_i}\psi_6\right]\right.\\
&\qquad\left.+\psi_6\left[\beta^*\rho k+2\beta_1\rho\omega-2(1-F_1)\frac{\rho\sigma_{\omega 2}}{\omega^2}\frac{\partial\omega}{\partial x_i}\frac{\partial k}{\partial x_i}\right]\right\}dD=0,\\
&\int\left\{\frac{\partial^2}{\partial x_i^2}\left[\left(\mu+\frac{\mu_t}{\sigma_f}\right)\psi_7\right]+\frac{\partial}{\partial x_i}\left(\psi_7\rho u_i\right)+\psi_7F_{\text{length}}c_{a1}\rho SF_{\text{onset}}{}^{0.5}\left(\frac{0.5}{\sqrt{\gamma}}-1.5c_{e1}\sqrt{\gamma}\right)\right.\\
&\qquad\left.+\psi_7c_{a2}\rho\Omega\gamma F_{\text{turb}}\left(2c_{e2}\gamma-1\right)\right\}dD=0,\\
&\int\left\{\frac{\partial^2}{\partial x_i^2}\left[\sigma_\theta\left(\mu+\mu_t\right)\psi_8\right]+\frac{\partial}{\partial x_i}\left(\psi_8\rho u_i\right)-\psi_8c_{\theta t}\frac{(\rho U)^2}{500\mu}(1-F_{\theta t})\right\}dD=0.
\end{aligned}
\tag{B.4}
$$

and their corresponding adjoint boundary conditions are

$$
\begin{aligned}
&\int n_i\left\{\psi_5\left[\left(\mu+\sigma_{k1}\mu_t\right)\frac{\partial\delta k}{\partial x_i}-\rho u_i\delta k+2(1-F_1)\frac{\rho\sigma_{\omega 2}}{\omega}\frac{\partial\omega}{\partial x_i}\delta k\right]-\frac{\partial\psi_5}{\partial x_i}\left(\mu+\sigma_{k1}\mu_t\right)\delta k\right\}dB=0,\\
&\int n_i\left\{\psi_6\left[\left(\mu+\sigma_{\omega 1}\mu_t\right)\frac{\partial\delta\omega}{\partial x_i}-\rho u_i\delta\omega+2(1-F_1)\frac{\rho\sigma_{\omega 2}}{\omega}\frac{\partial k}{\partial x_i}\delta\omega\right]-\frac{\partial\psi_6}{\partial x_i}\left(\mu+\sigma_{\omega 1}\mu_t\right)\delta\omega\right\}dB=0,
\end{aligned}
$$

$$
\begin{aligned}
&\int n_i\left\{\psi_7\left[\left(\mu+\frac{\mu_t}{\sigma_f}\right)\frac{\partial\delta k}{\partial x_i}-\rho u_i\delta\gamma\right]-\frac{\partial\psi_7}{\partial x_i}\left(\mu+\frac{\mu_t}{\sigma_f}\right)\delta\gamma\right\}dB=0,\\
&\int n_i\left\{\psi_8\left[\sigma_\theta\left(\mu+\mu_t\right)\frac{\partial\delta\omega}{\partial x_i}-\rho u_i\delta\tilde{Re}_{\theta t}\right]-\frac{\partial\psi_8}{\partial x_i}\sigma_\theta\left(\mu+\mu_t\right)\delta\tilde{Re}_{\theta t}\right\}dB=0.
\end{aligned}
\tag{B.5}
$$

The variation of the field variables are not eliminated since each type of boundary has its own special treatment which is dependent on its related turbulence and transition models boundary conditions. The objective function may include boundary contribution, domain contribution, or both depending on its definition. According to the continuous adjoint theory the derivatives of the boundary contributions of the cost function with respect to the corresponding field variables are added to the right hand side of the equation (B.5) and the similar derivatives of the domain terms are used as the source terms for the equation (B.4).

B.2.1 Continuous adjoint boundary conditions

The equation (B.5) is simplified based on the boundary conditions of the turbulence and transition models in order to derive the continuous adjoint boundary conditions.

- Inlet boundary

  The variation of the state variables on this boundary is zero $\left(\delta k = \delta\omega = \delta\gamma = \delta\tilde{R}e_{\theta t} = 0.\right)$. Regarding to this definition, the continuous adjoint boundary conditions are written as follows

  $$\int \left(\mu + \sigma_{k1}\mu_t\right)\frac{\partial \psi_5}{\partial x_i} n_i dB = 0, \qquad \int \left(\mu + \sigma_{\omega 1}\mu_t\right)\frac{\partial \psi_6}{\partial x_i} n_i dB = 0,$$
  $$\int \left(\mu + \frac{\mu_t}{\sigma_f}\right)\frac{\partial \psi_7}{\partial x_i} n_i dB = 0, \qquad \int \sigma_\theta\left(\mu + \mu_t\right)\frac{\partial \psi_8}{\partial x_i} n_i dB = 0.$$

  This implies that the gradient of the costate variables normal to the inlet boundary must be zero.

  $$\frac{\partial \psi_5}{\partial \eta} = \frac{\partial \psi_6}{\partial \eta} = \frac{\partial \psi_7}{\partial \eta} = \frac{\partial \psi_8}{\partial \eta} = 0.$$

- Outlet boundary

  According to the equation (B.5), the continuous adjoint boundary conditions for the turbulence and transition models at the outlet are described as follows

$$\int n_i \left\{ \psi_5 \left[-\rho u_i + 2(1-F_1)\frac{\rho\sigma_{\omega 2}}{\omega}\frac{\partial \omega}{\partial x_i} \right] - \frac{\partial \psi_5}{\partial x_i}\left(\mu + \sigma_{k1}\mu_t\right) \right\} dB = 0,$$

$$\int n_i \left\{ \psi_6 \left[-\rho u_i + 2(1-F_1)\frac{\rho\sigma_{\omega 2}}{\omega}\frac{\partial k}{\partial x_i} \right] - \frac{\partial \psi_6}{\partial x_i}\left(\mu + \sigma_{\omega 1}\mu_t\right) \right\} dB = 0.$$

$$\int n_i \left\{ -\psi_7 \rho u_i - \frac{\partial \psi_7}{\partial x_i}\left(\mu + \frac{\mu_t}{\sigma_f}\right) \right\} dB = 0,$$

$$\int n_i \left\{ -\psi_8 \rho u_i - \frac{\partial \psi_8}{\partial x_i}\sigma_\theta\left(\mu + \mu_t\right) \right\} dB = 0.$$

- Wall boundary

  Applying the wall boundary conditions into the continuous adjoint approach (equation B.5) leads to the following adjoint boundary equations for the $k-\omega$ SST turbulence model and the $\gamma - \tilde{Re}_{\theta t}$ transition model.

$$\int \left(\mu + \sigma_{k1}\mu_t\right)\frac{\partial \psi_5}{\partial x_i} n_i dB = 0,$$

$$\int \left(\mu + \sigma_{\omega 1}\mu_t\right)\frac{\partial \psi_6}{\partial x_i} n_i dB = 0,$$

$$\int n_i \left\{ -\psi_7 \rho u_i - \frac{\partial \psi_7}{\partial x_i}\left(\mu + \frac{\mu_t}{\sigma_f}\right) \right\} dB = 0,$$

$$\int n_i \left\{ -\psi_8 \rho u_i - \frac{\partial \psi_8}{\partial x_i}\sigma_\theta\left(\mu + \mu_t\right) \right\} dB = 0.$$

B.2.2 Recovery of the continuous adjoint equations for the turbulence and transition models from the discrete equations

To show the consistency of the discrete adjoint equations for the $\gamma - \tilde{Re}_{\theta t}$ transition and $k-\omega$ SST turbulence models, the discrete adjoint equations for the models approach the continuous ones when Δx_i and Δx_j approach zero. In the i-direction the discrete adjoint equations for the $\gamma - \tilde{R}e_{\theta t}$ transition model and $k - \omega$ SST turbulence model are re-written in the following form

$$\begin{aligned}
&(1 - F_{1,i-1j})\,\frac{\rho_{i-1j}\sigma_{\omega 2}}{\omega_{i-1j}}\frac{\omega_{ij} - \omega_{i-2j}}{2\Delta x_{i-1}^2}\psi_{5,i-1j} - (1 - F_{1,i+1j})\,\frac{\rho_{i+1j}\sigma_{\omega 2}}{\omega_{i+1j}}\frac{\omega_{i+2j} - \omega_{ij}}{2\Delta x_{i+1}^2}\psi_{5,i+1j} \\
&- \rho_{i-1j}\frac{u_{i-1}^{-}}{\Delta x_{i-1}}\psi_{5,i-1j} - \rho_{ij}\frac{u_i^{+} - u_i^{-}}{\Delta x_i}\psi_{5,ij} + \rho_{i+1j}\frac{u_{i+1}^{+}}{\Delta x_{i+1}}\psi_{5,i+1j} \\
&\frac{1}{\Delta x_{i-1}}\left(\frac{\mu + \sigma_{k1}\mu_t}{\Delta x}\right)_{i-\frac{1}{2}}\psi_{5,i-1j} + \frac{1}{\Delta x_{i+1}}\left(\frac{\mu + \sigma_{k1}\mu_t}{\Delta x}\right)_{i+\frac{1}{2}}\psi_{5,i+1j} \\
&- \frac{1}{\Delta x_i}\left[\left(\frac{\mu + \sigma_{k1}\mu_t}{\Delta x}\right)_{i+\frac{1}{2}} + \left(\frac{\mu + \sigma_{k1}\mu_t}{\Delta x}\right)_{i-\frac{1}{2}}\right]\psi_{5,ij} + \beta^{*}\rho_{ij}\omega_{ij}\psi_{5,ij} = 0,
\end{aligned}$$

$$\begin{aligned}
&(1 - F_{1,i-1j})\,\frac{\rho_{i-1j}\sigma_{\omega 2}}{\omega_{i-1j}}\frac{k_{ij} - k_{i-2j}}{2\Delta x_{i-1}^2}\psi_{6,i-1j} - (1 - F_{1,i+1j})\,\frac{\rho_{i+1j}\sigma_{\omega 2}}{\omega_{i+1j}}\frac{k_{i+2j} - k_{ij}}{2\Delta x_{i+1}^2}\psi_{6,i+1j} \\
&- \rho_{i-1j}\frac{u_{i-1}^{-}}{\Delta x_{i-1}}\psi_{6,i-1j} - \rho_{ij}\frac{u_i^{+} - u_i^{-}}{\Delta x_i}\psi_{6,ij} + \rho_{i+1j}\frac{u_{i+1}^{+}}{\Delta x_{i+1}}\psi_{6,i+1j} \\
&+ \frac{1}{\Delta x_{i-1}}\left(\frac{\mu + \sigma_{\omega 1}\mu_t}{\Delta x}\right)_{i-\frac{1}{2}}\psi_{6,i-1j} - \frac{1}{\Delta x_{i+1}}\left(\frac{\mu + \sigma_{\omega 1}\mu_t}{\Delta x}\right)_{i+\frac{1}{2}}\psi_{6,i+1j} \\
&+ \frac{1}{\Delta x_i}\left[\left(\frac{\mu + \sigma_{\omega 1}\mu_t}{\Delta x}\right)_{i+\frac{1}{2}} + \left(\frac{\mu + \sigma_{\omega 1}\mu_t}{\Delta x}\right)_{i-\frac{1}{2}}\right]\psi_{6,ij} \\
&+ \left[\beta^{*}\rho_{ij}k_{ij} + 2\beta\rho_{ij}\omega_{ij} + (1 - F_{1,ij})\,\frac{\rho_{ij}\sigma_{\omega 2}}{\omega_{ij}^2}\frac{k_{i+1j} - k_{i-1j}}{\Delta x_i}\frac{\omega_{i+1j} - \omega_{i-1j}}{\Delta x_i}\right]\psi_{6,ij} = 0,
\end{aligned}$$

$$
\begin{aligned}
&F_{\text{length}} c_{a1}\rho S F_{\text{onset}}^{0.5}\left(\frac{1}{\sqrt{\gamma}} - c_{e1}\sqrt{\gamma}\right)\psi_{7,ij} - c_{a2}\rho\Omega F_{\text{turb}}\left(2c_{e2}\gamma - 1\right)\psi_{7,ij} \\
&- \rho_{i-1j}\frac{u_{i-1}^{-}}{\Delta x_{i-1}}\psi_{7,i-1j} - \rho_{ij}\frac{u_i^{+} - u_i^{-}}{\Delta x_i}\psi_{7,ij} + \rho_{i+1j}\frac{u_{i+1}^{+}}{\Delta x_{i+1}}\psi_{7,i+1j} \\
&+ \frac{1}{\Delta x_{i-1}}\left(\frac{\mu + \sigma_{k1}\mu_t}{\Delta x}\right)_{i-\frac{1}{2}}\psi_{7,i-1j} + \frac{1}{\Delta x_{i+1}}\left(\frac{\mu + \sigma_{k1}\mu_t}{\Delta x}\right)_{i+\frac{1}{2}}\psi_{7,i+1j} \\
&- \frac{1}{\Delta x_i}\left[\left(\frac{\mu + \sigma_{k1}\mu_t}{\Delta x}\right)_{i+\frac{1}{2}} + \left(\frac{\mu + \sigma_{k1}\mu_t}{\Delta x}\right)_{i-\frac{1}{2}}\right]\psi_{7,ij} = 0,
\end{aligned}
$$

and

$$
\begin{aligned}
&- \rho_{i-1j}\frac{u_{i-1}^{-}}{\Delta x_{i-1}}\psi_{8,i-1j} - \rho_{ij}\frac{u_i^{+} - u_i^{-}}{\Delta x_i}\psi_{8,ij} + \rho_{i+1j}\frac{u_{i+1}^{+}}{\Delta x_{i+1}}\psi_{8,i+1j} \\
&+ \frac{1}{\Delta x_{i-1}}\left(\frac{\mu + \sigma_{\omega 1}\mu_t}{\Delta x}\right)_{i-\frac{1}{2}}\psi_{8,i-1j} - \frac{1}{\Delta x_{i+1}}\left(\frac{\mu + \sigma_{\omega 1}\mu_t}{\Delta x}\right)_{i+\frac{1}{2}}\psi_{8,i+1j} \\
&+ \frac{1}{\Delta x_i}\left[\left(\frac{\mu + \sigma_{\omega 1}\mu_t}{\Delta x}\right)_{i+\frac{1}{2}} + \left(\frac{\mu + \sigma_{\omega 1}\mu_t}{\Delta x}\right)_{i-\frac{1}{2}}\right]\psi_{8,ij} - c_{\theta t}\frac{(\rho U)^2}{500\mu}(1 - F_{\theta t})\psi_{8,ij} = 0.
\end{aligned}
$$

When Δx_i approaches zero, by applying the definitions of u_i^{-} and u_i^{+} (equation 4.7), and considering the first- and second-derivatives [6] the following relations are produced

$$
\begin{aligned}
&\beta^{*}\rho\omega\psi_5 - 2\frac{\partial}{\partial x_j}\left[(1 - F_1)\frac{\rho\sigma_{\omega 2}}{\omega}\frac{\partial \omega}{\partial x_j}\psi_5\right] + \frac{\partial}{\partial x_i}\left(\psi_5\rho u_i\right) + \frac{\partial^2}{\partial x_i^2}\left[\left(\mu + \sigma_{k1}\mu_t\right)\psi_5\right] = 0, \\
&\left[\beta^{*}\rho k + 2\beta_1\rho\omega - 2(1 - F_1)\frac{\rho\sigma_{\omega 2}}{\omega^2}\frac{\partial \omega}{\partial x_i}\frac{\partial k}{\partial x_i}\right]\psi_6 - 2\frac{\partial}{\partial x_i}\left[(1 - F_1)\frac{\rho\sigma_{\omega 2}}{\omega}\frac{\partial k}{\partial x_i}\psi_6\right] \\
&\qquad + \frac{\partial}{\partial x_i}\left(\psi_6\rho u_i\right) + \frac{\partial^2}{\partial x_i^2}\left[\left(\mu + \sigma_{\omega 1}\mu_t\right)\psi_6\right] = 0,
\end{aligned}
$$

$$\frac{\partial^2}{\partial x_i^2}\left[\left(\mu+\frac{\mu_t}{\sigma_f}\right)\psi_7\right]+\frac{\partial}{\partial x_i}\left(\psi_7\rho u_i\right)+\psi_7 F_{\text{length}} c_{a1}\rho S F_{\text{onset}}{}^{0.5}\left(\frac{0.5}{\sqrt{\gamma}}-1.5c_{e1}\sqrt{\gamma}\right)$$

$$+\,\psi_7 c_{a2}\rho\Omega\gamma F_{\text{turb}}\left(2c_{e2}\gamma-1\right)=0,$$

$$\frac{\partial^2}{\partial x_i^2}\left[\sigma_\theta\left(\mu+\mu_t\right)\psi_8\right]+\frac{\partial}{\partial x_i}\left(\psi_8\rho u_i\right)-\psi_8 c_{\theta t}\frac{(\rho U)^2}{500\mu}(1-F_{\theta t})=0.$$

The integrals of these equations over the domain in the i-direction are

$$\int\left\{\beta^*\rho\omega\psi_5-2\frac{\partial}{\partial x_j}\left[(1-F_1)\frac{\rho\sigma_{\omega 2}}{\omega}\frac{\partial\omega}{\partial x_j}\psi_5\right]+\frac{\partial}{\partial x_i}\left(\psi_5\rho u_i\right)+\frac{\partial^2}{\partial x_i^2}\left[\left(\mu+\sigma_{k1}\mu_t\right)\psi_5\right]\right\}dD=0,$$

$$\int\left\{\left[\beta^*\rho k+2\beta_1\rho\omega-2(1-F_1)\frac{\rho\sigma_{\omega 2}}{\omega^2}\frac{\partial\omega}{\partial x_i}\frac{\partial k}{\partial x_i}\right]\psi_6-2\frac{\partial}{\partial x_i}\left[(1-F_1)\frac{\rho\sigma_{\omega 2}}{\omega}\frac{\partial k}{\partial x_i}\psi_6\right]\right.$$

$$\left.+\frac{\partial}{\partial x_i}\left(\psi_6\rho u_i\right)+\frac{\partial^2}{\partial x_i^2}\left[\left(\mu+\sigma_{\omega 1}\mu_t\right)\psi_6\right]\right\}dD=0,$$

$$\int\left\{\frac{\partial^2}{\partial x_i^2}\left[\left(\mu+\frac{\mu_t}{\sigma_f}\right)\psi_7\right]+\frac{\partial}{\partial x_i}\left(\psi_7\rho u_i\right)+\psi_7 F_{\text{length}} c_{a1}\rho S F_{\text{onset}}{}^{0.5}\left(\frac{0.5}{\sqrt{\gamma}}-1.5c_{e1}\sqrt{\gamma}\right)\right.$$

$$\left.+\psi_7 c_{a2}\rho\Omega\gamma F_{\text{turb}}\left(2c_{e2}\gamma-1\right)\right\}dD=0,$$

$$\int\left\{\frac{\partial^2}{\partial x_i^2}\left[\sigma_\theta\left(\mu+\mu_t\right)\psi_8\right]+\frac{\partial}{\partial x_i}\left(\psi_8\rho u_i\right)-\psi_8 c_{\theta t}\frac{(\rho U)^2}{500\mu}(1-F_{\theta t})\right\}dD=0,$$

which are identical to the continuous adjoint equations for the transition and turbulence models in the i-direction. By performing the same procedure in the j-direction, similar results are achieved. Therefore the complete consistency of the discrete adjoint equations for the $\gamma-\tilde{R}e_{\theta t}$ transition model and $k-\omega$ SST turbulence model is shown over the entire domain.

References

[1] O. Amoignon, J. Pralits, A. Hanifi, M. Berggre, and D. Henningson. Shape optimization for delay of laminar-turbulent transition. *AIAA Journal*, 44:1009–24, 2006.

[2] Scott W. Ashcraft, Andres S. Padron, Kyle A. Pascioni, Jr. Gary W. Stout, and Dennis L. Huff. Review of propulsion technologies for n+3 subsonic vehicle concepts. In *NASA/TM2011-217239*, Glenn Research Center, Cleveland, Ohio, October 2011.

[3] W. A. Basha and W. S. Ghaly. Drag prediction in transitional flow over airfoils. *Journal of Aircraft*, 44:824–32, 2007.

[4] Albert L. Braslow. A history of suction-type laminar flow control with emphasis on flight research. Washinton, DC, 1999. NASA history division.

[5] R. R. Brodeur and C. P. van Dam. Flow transition prediction for wind turbine airfoils. *Wind Energy*, 4:61–75, 2001.

[6] T. Cebeci. *Stability and Transition: Theory and Application*. Horizon Publishing Inc., 2004.

[7] Martin M. D'Angelo, John Gallman, Vicki Johnson, Elena Garcia, Jimmy Tai, and Russell Young. N+3 small commercial efficient and quiet transportation for year 2030-2035. In *NASA/CR2010-216691*, Langley Research Center, Hampton, Virginia, May 2010.

[8] N. A. Denissen, D. A. Yoder, and N. J. Georgiadis. Implementation and validation of a laminar-to-turbulent transition model in the wind-us code. In *NASA/TM2008-215451*, Glenn Research Center, Cleveland, Ohio, September 2008.

[9] M. Drela. Design and optimization method for multi-element airfoils. AIAA Paper 93-0969, 1993.

[10] J. Driver and D. W. Zingg. Numerical aerodynamic optimization incorporating laminar-turbulent transition prediction. *AIAA Journal*, 45:1810–18, 2007.

[11] Toro E.F. *Riemann Solver and Numerical Methods for Fluid Dynamics: A Practical Introduction*. Springer, 2009.

[12] John E. Green. Laminar flow control-back to the future? In *38th Fluid Dynamics Conference and Exhibit*, Seattle, Washington, June 2008. AAIAA 2008-3738.

[13] E. M. Greitzer and H. N. Slater. N+3 aircraft concept designs and trade studies. In *FINAL REPORT;Cooperative Agreement Number NNX08AW63A*, Massachusetts Institute of Technology, 2010.

[14] S. Grundmann. *Transition Control using Dieelectric Barrier Discharge Actuators*. PhD thesis, TU-Darmstadt, 2008.

[15] M. Hepperle. Mdo of forward swept wings, http://www.mh-aerotools.de/company/paper_12/KATnet_-_Forward_Swept_Wings_-_DLR-AS_-Hepperle.pdf.

[16] R. M. Hicks and P. A. Henne. Wing design by numerical optimization. *Journal of Aircraft*, 15:407–412, 1978.

[17] C. Hirsch. *Numerical Computation of Internal and External Flows: Volume 1 and 2*. John Wiley & Sons Inc., 1990.

[18] http://www mdp.eng.cam.ac.uk/web/library/enginfo/aerothermal_dvd_only /aero/fprops/introvisc/node8.html.

[19] http://www.aeronautics.nasa.gov/nra.htm.

[20] http://www.cleansky.eu/content/homepage/activities.

[21] http://www.csi.tu darmstadt.de/institute/dcc/index.en.jsp.

[22] Nocedal J. and Wright S.J. *Numerical Optimization*. Springer Series in Operations Research. Springer, 1999.

[23] A. Jameson. Aerodynamic design via control theory. *Journal of Scientific Computing*, 3:233–60, 1988.

[24] A. Jameson. Automatic design of transonic airfoils to reduce the shock induced pressure drag. In *Proceedings of the 31st Israel Annual Conference on Aviation and Aeronautics*, Tel Aviv, Israel, February 1990.

[25] A. Jameson. Optimum aerodynamic design using cfd and control theory. In *AIAA 12th Computational Fluid Dynamics Conference*, San Diego, CA, June 1995. AIAA paper 95-1729.

[26] A. Jameson, L. Martinelli, and N. Pierce. Optimum aerodynamic design using the navier-stokes equations. *Theoretical Computational Fluid Dynamics*, 10:213–37, 1998.

[27] A. Jameson, W. Schmidt, and E. Turkel. Numerical solution of the euler equations by finite volume methods using runge-kutta time-stepping schemes. In *AIAA 14th Fluid and Plasma Dynamic Conference*, Palo Alto, California, June 1981. AIAA 1981-1259.

[28] C. S. Kim, C. Kim, and O. H. Rho. Sensitivity analysis for the navier-stokes equations with two-equation turbulence models. *AIAA Journal*, 39:838–45, 2001.

[29] S. Kim, J.J. Alonso, and A. Jameson. A gradient accuracy study for the adjoin-based navier-stokes design method. In *AIAA 37th Aerospace Sciences Meeting and Exhibit*, Reno, Nevada, January 1999. AIAA paper 99-0299.

[30] R. B. Langtry. *A Correlation-Based Transition Model Using Local Variables for Unstructured Parallelized CFD Codes*. PhD thesis, University of Stuttgart, Stuttgart, Germany, 2006.

[31] R.B. Langtry and F.R. Menter. Transition modeling for general cfd applications in aeronautics. In *43rd AIAA Aerospace Sciences Meeting and Exhibit*, Reno, Nevada, January 2005. AIAA 2005-522.

[32] R.B. Langtry and F.R. Menter. Correlation-based transition modeling for unstructured parallelized computational fluid dynamics codes. *AIAA Journal*, 47:2894–906, 2009.

[33] J. Lee and A. Jameson. Natural-laminar-flow airfoil and wing design by adjoint method and automatic transition prediction. In *AIAA 47th Aerospace Sciences Meeting including, The New Horizons Forum and Aerospace Exposition*, Orlando, Florida, January 2009. AIAA 2009-897.

[34] J. Lepine, F. Guibault, J. Trepanier, and F. Pepin. Optimized nonuniform rational b-spline geometrical representation for aerodynamic design of wings. *AIAA Journal*, 39:2033–41, 2001.

[35] J. L. Lions. *Optimal Control of Systems Governed by Partial Differential Equations.* Springer-Verlag, 1971.

[36] White F. M. *Viscous fluid flow.* McGraw-Hill series in mechanical engineering. McGraw-Hill, 1991.

[37] P. Malan, K. Suluksna, and E. Juntasaro. Calibrating the $\gamma - \tilde{Re_\theta}$ transition model for commercial cfd. In *AIAA 47th Aerospace Sciences Meeting including, The New Horizons Forum and Aerospace Exposition*, Orlando, Florida, January 2009. AIAA 2009-1142.

[38] L. Martinelli. *Calculations of Viscous Flow with a Multigrid Method.* PhD thesis, Princeton University, Princeton, NJ, October 1987.

[39] F. R. Menter. Two-equation eddy viscosity turbulence models for engineering applications. *AIAA Journal*, 32:1598–605, 1994.

[40] F. R. Menter, R. B. Langtry, S. R. Likki, Y. B. Suzen, P. G. Huang, and S. Volker. A correlation-based transition model using local variablespart i: Model formulation. *Journal of Turbomachinery*, 128:413–22, 2006.

[41] F. R. Menter, R. B. Langtry, S. R. Likki, Y. B. Suzen, P. G. Huang, and S. Volker. A correlation-based transition model using local variablespart ii: Test cases and industrial applications. *Journal of Turbomachinery*, 128:423–34, 2006.

[42] Alan Le Moigne and Ning Qin. Variable-fidelity aerodynamic optimization for turbulent flows using a discrete adjoint formulation. *AIAA Journal*, 42:1281–92, 2004.

[43] S. Nadarajah and A. Jameson. Studies of the continuous and discrete adjoint approaches to viscous automatic aerodynamic shape optimization. In *15th AIAA Computational Fluid Dynamics Conference*, CA, June 2001. AIAA Paper 2001-2530.

[44] S. K. Nadarajah. *The Discrete Adjoint Approach to Aerodynamic Shape Optimization.* PhD thesis, Departement of Aeronautics and Astronautics, Stanford University, Stanford, CA, January 2003.

[45] Jean Perraud, Daniel Arnal, G. Casalis, Jean-Pierre Archambaud, and Raffaele Donelli. Automatic transition predictions using simplified methods. *AIAA Journal*, 47:2676–84, 2009.

[46] O. Pironneau. *Optimal Shape Design for Elliptic Systems.* Springer-Verlag, 1984.

[47] R. Ritlop, P. Khayatzadeh, and S. K. Nadarajah. Design of wind turbine profiles via a preconditioned adjoint-based aerodynamic shape optimization. In *AIAA 47th Aerospace Sciences Meeting including, The New Horizons Forum and Aerospace Exposition*, Orlando, Florida, January 2009. AIAA 2009-1547.

[48] J. Roskam and C.T.E. Lan. *Airplane Aerodynamics and Performance.* Airplane design and analysis. DARcorporation, 1997.

[49] J. G. Schepers, A. J. Brand, A. Bruining, J. M. R. Graham, M. M. Hand, D. G. Infield, H. A. Madsen, R. J. H. Paynter, and D. A. Simms. Final report of IEA annex XIV: field rotor aerodynamics. In *ECN-C-97-027*, 1997.

[50] H. Schlichting. *Boundary Layer Theory.* McGraw-Hill Inc., 6th edition, 1968.

[51] D. M. Somers. Design and experimental results for a natural laminar flow airfoil for general aviation applications. In *NASA TP 1861*, 1981.

[52] D. M. Somers. Design and experimental results for the s809 airfoil. In *NREL SR-440-6918*, 1997.

[53] Dan M. Somers. Subsonic airfoil design; historical background, http://www.airfoils.com/design1.htm.

[54] Niels N. Sorensen. CFD modelling of laminar-turbulent transition for airfoils and rotors using the $\gamma - \tilde{Re}_{\theta t}$ model. *Wind Energy*, 12:715–33, 2009.

[55] P. R. Spalart and C. L. Rumsey. Effective inflow conditions for turbulence models in aerodynamic calculations. *AIAA Journal*, 45:2544–53, 2007.

[56] P.R. Spalart and S.R. Allmara. A one-equation turbulence model for aerodynamic flows. In *30th AIAA Aerospace Sciences Meeting and Exhibit*, Reno, Nevada, January 1992. AIAA 92-0439.

[57] H. W. Stock and W. Hasse. Navier-stokes airfoil computations with transition prediction e^n including transitional flow regions. *AIAA Journal*, 38:2059–66, 2000.

[58] P. Sturdza. *An Aerodynamic Design Method for Supersonic Natural Laminar Flow Aircraft.* PhD thesis, Departement of Aeronautics and Astronautics, Stanford University, Stanford, CA, 2003.

[59] Keerati Suluksna, Pramote Dechaumphai, and Ekachai Juntasaro. Correlations for modeling transitional boundary layers under influences of freestream turbulence and pressure gradient. *International Journal of Heat and Fluid Flow*, 30:66–75, 2009.

[60] A.S. Zymaris, D.I. Papadimitriou, K.C. Giannakoglou, and C. Othmer. Continuous adjoint approach to the spalart-allmaras turbulence model for incompressible flows. *Journal of Computers and Fluids*, 38:1528–38, 2009.